UNIVERSITY OF CALIFORNIA, SAN DIEGO

Colloidal Nanocrystal Metasurfaces

A dissertation submitted in partial satisfaction of the
requirements for the degree of Doctor of Philosophy

in

Materials Science and Engineering

by

Matthew J. Rozin

Committee in charge:

Professor Andrea Tao, Chair
Professor Eric Fullerton
Professor Darren Lipomi
Professor Zhaowei Liu
Professor Donald Sirbuly

2017

The dissertation of Matthew J. Rozin is approved, and it is acceptable in quality and form for publication on microfilm and electronically:

_____

_____

_____

_____

_____

Chair

University of California, San Diego

2017

DEDICATION

Dedicated to my Mother and Father, and to my Brother and two Sisters. Thank you for your patience and for your friendship, and above all your unconditional love.

EPIGRAPH

"I have no special talents. I am only passionately curious."

– Albert Einstein

TABLE OF CONTENTS

LIST OF ABBREVIATIONS

2D	Two-dimensional
3D	Three-dimensional
AFM	Atomic Force Microscope
AgNCs	Silver nanocubes
AgNSs	Silver nanospheres
DI	deionized
EF	Enhancement factor
HDT	1-hexadecanethiol
LB	Langmuir-Blodgett
LSPR	Localized surface plasmon resonance
NP	Nanoparticle
PhSH	Thiophenol
PVP	Polyvinylpyrrolidone
RA	Raman analyte
SAM	Self-assembled monolayer
SEM	Scanning electron microscope
SERS	Surface-enhanced Raman spectroscopy
SHG	Second Harmonic Generation
SNR	Signal-to-noise ratio

LIST OF FIGURES

LIST OF TABLES

ACKNOWLEDGEMENTS

I would like to acknowledge Professor Andrea R. Tao for her support as my advisor and mentor, and as the chair of my committee. I would also like to acknowledge the Tao Lab—both past and present members—for their continual academic, professional, and emotional support over the past five-odd years.

Chapter 2, in part, is a reformatted reprint of material from the following published paper: Gao, B., **Rozin, M. J.** and Tao, A. R. Plasmonic Nanocomposites: Polymer-Guided Strategies for Assembling Metal Nanoparticles. *Nanoscale* 5, 5677-5691, (2013). The dissertation author was the second author, or principal co-author for the above paper.

Chapter 3 is a reformatted reprint in full, of the material from: **Rozin, M. J.**, Rosen, D., Dill, T. J. and Tao, A. R. Colloidal Metasurfaces Displaying Near-Ideal and Tunable Light Absorbance in the Infrared. *Nature Communications* 6, (2015). The dissertation author was the principal researcher and author of this paper.

Chapter 4, in full, is currently being prepared for submission for publication of the material. **Rozin, M. J.**; Zeng, Y.; Brown, E. R; Qian, H.; Liu, Z.; and Tao, A. R., Enhanced Second Harmonic Generation in Colloidal Metasurfaces. The dissertation author was the principal researcher and author of this material.

Chapter 5, in part, is a reformatted reprint of the material from: Dill[†], T. J. & **Rozin[†], M. J.**, Brown, E. R., Palani, S., Tao. A. R., Investigating the Effects of Polydispersity on Gap-Mode SERS Enhancement Factors. *The Analyst* **2016**, 141 (12),

3916-3924. (†Authors contributed equally) The dissertation author was the principal researcher and author of this paper.

VITA

2011 Bachelor of Science, University of Massachusetts, Amherst

2012 Master of Science, University of California, San Diego

2017 Doctor of Philosophy, University of California, San Diego

PUBLICATIONS

Dill, T. J.; Rozin, M. J.; Brown, E. R.; Palani, S.; Tao, A. R., Investigating the Effect of Ag Nanocube Polydispersity on Gap-Mode SERS Enhancement Factors. *Analyst* **2016,** *141* (12), 3916-3924.

Dill, T. J.; Rozin, M. J.; Palani, S.; Tao, A. R., Colloidal Nanoantennas for Hyperspectral Chemical Mapping. *ACS Nano* **2016,** *10* (8), 7523-7531.

Rozin, M. J.; Rosen, D. A.; Dill, T. J.; Tao, A. R., Colloidal Metasurfaces Displaying Near-Ideal and Tunable Light Absorbance in the Infrared. *Nature Communications* **2015,** *6*.

Laxminarayana, G. K., Rozin, M. J., Smith, S. and Tao, A. R. Modular, Polymer-Directed Nanoparticle Assembly for Fabricating Metamaterials. *Faraday Discussions*, **2015**

Gao, B., Rozin, M. J. and Tao, A. R. Plasmonic Nanocomposites: Polymer-Guided Strategies for Assembling Metal Nanoparticles. *Nanoscale* **2013**, 5, 5677-5691

FIELDS OF STUDY

Major Field: Materials Science, NanoEngineering

Studies in colloidal synthesis, plasmonics, self-assembly, optical metasurfaces

Professor Andrea Tao

ABSTRACT OF THE DISSERTATION

Colloidal Nanocrystal Metasurfaces

by

Matthew J. Rozin

Doctor of Philosophy in Materials Science and Engineering

University of California, San Diego, 2017

Professor Andrea Tao, Chair

Metasurfaces are ultrathin, quasi-two-dimensional materials that are engineered to control and manipulate the flow of light, producing properties unattainable with naturally occurring materials. Metasurfaces designed to operate

within the visible spectrum are of particular interest for advanced nanoscale light sources and chemical sensing. One promising approach to building optical metasurfaces utilizes plasmonic nanoantenna to funnel freely-propagating visible and near-infrared radiation from the far-field into confined nanoscale volumes using metallic antenna. Localized surface plasmon resonances (LSPR) supported by metallic nanoantenna strongly enhance the incident optical field, providing enhanced far-field coupling as well as enhancement of nonlinear optical processes. However, features significantly smaller than the wavelength of light are required and control over nanoscale morphology can be to achieve. In this thesis, I use bottom-up assembly methods to fabricate colloidal nanocrystal metasurfaces and experimentally demonstrate their capability as a tunable, ultrathin platform for controlling highly enhanced optical fields at the nanoscale. Shaped plasmonic nanocrystals are arranged using bottom-up self-assembly methods to produce metasurfaces operational throughout the visible and near-infrared spectrum. These metasurfaces exhibit extreme in-plane electromagnetic coupling that is strongly dependent on nanocrystal size, shape and spacing, displaying near-ideal electromagnetic absorbance tunable between 500–3,000 nanometers. I investigate their ability to mediate and enhance nonlinear optical processes such as second harmonic generation (SHG) and Raman scattering. By utilizing the double-resonance of metal thin-film coupled nanoantenna, we demonstrate colloidal metasurfaces as efficient sources for nonlinear light generation, achieving SHG enhancement of 10^4, with efficiencies of $5x10^{-10}$. Finally, I investigate

colloidal metasurfaces for ultra-sensitive detection and hyperspectral chemical mapping, with uniform and predictable Raman enhancement factors of 10^6–10^7.

Chapter 1

Introduction

1.1. Overview

In this dissertation, I describe my doctoral research on a bottom-up approach for building optical metasurfaces with colloidal nanocrystals as the building blocks. Metasurfaces are composite materials that utilize artificial subwavelength structure to steer the flow of light in unusual ways, achieving novel optical phenomena not found in nature. Optical metasurfaces provide a novel means to realize numerous optoelectronic applications, such as subwavelength imaging,[1] ultrafast optical switching and generation,[2-6] photodetection,[7-9] chemical sensing,[10, 11] and plasmonic enhanced light harvesting and photovoltaics.[12, 13] Metasurfaces are unique among optical materials; they exhibit spatially varying electromagnetic response, giving rise to optical properties which are highly dependent on metasurface structure. In order to effectively manipulate electromagnetic radiation at visible frequencies, the size and spacing of structural constituents which make up the metasurface must be significantly smaller than the wavelength of light—well within the nanoscale size regime. As a result, the ability to predictably and precisely control the long-range order of metallic nanostructures—down to a few billionths of a meter—will enable a new class of ultrathin, designer optical materials with unprecedented performance and flexibility.

While the research surrounding electromagnetic metasurfaces can be traced back to the early part of last century,[14] the present-day field of optical metasurfaces has come to be only over the past two decades. It was made possible in part by the

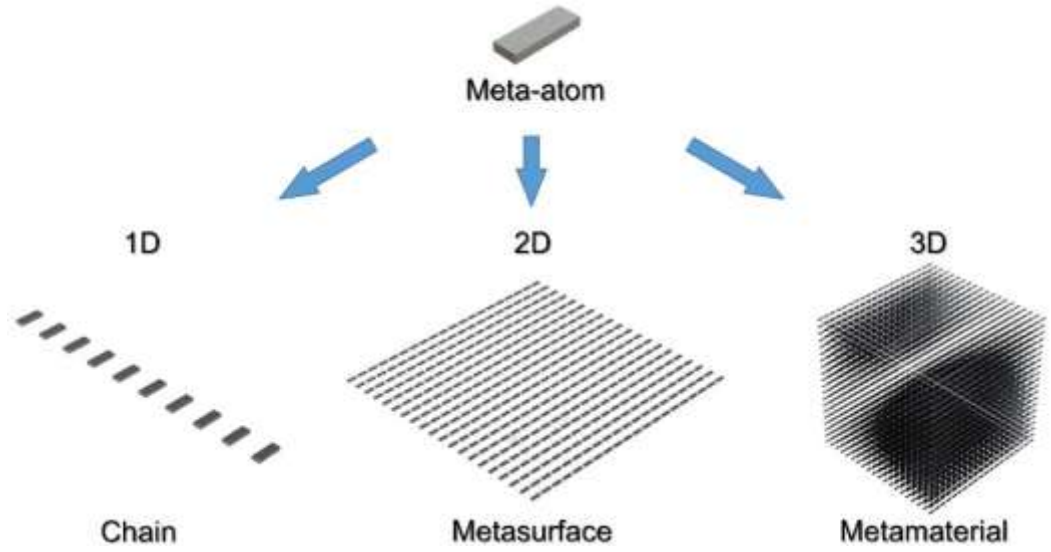

Figure 1.1. Metamaterial dimensionality. Metamaterials are a class of modern, composite materials, deliberately designed to manipulate the flow of fields, i.e. light, heat, or sound. In the case of electromagnetic metamaterials, they are composed of sub-wavelength resonators, or meta-atoms. (Figure credit: J. Wang et al. 2016) [9]

groundbreaking work on the theory of transformation optics from John Pendry,[15, 16] and the experimental demonstration of metasurfaces in the microwave regime by David R. Smith.[17, 18] To date, the challenge of controllably fabricating nanoscale features in metals and dielectrics required for optical-regime metasurfaces has predominantly relied on direct-write or lithography-based nanofabrication techniques such as focused ion-beam milling and electron-beam lithography. These so-called *top-down* fabrication techniques, while suitable for building proof-of-concept structures, are beset by severe limitations in scalability, complexity, throughput, and above-all, cost. This herein constitutes the engineering-centric motivation for the work in this thesis—interest in the practical challenges and applications of building novel functional optical materials using straight-forward, scalable, and inexpensive bottom-up methods. In contrast to traditionally employed top-down nanofabrication, a bottom-

up approach relies on chemical synthesis of nanocrystals. By engineering the surface chemistry and interfacial physics of such colloidal nanocrystal solutions, useful structures can be coaxed into predictably and controllably self-assembling. From a fundamental perspective, the work in this thesis is motivated by the rich and often surprising plethora of optical phenomena surrounding the interaction of light with metallic nanocrystals.

1.1.1. Optical Metasurfaces

An *optical metasurface* can be defined as an ultrathin, quasi-two-dimensional composite engineered to control and manipulate the flow of light in order to produce properties that are unattainable with naturally occurring materials. The term metasurface is an adaptation of the three dimensional, or bulk *metamaterial*—an artificially structured composite material without confined dimensionality. Metasurfaces are composed of an array of subwavelength resonators, commonly referred to as *meta-atoms*, often supported by some underlying substrate or backplane. Meta-atoms act like nanoscale antenna in the optical regime, channeling free propagating visible and near-infrared radiation into localized energy, confined to volumes hundreds of times smaller than the wavelength of light. Similar to radiowave antennas at sub-MHz frequencies or microwave antennas operating at a few GHz; optical nanoantenna function at hundreds of terahertz (THz).

Conventionally, meta-atoms consist of a metallic resonator electromagnetically isolated within a dielectric medium—typically Au or Ag nanostructures for meta-

atoms which operate at optical frequencies. The meta-atom serves as a unit-cell for the ensemble metasurface structure, where the lateral organization of the unit-structure can be periodic, quasi-periodic, or random, however must remain subwavelength. The scale of the meta-atom—concerning both size and spacing—is required to be considerably smaller than the wavelength of light in order for the composite metasurface to behave effectively as a continuous material. In effect, the collection of discrete meta-atom element responses is replaced by a collective, macro-scale optical response for the metasurface.

1.2. Background & Theory

1.2.1. Electromagnetic Response of Metals

In order to discuss how optical metasurfaces function, we must first briefly describe the frequency dependent optical properties of metals. At low frequencies—spanning from low energy radio waves through the infrared—the electromagnetic response of metals can be closely approximated as that of a perfect conductor.[19] Under a plasma model, the high density of free carriers in metals—commonly referred to as the sea of conduction electrons or the free electron gas—is able to freely move about the fixed background of ion cores of the metallic crystal lattice. An impinging electromagnetic wave on a bulk metal induces collective oscillations of the metal's free electron gas. The quanta of these free oscillations of the electron gas are called volume plasmons. Metals are highly reflective in this low-frequency regime, permitting only a negligible quantity of incident light to penetrate into their bulk.

However, the perfect conductor approximation no longer holds at higher frequencies, where noble metals such as Au, Ag, and Pt exhibit increased field penetration and dissipation resulting from transitions between electronic bands.[20]

1.2.2. Localized Surface Plasmon Resonance

The electromagnetic response of metals is closely linked with the physical phenomenon of localized surface plasmon resonance, or LSPR. Like their bulk or volume counterparts, surface plasmons are collective oscillations of a metal's conduction-band electrons in relation to the static ionic lattice of the metal. However LSPRs are localized to nanoscale features of a metallic surface, whether sharp features on the surface of a roughened metal film, or the edges and corners of a metallic nanoparticle. Such sharp features of a metal surface effectively focus the collective oscillations of the free electron gas, in what's known as the lightning rod effect. This focusing produce so-called hot spots, where the local electromagnetic field can be amplified to many times it's incident intensity. These strong local field intensities, or near-fields, have a profound effect on their immediate environment. LSPRs decay evanescently from the metal surface, and can dramatically increase the interaction with far-field radiation.

1.2.3. Surface Plasmon Coupling

The evanescent field generated by a surface plasmon decays over short distances (proportional to $1/d^3$) away from the surface of a metal nanoparticle (NP).

To produce a nanojunction that effectively confines light to a small volume, strong electromagnetic coupling must be generated between closely-spaced NPs with interparticle gaps of only a few nanometers. Interparticle separation distance is observed to have a profound effect on the resonant wavelength for which strong coupling is observed. While direct-write techniques such as electron-beam lithography can produce nanostructures with sub-10 nm separation distances, achieving such spatial control with bottom-up assembly methods can present a difficult challenge.

A growing area of research in plasmonics is the assembly of shaped NP building blocks. Shaped metal NPs possess LSPRs that can be tuned through chemical synthesis[21] and possess compelling geometries for constructing plasmonic nanojunctions by NP coordination through facet, corner, or edge sites.[22, 23] Within these NP assemblies, electromagnetic coupling between neighboring NPs is highly sensitive to NP orientation. For two approaching NPs, van der Waals forces scale exponentially with the surface area of interaction.[24] As a result, shaped NPs tend to organize into close-packed structures that maximize this interaction area: rods align side-by-side,[25] cubes align face-to-face.[26, 27] To control plasmonic coupling, NP assembly strategies must overcome these attractive van der Waals forces. As a result, significant efforts have been directed toward developing strategies for rationally assembling shaped NP building blocks into specific geometric orientations.

1.3. Colloidal Nanocrystal Meta-Atoms

Colloidal metal nanocrystals of nearly every shape and size imaginable have been synthesized for use as meta-atoms. These nanoparticles, typically Au or Ag and ranging in size from 10-500 nm exhibit strongly confined electromagnetic fields, or 'hotspots' upon excitation with incident radiation. Hotspots formed by either roughened metal surfaces or metal nanoparticles originate from localized surface plasmon resonances (LSPRs) focused at the apexes of such nanostructures. But not all nanoparticles are equally good at generating intense and reproducible hot spots. Colloidal Ag nanocrystals are advantageous for designing optical metasurfaces because of the high quality resonances they support, owing to their single crystalline and highly faceted nature. Of particular interest are Ag nanocubes, synthesized via a modified polyol method.[28] In this one-pot, reagent-limited synthesis, polyvinylpyrrolidone (PVP) serves as a selective capping agent, controlling the nucleation and growth of single crystalline Ag nanocubes. The PVP physisorbs to the bare Ag surface, effectively encapsulating the nanocubes, protecting them against oxidation and ripening, and providing a convenient dielectric spacer layer of a few nanometers.[29]

The ability to design nanoparticle metasurfaces using entirely bottom-up assembly techniques allows for parallel and scalable fabrication. SERS substrates are commonly designed to utilize the increase in local field enhancement associated with coupling between LSPRs of adjacent nanostructures, which in general produces a stronger field than either single nanoparticle constituent. In the nanocube metasurface,

strong plasmonic coupling between the nanocube and its dipole image in the metal film focuses light within the cavity formed between two parallel surfaces. Multiple reflections within the parallel cavity produce highly enhanced electromagnetic fields, even greater than the hotspots formed by the sharp nanocube edges or corners. In addition to higher field enhancement, the field confinement within the nanocube-film gap represents a significantly larger Raman-active volume than that for a junction formed between two nanocube corners or edges. Unlike such systems as bowtie junctions tuned for maximum absolute field enhancement, or stacked disk-like pairs, with large volume hotspots for maximum average field enhancement, the nanocube metasurface geometry is optimized for both maximum absolute field enhancement and Raman-active volume. This makes the nanocavities formed within the nanocube metasurface an ideal system for ultra-sensitive detection of trace analytes.

1.4. Advances & Outlook

1.4.1 Applications of Optical Metasurfaces

We find numerous fundamental and applied motivations for advancing the nascent field of optical metasurfaces, based on the rich degree of classical, nonlinear, and quantum optoelectronic phenomena surrounding the interaction of light with metallic nanocrystals. Optical metasurfaces promise practical applications of building novel and functional materials using inexpensive, and scalable bottom-up methods. Such an approach utilizes creative chemistry and the unique physics that occurs at

interfaces, to rationally impose the conditions for systems at the nanoscale to controllably self-assemble.

1.5. References

1. Leonhardt, U., Optical Conformal Mapping. *Science* **2006,** *312* (5781), 1777.

2. Boyd, R. W., Chapter 13 - Ultrafast and Intense-Field Nonlinear Optics. In *Nonlinear Optics (Third Edition)*, Academic Press: Burlington, 2008; pp 561-587.

3. Dolling, G.; Enkrich, C.; Wegener, M.; Zhou, J. F.; Soukoulis, C. M.; Linden, S., Cut-wire pairs and plate pairs as magnetic atoms for optical metamaterials. *Optics Letters* **2005,** *30* (23), 3198-3200.

4. Linnenbank, H.; Grynko, Y.; Forstner, J.; Linden, S., Second harmonic generation spectroscopy on hybrid plasmonic/dielectric nanoantennas. *Light Sci Appl* **2016,** *5*, e16013.

5. Klein, M. W.; Enkrich, C.; Wegener, M.; Linden, S., Second-Harmonic Generation from Magnetic Metamaterials. *Science* **2006,** *313* (5786), 502.

6. Kauranen, M.; Zayats, A. V., Nonlinear plasmonics. *Nat Photon* **2012,** *6* (11), 737-748.

7. Knight, M. W.; Sobhani, H.; Nordlander, P.; Halas, N. J., Photodetection with Active Optical Antennas. *Science* **2011,** *332* (6030), 702-704.

8. Fang, Z.; Liu, Z.; Wang, Y.; Ajayan, P. M.; Nordlander, P.; Halas, N. J., Graphene-Antenna Sandwich Photodetector. *Nano Letters* **2012,** *12* (7), 3808-3813.

9. Mukherjee, S.; Libisch, F.; Large, N.; Neumann, O.; Brown, L. V.; Cheng, J.; Lassiter, J. B.; Carter, E. A.; Nordlander, P.; Halas, N. J., Hot Electrons Do the

Impossible: Plasmon-Induced Dissociation of H2 on Au. *Nano Letters* **2012,** *13* (1), 240-247.

10. Cao, Y. C.; Jin, R.; Mirkin, C. A., Nanoparticles with Raman Spectroscopic Fingerprints for DNA and RNA Detection. *Science* **2002,** *297* (5586), 1536.

11. Anker, J. N.; Hall, W. P.; Lyandres, O.; Shah, N. C.; Zhao, J.; Van Duyne, R. P., Biosensing with plasmonic nanosensors. *Nat Mater* **2008,** *7* (6), 442-453.

12. Ferry, V. E.; Sweatlock, L. A.; Pacifici, D.; Atwater, H. A., Plasmonic Nanostructure Design for Efficient Light Coupling into Solar Cells. *Nano Letters* **2008,** *8* (12), 4391-4397.

13. Atwater, H. A.; Polman, A., Plasmonics for improved photovoltaic devices. *Nat Mater* **2010,** *9* (3), 205-213.

14. Wood, R. W., On a Remarkable Case of Uneven Distribution of Light in a Diffraction Grating Spectrum. *Proceedings of the Physical Society of London* **1902,** *18* (1), 269.

15. Pendry, J. B.; Schurig, D.; Smith, D. R., Controlling Electromagnetic Fields. *Science* **2006,** *312* (5781), 1780.

16. Schurig, D.; Mock, J. J.; Justice, B. J.; Cummer, S. A.; Pendry, J. B.; Starr, A. F.; Smith, D. R., Metamaterial Electromagnetic Cloak at Microwave Frequencies. *Science* **2006,** *314* (5801), 977.

17. Smith, D. R.; Schultz, S.; Markoš, P.; Soukoulis, C. M., Determination of effective permittivity and permeability of metamaterials from reflection and transmission coefficients. *Physical Review B* **2002,** *65* (19), 195104.

18. Smith, D. R.; Padilla, W. J.; Vier, D. C.; Nemat-Nasser, S. C.; Schultz, S., Composite Medium with Simultaneously Negative Permeability and Permittivity. *Physical Review Letters* **2000,** *84* (18), 4184-4187.

19. Maier, S. A., *Plasmonics: Fundamentals and Applications*. Springer: 2007.

20. Rakić, A. D.; Djurišić, A. B.; Elazar, J. M.; Majewski, M. L., Optical properties of metallic films for vertical-cavity optoelectronic devices. *Applied Optics* **1998,** *37* (22), 5271-5283.

21. Mock, J. J.; Barbic, M.; Smith, D. R.; Schultz, D. A.; Schultz, S., Shape effects in plasmon resonance of individual colloidal silver nanoparticles. *J Chem. Phys.* **2002,** *116* (15), 6755-6759.

22. Schuck, P. J.; Fromm, D. P.; Sundaramurthy, A.; Kino, G. S.; Moerner, W. E., Improving the Mismatch between Light and Nanoscale Objects with Gold Bowtie Nanoantennas. *Phys. Rev. Lett.* **2005,** *94* (1), 017402.

23. Su, K. H.; Wei, Q. H.; Zhang, X.; Mock, J. J.; Smith, D. R.; Schultz, S., Interparticle Coupling Effects on Plasmon Resonances of Nanogold Particles. *Nano Lett.* **2003,** *3* (8), 1087-1090.

24. Israelachvili, J. N., *Intermolecular and surface forces*. Academic Press: 1992.

25. Nikoobakht, B.; Wang, Z. L.; El-Sayed, M. A., Self-Assembly of Gold Nanorods. *J Phys. Chem.B* **2000,** *104* (36), 8635-8640.

26. Chen, M.; Kim, J.; Liu, J. P.; Fan, H.; Sun, S., Synthesis of FePt Nanocubes and Their Oriented Self-Assembly. *J. Am. Chem. Soc* **2006,** *128* (22), 7132-7133.

27. Ren, J.; Tilley, R. D., Preparation, Self-Assembly, and Mechanistic Study of Highly Monodispersed Nanocubes. *J. Am. Chem. Soc* **2007,** *129* (11), 3287-3291.

28. Gao, B.; Arya, G.; Tao, A. R., Self-orienting nanocubes for the assembly of plasmonic nanojunctions. *Nat Nano* **2012,** *7* (7), 433-437.

29. Rozin, M. J.; Rosen, D. A.; Dill, T. J.; Tao, A. R., Colloidal metasurfaces displaying near-ideal and tunable light absorbance in the infrared. *Nat Commun* **2015,** *6*.

Chapter 2

Nanocrystal Synthesis & Assembly

2.1. Introduction

Metal nanoparticles composed of Au and Ag behave like optical antennae by supporting the excitation of localized surface plasmon resonances (LSPRs), where conduction electrons of the metal oscillate in resonance with the incident light wave to produce intense electromagnetic fields localized at the metal surface. The size, shape, and arrangement of plasmonic metal NPs are critical in determining the LSPR wavelength and the magnitude of the resulting field enhancement. *Hot spots* —where the electromagnetic field is highly confined within a small volume — are particularly pronounced at sharp nanoscale features (i.e. the antenna effect) and small gaps between adjacent metal surfaces. To utilize this plasmonic field enhancement within a device, hot spots must be fabricated with controlled densities and locations. Thus, arrays of NPs are typically desired. For example, periodic arrays of metal NPs deposited at an absorber interface can serve as plasmonic concentrators in a photovoltaic device[1] and two-dimensional (2D) arrays of nanoscale split-ring resonators[2] and paired metal stripes[3] have been demonstrated as negative-index metamaterials.

Self-assembly provides a bottom-up approach to the fabrication of plasmonic arrays and has the potential to accommodate massively parallel, large-scale materials processing for device integration. Specifically, NP organization can be engineered for specific optical functions, for example: chains for waveguiding;[4] tapers and gaps for focusing;[5] grooves and apertures for transmission;[6] and clusters for negative refractive index metamaterials.[7] In addition, ensembles of NPs can support SP excitation over

multiple length scales — from a few nanometers for LSPRs to tens of microns for long-range propagating surface plasmons — and may enable the observation of unique emergent optical properties. A significant challenge in the self-assembly of metal NPs is the formation of non-close-packed NP groupings that possess hierarchical order and specific interparticle orientations. Towards this end, a variety of self-assembly strategies for colloidal metal NPs have been explored for the fabrication of plasmonic materials, including capillary or convective assembly, assembly at fluid interfaces, and chemical tethering between NPs.[7a, 8]

Polymer-directed assembly is a particularly attractive route for the organization of colloidal metal NPs into plasmonic groups and arrays. In these strategies, Ag and Au NPs whose surfaces are grafted with polymer chains can be organized into clusters, chains, micelles, and other complex structures. Assembly is guided by intermolecular forces rather than strong chemical bonds between NPs. Generally, these NP assemblies form by approaching equilibrium, where variables such as polymer graft length, graft density, and miscibility are important parameters in determining the energy of interaction between NPs. In this manner, polymer grafts can be selected to control the spacing between NPs, the orientation of shaped NPs, or the long-range order of NPs dispersed within a polymer matrix. The formation of nanocomposite materials is particularly attractive not only because the polymer matrix provides a convenient dielectric medium for encapsulation of the plasmonic NPs, but also because it enables the use of polymeric processing techniques (e.g. extrusion, molding, thin-film casting) that are amenable for large-scale manufacturing of these

electromagnetic materials.

2.2. Colloidal Nanoparticle Assembly

2.2.1. Surface Functionalization

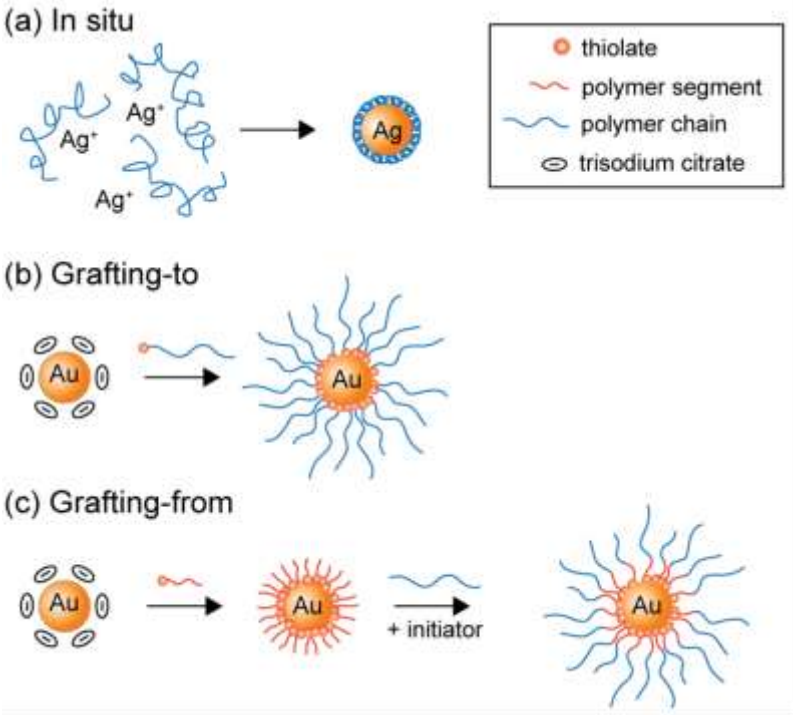

Figure 2.1. Schematic illustration of polymer grafting strategy on NP surfaces. (a) In situ grafting, (b) Grafting-to, and (c) Grafting-from.

Plasmonic NPs are typically surface-modified with polymer grafts during NP synthesis or in a post-synthetic ligand exchange step. For modification *in situ*, surface functionalization is carried out during the NP synthesis by introducing the desired polymer graft into the reaction mixture. (Fig.1a) The polymer can serve a double role as both a shape-directing molecule and a surface passivating agent during the

synthesis. For example, the polyol process is a common approach to synthesize colloidal Ag and Au NPs by carrying out metal reduction in a diol solvent. Poly (vinyl pyrrolidone) (PVP) is generally added continuously during the reduction of a metal salt. PVP is known to behave as a stabilizing agent for the lowest energy crystal faces of Ag and Au (e.g. the {111}, {100}, and {110} planes), and promotes the formation of polyhedral NPs.[15, 16] The resulting polyhedral NPs are well-protected by PVP chains, which are grafted to the metal surface through interaction with their pyrrolidone functional groups. While polymer grafting density is poorly controlled in this reaction, it is likely that the polymer chains adopt a brush-like structure at the metal surface given the typical lengths of the PVP chains (M_w = 29k-200k) employed in these synthesis.[15-17]

Similarly, Ag and Au NPs can be synthesized in the presence of cationic polyelectrolytes to produce crystalline NPs with a narrow size-distribution.[18] Polyelectrolyte-stabilized NPs are prepared via the rapid addition of a fast reducing agent such as potassium borohydride to an aqueous solution of a metal salt (such as $AgNO_3$ or $HAuCl_4$) and excess polyelectrolyte.[18] *In situ* modification is dependent on the polyelectrolyte's ability to form complexes with the metal cation, and various chloride-based cationic polyelectrolytes such as poly(diallyldimethylammonium chloride) and poly(2-hydroxy-3-methacryloxypropyltrimethyl ammonium chloride) are commonly used.[19] Polymer graft layers resulting from *in situ* NP modification with a polyelectrolyte tend to be limited to sub-monolayer shells surrounding the NPs, since the polymers are inherently labile and must allow for NP nucleation and growth.

Thicker polymer layers can be achieved by grafting metal NPs with cross-linked amphiphilic copolymers, where shell thickness is controlled by tuning the NP to copolymer ratio in solution.[20] NPs can be modified post-synthesis through ligand exchange reactions that substitute the capping molecule of the as-made NP, or through chemical alteration of the capping molecule. For NPs that serve as plasmonic building blocks, commonly used capping molecules include sodium citrate and various cationic surfactants such as cetyl trimethylammonium bromide[21], benzyldimethyl hexadecylammonium chloride[22, 23], or cetylpyridinium chloride monohydrate.[24, 25] Because these capping molecules tend to be labile and only weakly chemisorbed to the NP surface, ligand exchange reactions are a versatile strategy for NP surface modification with polymer grafts. (Fig. 1b) Displacement of the capping molecule is typically carried out by either: (i) covalent binding of the graft to the NP surface, or (ii) through chemisorption of the polymer graft. The effectiveness of this displacement depends on the affinity of the polymer graft with the NP surface. Post-synthetic modification of the NP is typically limited to polymer grafts that display strong binding affinities to metal surfaces. For example, thiol-functionalized polymer grafts are widely used in the surface modification of plasmonic NPs, since the high affinity of the thiol for Ag and Au enables facile end-tethering of the polymer to the metal NP surface.[26, 27]

In order to modify the composition of the chemical grafts on the NP surface *in situ*, a grafting-from approach can be considered where polymers are grown from the NP surface via polymerization reactions.(Fig.1c) This technique is useful for building

brush like or cross-linked ligand shells, with thickness on the order of or larger than the NP diameter. Responsive polymers can be utilized in a grafting-from approach to create smart core/shell particles or microgels that respond to external stimuli by shrinking or swelling. For example, growth of the poly-N-isopropylacrylamide (pNIPAM) shell around the Au NPs has been demonstrated through precipitation polymerization on the Au NP surface using the monomer NIPAM and cross-linker.[28] Other polymers such as polystyrene (PS),[29, 30] poly(vinyl alcohol) (PVA),[31] polystyrene-b-poly(acrylic acid) (PS-b-PAA),[32, 33] polypyrrole,[34] and phenol formaldehyde resin[35] have also been successfully attached using a grafting-from approach.

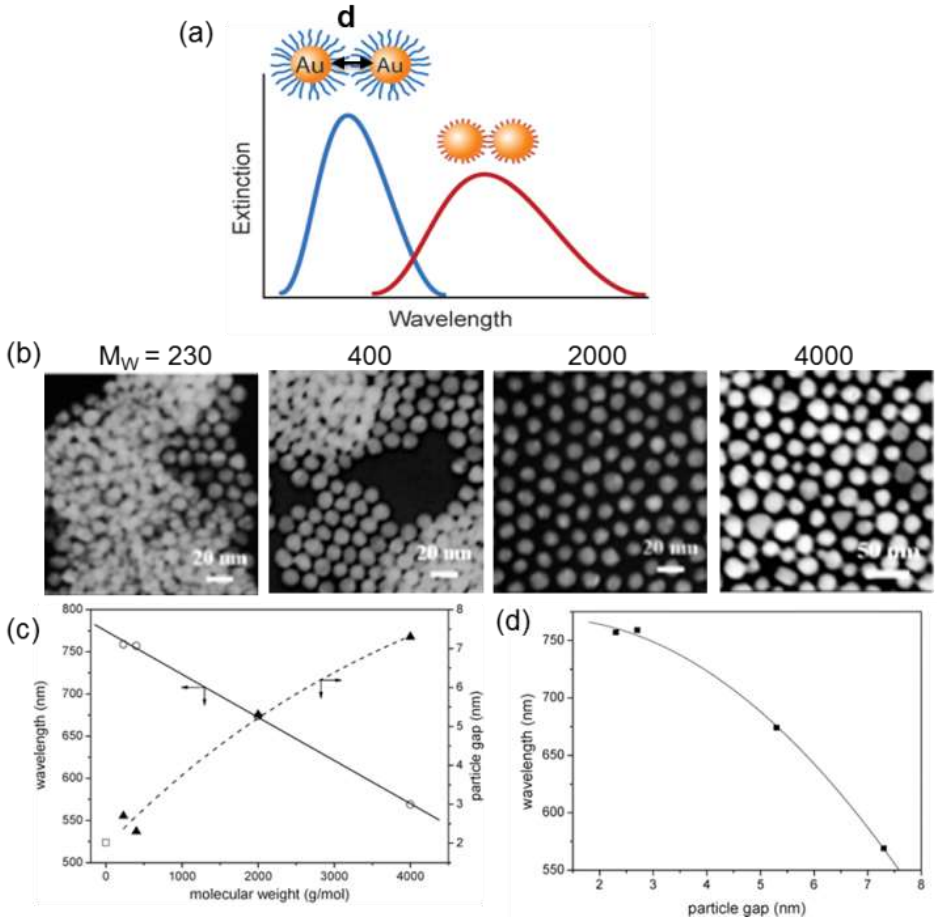

Figure 2.2. NP coupling vs. graft length. (a) Schematic illustration of dependence of Au NP plasmonic coupling on grafted polymer chain length. (b) TEM images of Au NPs modified with POPDA of different molecular weights. (c) Absorption band (circle) and particle gap (triangle) of Au NP change as a function of ligand molecular weight. (d) Gap dependence of the optical absorption of ligand-capped Au NPs. (Reproduced with permission from Ref.25).

2.2.2. Plasmonic Gaps

The evanescent field generated by a surface plasmon decays over short distances (proportional to $1/d^3$) away from the surface of a metal NP. To produce a nanojunction that effectively confines light to a small volume, strong electromagnetic coupling must be generated between closely-spaced NPs with interparticle gaps of only a few nanometers. Interparticle separation distance is observed to have a

profound effect on the resonant wavelength for which strong coupling is observed. While direct-write techniques such as electron-beam lithography can produce nanostructures with sub-10 nm separation distances,[36, 37] achieving such spatial control with bottom-up assembly methods can present a difficult challenge.

Polymer grafts can be used as molecular spacers to control metal NP separation distances during the assembly process. By thoughtfully tailoring the length of the graft chain, inter-NP junctions can be tuned to control the degree of plasmonic coupling between NPs (Fig. 2a). Moreover, compression of the grafts at short interparticle separation distances provides an entropic barrier to gap distances of zero (i.e. touching or fused NPs). For example, spherical Au NPs can be self-organized into 2D and 3D aggregates after surface modification with poly(oxypropylene)diamines, which act as cross-linkers that drive NP assembly. As molecular weight of the polymer is increased from 230 to 4000 g/mol, the inter-NP distances in the NP aggregates are increased from 2.7±0.7 nm to 7.3±1.3 nm.[38] Correspondingly, the optical response of these aggregates shows a large blue-shift in LSRP wavelength from 759 nm to 569 nm. (Fig. 2b-d)

In linear NP assemblies, this polymer-directed control over interparticle spacing has been demonstrated with nanometer precision. For example, spherical Au NPs suspended in a mixture of ethanol and water can be aggregated to form chainlike assemblies by adding short thiol-terminated grafts with the formula $HS(CH_2)_nCOOH$, where *n* is number of methylene units in the graft. The interparticle spacings between adjacent Au NPs are dependent on *n*, which was varied from 2-15 units to tune the

interparticle spacing between 0.6-1.6 nm.[39] Smaller spacings give rise to a red-shift in the observed LSPR wavelength due to increased plasmon coupling, with a maximum shift of λ = 97 nm. Interparticle spacing can be further guided by utilizing a more rigid polymer backbone to facilitate NP assembly into chains (Fig. 3), which can increase the interparticle spacing up to 5.4 nm.[40]

Polymer grafts can also be utilized to fabricate dynamic, responsive plasmonic assemblies by employing grafts that exhibit adaptable chain lengths or conformations. For example, Au nanorods that are chemically modified by end-tethered photoactive polymers can be assembled into linear superstructures whose inter-rod spacings are controlled by solvent swelling.[41] The polymer grafts between neighboring nanorods are first photochemically cross-linked, resulting in a reduction of the inter-rod spacing of up to 55% and corresponding red-shift of λ = 60 nm in the LSPR wavelength. This red-shift occurs specifically for the longitudinal LSPR mode that is polarized along the nanorod main axis, since the nanorods are aligned end-to-end. Solvent-induced swelling of the cross-linked grafts can then be carried out to increase in the inter-rod distance, while maintaining the structural integrity of the chain-like nanorod assembly. (Fig. 4b) Swelling of the cross-linked polymers weakens electromagnetic coupling between adjacent nanorods and leads to an observable blue-shift of the LSPR wavelength.

Using inter-NP spacing to induce dramatic changes in LSPR wavelength was further demonstrated by Qian et al. in the development of pH-responsive substrates for surface-enhanced Raman spectroscopy (SERS). (Fig. 4f) Au NPs were grafted with a

thiol-functionalized block copolymer (BCP) consisting of a pH-responsive polymethacrylic acid (PMAA) block (M_W=3000) and an amphiphilic polyethylene glycol (PEG) block (M_W=5000).[42] At pH < 4, the PMAA segment undergoes a reversible conformational change from an expanded chain to a collapsed structure, leading to a large decrease in interparticle distance and an increase in electromagnetic coupling between NPs. As a result of this hot spot generation, they observed large pH-dependent intensity changes for SERS reporter molecules located in the interparticle gaps.

For 3D plasmonic assemblies, controlled interparticle separation distances have been accomplished using the "brick-and-mortar" approach developed by the Rotello group, where a polymer dendrimer serves as the "mortar" or spacer layer between neighboring Au NPs.[43] Here, the polymer spacer can be chemisorbed to the NP surface through electrostatic interactions. For example, an amine-terminated poly(amidoamine) dendrimer can be chemisorbed to the surface of Au NPs covalently grafted with carboxylic acid terminated ligands (Fig. 5). The electrostatic interaction between the terminal amine on the dendrimer and the carboxylic acid on the NP surface provide the driving force for self-assembly. Increasing dendrimer diameter increases the interparticle separation distance between NPs within the assembly. This is accompanied by a blue-shift in the optical extinction peak of the NP-dendrimer clusters due to weakened inter-NP electromagnetic coupling. The coupled LSPR mode is tunable over a range of λ= 80 nm for dendrimers between 0.6-1.9 nm in diameter.

Responsive polymers can also be utilized in a brick-and-mortar approach to

fabricate 3D NP assemblies with dynamic optical properties. For example, bulk pNIPAM is well known for producing thermoresponsive gels that exhibit a reversible volume phase transition at its lower critical solution temperature (near 32°C).[44] By heating and cooling an Au NP-pNIPAM nanocomposite near this temperature, shrinking and swelling of the spacer layer can give rise to reversible LSPR shifts.[45, 46] (Fig. 6) More recently, Au NPs coated with a thick pNINAM shell (28 nm thick in the collapsed state at 45°C and 37 nm thick in the swollen state at 25°C) were assembled to produce 3D NP superlattices with tunable spacings over an impressive range, from 50–500 nm.[47] For the larger NP spacings, the ordered nanocomposites exhibit sharp peaks in their optical absorption spectra due to both LSPR excitation and optical diffraction effects. These NP-polymer core-shell assemblies display a fast melting and recrystallization response (< 1 min) during heating and cooling cycles, and may provide a new pathway towards the fabrication of responsive, hybrid plasmonic-photonic crystals.

2.2.3. Oriented Plasmonic Nanojunctions

A growing area of research in plasmonics is the assembly of shaped NP building blocks. Shaped metal NPs possess LSPRs that can be tuned through chemical synthesis[48] and possess compelling geometries for constructing plasmonic nanojunctions by NP coordination through facet, corner, or edge sites.[49, 50] Within these NP assemblies, electromagnetic coupling between neighboring NPs is highly sensitive to NP orientation. For two approaching NPs, van der Waals forces scale

exponentially with the surface area of interaction.[51] As a result, shaped NPs tend to organize into close-packed structures that maximize this interaction area: rods align side-by-side,[52] cubes align face-to-face (Fig. 7).[53, 54] To control plasmonic coupling, NP assembly strategies must overcome these attractive van der Waals forces. As a result, significant efforts have been directed toward developing strategies for rationally assembling shaped NP building blocks into specific geometric orientations.

Here we discuss two general strategies for achieving specific NP orientations by employing a polymer graft to tune interparticle interactions: i) site-selective modification, and ii) homogeneous surface modification.

2.2.4. Site-selective modification

To overcome the tendency of NPs to close-pack, the surface of a NP can be modified with polymer grafts such that only certain site-specific interactions are allowed.[55, 56] Site-selective modification can be achieved a number of different ways, including modification of NPs with multiple polymer grafts that segregate into separate domains at the NP surface,[57] or by forming Janus-like particles through methods such as precipitate polymerization.[58] For plasmonic building blocks that possess different shapes, site-selective modification can take advantage of the inherent chemical anisotropy of the NP surfaces or facets that are present. This has been the most well-studied for Au nanorods, which are compelling plasmonic building blocks due to their shape-dependent LSPR excitations: Au nanorods are characterized by a longitudinal dipolar LSPR that oscillates along the major axis of the nanorod and a

transverse dipolar LSPR that oscillates along the minor axis of the nanorod. Excitation of the longitudinal LSPR is responsible for the observed "lighting rod effect," where the electromagnetic field becomes focused at the nanorod tips upon irradiation with light. As a result, nanorod assembly in an end-to-end configuration is expected to result in a high degree of electromagnetic field confinement.

Several groups have succeeded in selectively tethering polymer chains to Au nanorod tips to form these desired architectures. Tip-selective modification involves a ligand exchange reaction that proceeds more readily at the nanorod tips, where the stabilizing surfactant layer is less dense and more readily displaced due to the high degree of curvature at ends of the nanorod relative to the nanorod side surfaces.[21] In the work of Nie et al., nanorod tips are modified with thiol-terminated PS chains that render the tips hydrophobic. This pseudo-triblock structure (PS-surfactant-PS) can be triggered to assemble into different orientations by adjusting solvent conditions. Adding water —a bad solvent for PS— to a dispersion of the hybrid polymer-nanorod blocks in dimethyl formamide (DMF) produces end-to-end aligned nanorod chains, resulting in a redshift of λ_{LSPR} for the longitudinal SP mode.[59] On the other hand, the addition of water to a dispersion of nanorods in tetrahydrofurane (THF) a bad solvent for the surfactant— produces nanorod bundles. (Fig. 8) Further studies have explored the dynamic generation of plasmonic hot spots during the self-assembly process to establish a direct correlation between nanorod cluster sizes and ensemble-averaged SERS intensities.[60] (Fig. 9) Chen et al. were able to generate SERS-active nanorod chains by selectively modifying the nanorod sides with PS-b-PAA grafts and leaving

the nanorod tips bare,[61] They incorporated 4-mercaptobenzoic acid into the nanorod dispersions as a SERS analyte, and observed unusual changes in the SERS fingerprint generated by molecular reorientation in the hot spots. (Fig. 9c)

Alternative routes for grafting polymers onto selective sites at the surface of a metal NP can involve a combination of top-down and bottom-up approaches. This can include surface modification of substrate-bound NPs, where the substrate serves to protect a portion of the NP surface from exposure to a particular ligand or graft.[40, 62, 63] Another top-down method involves selective surface modification using a nano-contact printing approach. For example, Rycenga et al. demonstrated that polymer grafts located on certain faces of plasmonic Ag nanocubes could be selectively displaced when in contact with an elastomer stamp inked with alkanethiol molecules. When released from the stamp and allowed to assemble in aqueous solutions, the functionalized nanocubes assemble into clusters with varying dimensions, depending on how many of the nanocube sides were modified with hydrophobic ligands (Fig. 10).[64] While such approaches can generate NPs that prefer to assemble in specific orientations, the utility of these techniques in the fabrication of plasmonic nanocomposites is severely limited by the ability to scale up these surface modification techniques for large NP quantities.

2.2.4. Homogeneous surface modification

Research efforts have also demonstrated that NP assembly with controlled inter-NP orientations can be achieved by homogeneously grafting NPs with polymer

chains. For shaped NPs, homogeneous polymer grafts can facilitate NP assembly into orientations that maximize the interaction area between neighboring NPs to obtain largest attraction when the assembly is driven by depletion attraction or linkers. For example, Au nanorods coated with a homogeneous ligand shell of polymer over the entire nanorod surface is observed to form side-to-side binding interactions (where the nanorods assemble parallel to each other) that can be reinforced by molecular linkers.[65, 66] Grzelczak and co-workers reported that this oriented nanorod clustering could also result in side-by-side nanorod orientations where the nanorods are assembled into ladder-like stacks and are slightly offset from each other. These unique structures give rise to unique "anti-bonding" surface plasmon modes in the optical absorption spectra, suggesting that these assemblies possess electromagnetic chirality.[67]

Similarly, Jones et al. demonstrated that shaped metal NPs can be driven into oriented 3D supercrystals when homogeneously grafted with DNA strands.[68] Au nanorods, Ag triangular prisms, Ag rhombic dodecahedra, and Ag octahedral organize into face-centered cubic arrangements with inter-NP orientations that maximize hybridization interactions. While DNA strands provide strong hybridization interactions that drive assembly, this study demonstrated key design concepts that can be generalized to polymer-grafted NPs that are anisotropic in shape: i) that both NP shape and polymer grafts play synergistic roles in directing NP assembly, and ii) that the length of the polymer graft often determines the relative importance of each parameter (shape or polymer) in directing inter-NP orientation. For DNA grafts, NPs

grafted with long, flexible DNA strands assemble into superstructures where inter-NP orientations are randomly generated and less influenced by NP shape.

Using linear homopolymer grafts, our research group recently demonstrated that inter-NP orientations of shaped metal plasmonic NPs can be modulated by polymer graft length. Au nanorods, Ag triangular nanoprisms, and Ag nanocubes were modified by hydrophilic end-tethered polymers and embedded into a hydrophobic polymer matrix.[69, 70] Solvent or thermal annealing of this nanocomposite drives spontaneous segregation of linear, string-like NP domains. Within these strings, inter-NP orientation is dictated by the steric interactions between polymer chains grafted on the surfaces of neighboring NPs. Monte Carlo simulations predicting the free energy profile of two approaching Ag nanocubes indicate that at a critical graft chain length, polymer-polymer repulsion can be large enough to discourage close-packed NP orientations.[69] To confirm this by experiment, we modified colloidal Ag nanocubes with both ultra-long polymer grafts (~15 nm in length as determined by dynamic light scattering measurements) and ultra-short polymer grafts (~2.0 nm in length). When grafted with long polymer chains, the nanocubes favor edge-edge (EE) orientations that alleviate the steric repulsion between adjacent, closely-spaced nanocubes. In the EE configuration, nanocube assemblies produce hot spots in the interstitial junctions between nanocube edges, evidenced by broad LSPR modes in the red wavelengths and also in electrodynamic simulations (Fig. 11). When grafted with short polymer chains, the nanocubes adopt face-face (FF) orientations favored by strong van der Waals interactions. Poor electromagnetic field localization within FF assemblies results in a

broadband scattering response for these nanocubes (Fig. 11).

The free energy profiles also indicate the presence of a phase transition between EE and FF configurations. We demonstrated this experimentally by thermally treating the NP-polymer composites for nanocubes grafted with various chain length polymers. As shown in Fig. 11d, nanocubes grafted with a short polymer chain switch from the edge-edge orientation (15.1 ± 1.9%) to face-face orientation (88.7 ± 1.8%). This reorientation of NPs may provide a convenient strategy for designing responsive plasmonic materials where such phase transitions can be predicted by theory.

2.3. Conclusions

In this review, we demonstrate different polymer-directed strategies of organizing various NP building blocks into functional plasmonic materials. For NP assembly, polymer grafting onto NP surfaces is an effective means of guiding interparticle separation distance, interparticle orientation, and aggregation. Integrating polymer-grafted NPs into plasmonic nanocomposites enables the use of convenient and facile fabrication techniques that take advantage of large-scale and low-cost production.

Chapter 2, in part, is a reformatted reprint of material from the following published paper: Gao, B., **Rozin, M. J.** and Tao, A. R. Plasmonic Nanocomposites: Polymer-Guided Strategies for Assembling Metal Nanoparticles. *Nanoscale* 5, 5677-5691, (2013) The dissertation author was the second author, or principal co-author for the above paper.

2.4. References

1. Ferry, V. E.; Sweatlock, L. A.; Pacifici, D.; Atwater, H. A., Plasmonic Nanostructure Design for Efficient Light Coupling into Solar Cells. *Nano Lett.* **2008,** *8* (12), 4391-4397.

2. Pala, R. A.; White, J.; Barnard, E.; Liu, J.; Brongersma, M. L., Design of Plasmonic Thin-Film Solar Cells with Broadband Absorption Enhancements. *Adv. Mater.* **2009,** *21* (34), 3504-3509.

3. Smith, D. R.; Padilla, W. J.; Vier, D. C.; Nemat-Nasser, S. C.; Schultz, S., Composite Medium with Simultaneously Negative Permeability and Permittivity. *Phys. Rev. Lett.* **2000,** *84* (18), 4184.

4. Shalaev, V. M.; Cai, W.; Chettiar, U. K.; Yuan, H.-K.; Sarychev, A. K.; Drachev, V. P.; Kildishev, A. V., Negative index of refraction in optical metamaterials. *Opt. Lett.* **2005,** *30* (24), 3356-3358.

5. Shalaev, V. M., Optical negative-index metamaterials. *Nat Photon* **2007,** *1* (1), 41-48.

6. Maier, S. A.; Kik, P. G.; Atwater, H. A.; Meltzer, S.; Harel, E.; Koel, B. E.; Requicha, A. A. G., Local detection of electromagnetic energy transport below the diffraction limit in metal nanoparticle plasmon waveguides. *Nat Mater* **2003,** *2* (4), 229-232.

7. Stockman, M. I., Nanofocusing of Optical Energy in Tapered Plasmonic Waveguides. *Phys. Rev. Lett.* **2004,** *93* (13), 137404.

8. Gramotnev, D. K.; Bozhevolnyi, S. I., Plasmonics beyond the diffraction limit. *Nat Photon* **2010,** *4* (2), 83-91.

9. Martin-Moreno, L.; Garcia-Vidal, F. J.; Lezec, H. J.; Pellerin, K. M.; Thio, T.; Pendry, J. B.; Ebbesen, T. W., Theory of Extraordinary Optical Transmission through Subwavelength Hole Arrays. *Phys. Rev. Lett.* **2001,** *86* (6), 1114.

10. Henzie, J.; Lee, M. H.; Odom, T. W., Multiscale patterning of plasmonic metamaterials. *Nat Nano* **2007,** *2* (9), 549-554.

11. Fan, J. A.; Wu, C.; Bao, K.; Bao, J.; Bardhan, R.; Halas, N. J.; Manoharan, V. N.; Nordlander, P.; Shvets, G.; Capasso, F., Self-Assembled Plasmonic Nanoparticle Clusters. *Science* **2010,** *328* (5982), 1135-1138.

12. Engheta, N., Circuits with Light at Nanoscales: Optical Nanocircuits Inspired by Metamaterials. *Science* **2007,** *317* (5845), 1698-1702.

13. Tao, A.; Sinsermsuksakul, P.; Yang, P., Tunable plasmonic lattices of silver nanocrystals. *Nat Nano* **2007,** *2* (7), 435-440.

14. Chen, C.-F.; Tzeng, S.-D.; Chen, H.-Y.; Lin, K.-J.; Gwo, S., Tunable Plasmonic Response from Alkanethiolate-Stabilized Gold Nanoparticle Superlattices: Evidence of Near-Field Coupling. *J. Am. Chem. Soc* **2007,** *130* (3), 824-826.

15. Tao, A.; Sinsermsuksakul, P.; Yang, P., Polyhedral Silver Nanocrystals with Distinct Scattering Signatures. *Angew. Chem. Int. Ed.* **2006,** *45* (28), 4597-4601.

16. Sun, Y.; Xia, Y., Shape-Controlled Synthesis of Gold and Silver Nanoparticles. *Science* **2002,** *298* (5601), 2176-2179.

17. Xia, X.; Zeng, J.; Oetjen, L.; Li, Q.; Xia, Y., Quantitative analysis of the role played by poly(vinylpyrrolidone) in seed-mediated growth of Ag nanocrystals. *J. Am. Chem. Soc* **2012,** *134* (3), 1793-1801.

18. Mayer, A. B. R.; Hausner, S. H.; Mark, J. E., Colloidal Silver Nanoparticles Generated in the Presence of Protective Cationic Polyelectrolytes. *Polym. J.* **2000,** *32* (1), 15-22.

19. Katz, E.; Willner, I., Integrated Nanoparticle-Biomolecule Hybrid Systems: Synthesis, Properties, and Applications. *Angew. Chem. Int. Ed.* **2004,** *43*, 6042-6108.

20. Kang, Y.; Taton, T. A., Controlling Shell Thickness in Core−Shell Gold Nanoparticles via Surface-Templated Adsorption of Block Copolymer Surfactants. *Macromolecules* **2005,** *38* (14), 6115–6121.

21. Jana, N. R.; Gearheart, L.; Murphy, C. J., Seed-Mediated Growth Approach for Shape-Controlled Synthesis of Spheroidal and Rod-like Gold Nanoparticles Using a Surfactant Template. *Adv. Mater.* **2001,** *13*, 1389-1393.

22. Park, K.; Koerner, H.; Vaia, R. A., Depletion-Induced Shape and Size Selection of Gold Nanoparticles. *Nano Lett* **2010,** *10* (4), 1433-1439.

23. Nikoobakht, B.; El-Sayed, M. A., Preparation and Growth Mechanism of Gold Nanorods (NRs) Using Seed-Mediated Growth Method. *Chem. Mater.* **2003,** *15* (10), 1957-1962.

24. Setua, P.; Pramanik, R.; Sarkar, S.; Ghatak, C.; Das, S. K.; Sarkar, N., Synthesis of Silver Nanoparticle Inside the Nonaqueous Ethylene Glycol Reverse Micelle and a Comparative Study to Show the Effect of the Nanoparticle on the Reverse Micellar Aggregates through Solvation Dynamics and Rotational Relaxation Measurements. *J. Phys. Chem. B* **2010,** *114* (22), 7557-7564.

25. Bronstein, L. M.; et; al, Interaction of Polystyrene-block-poly(ethylene oxide) Micelles with Cationic Surfactant in Aqueous Solutions. Metal Colloid Formation in Hybrid Systems. *Langmuir* **2000,** *16* (8), 3626-3632.

26. Rucareanu, S.; Maccarini, M.; Shepherd, J. L.; Lennox, R. B., Polymer-capped gold nanoparticles by ligand-exchange reactions. *J Mater. Chem.* **2008,** *18* (47), 5830-5834.

27. Love, J. C.; Estroff, L. A.; Kriebel, J. K.; Nuzzo, R. G.; Whitesides, G. M., Self-Assembled Monolayers of Thiolates on Metals as a Form of Nanotechnology. *Chem. Rev.* **2006,** *105* (4), 1103 -1170.

28. Karg, M.; Jaber, S.; Hellweg, T.; Mulvaney, P., Surface Plasmon Spectroscopy of Gold-Poly(N-isopropylacrylamide) Core-Shell Particles. *Langmuir* **2011,** *27* (2), 820-827.

29. Bishnu P. Khanal; Zubarev, E. R., Rings of Nanorods. *Angew. Chem. Int. Ed.* **2007,** *46* (13), 2195–2198.

30. Zhang, X. W.; Liu, L.; Tian, J.; Zhang, J.; Zhao, H. Y., Copolymers of styrene and gold nanoparticles. *Chem. Comm.* **2008,** (48), 6549-6551.

31. Pérez-Juste, J.; Rodriguez-Gonzalez, B.; Mulvaney, P.; Liz-Marzán, L. M., Optical Control and Patterning of Gold-Nanorod–Poly (vinyl alcohol) Nanocomposite Films. *Adv. Funct. Mater.* **2005,** *15*, 1065.

32. Wang, H.; Chen, L. Y.; Shen, X. S.; Zhu, L. F.; He, J. T.; Chen, H. Y., Unconventional Chain-Growth Mode in the Assembly of Colloidal Gold Nanoparticles. *Angew. Chem. Int. Ed.* **2012,** *51* (32), 8021-8025.

33. Yang, M. X.; Chen, T.; Lau, W. S.; Wang, Y.; Tang, Q. H.; Yang, Y. H.; Chen, H. Y., Development of Polymer-Encapsulated Metal Nanopartictes as Surface-Enhanced Raman Scattering Probes. *Small* **2009,** *5* (2), 198-202.

34. Munoz-Rojas, D.; Oro-Sole, J.; Ayyad, O.; Gomez-Romero, P., Facile one-pot synthesis of self-assembled silver@polypyrrole core/shell nanosnakes. *Small* **2008,** *4* (9), 1301-1306.

35. Guo, S. R.; Gong, J. Y.; Jiang, P.; Wu, M.; Lu, Y.; Yu, S. H., Biocompatible, luminescent silver@phenol formaldehyde resin core/shell nanospheres: Large-scale synthesis and application for in vivo bioimaging. *Adv. Funct. Mater.* **2008,** *18* (6), 872-879.

36. Gao, B.; Sarveswaran, K.; Bernstein, G.; Lieberman, M., Guided deposition of individual DNA nanostructures on silicon substrates. *Langmuir* **2009,** *26* (15), 12680-12683.

37. Duan, H.; H. Hu; Kumar, K.; Shen, Z.; Yang, J. K. W., Direct and Reliable Patterning of Plasmonic Nanostructures with Sub-10-nm Gaps. *ACS Nano* **2011,** *5* (9), 7593-7600.

38. Huang, H.-Y.; Chen, W.-F.; Kuo, P.-L., Self-Assembly of Gold Nanoparticles Induced by Poly(oxypropylene)diamines. *J. Phys. Chem. B* **2005,** *109*, 24288-24294.

39. Cho, E. C.; Choi, S.-W.; Camargo, P. H. C.; Xia, Y., Thiol-Induced Assembly of Au Nanoparticles into Chainlike Structures and Their Fixing by Encapsulation in Silica Shells or Gelatin Microspheres. *Langmuir* **2010,** *26* (12), 10005-10012.

40. Sardar, R.; Shumaker-Parry, J. S., Asymmetrically Functionalized Gold Nanoparticles Organized in One-Dimensional Chains. *Nano Lett.* **2008,** *8* (2), 731-736.

41. Lukach, A.; Liu, K.; Therien-Aubin, H.; Kumacheva, E., Controlling the Degree of Polymerization, Bond Lengths, and Bond Angles of Plasmonic Polymers. *J. Am. Chem. Soc* **2012,** *134* (45), 18853–18859.

42. Qian, X.; Li, J.; Nie, S., Stimuli-Responsive SERS Nanoparticles: Conformational Control of Plasmonic Coupling and Surface Raman Enhancement. *J. Am. Chem. Soc* **2009,** *131* (22), 7540-7541.

43. Srivastava, S.; Frankamp, B. L.; Rotello, V. M., Controlled Plasmon Resonance of Gold Nanoparticles Self-Assembled with PAMAM Dendrimers. *Chem. Mater.* **2005,** *17* (487-490).

44. Hirokawa, Y.; Tanaka, T., VOLUME PHASE-TRANSITION IN A NONIONIC GEL. *J Chem. Phys.* **1984,** *81* (12), 6379-6380.

45. Karg, M.; Pastoriza-Santos, I.; Perez-Juste, J.; Hellweg, T.; Liz-Marzan, L. M., Nanorod-coated PNIPAM microgels: Thermoresponsive optical properties. *Small* **2007,** *3* (7), 1222-1229.

46. Contreras-Caceres, R.; Pacifico, J.; Pastoriza-Santos, I.; Perez-Juste, J.; Fernandez-Barbero, A.; Liz-Marzan, L. M., Au@pNIPAM Thermosensitive Nanostructures: Control over Shell Cross-linking, Overall Dimensions, and Core Growth. *Adv. Funct. Mater.* **2009,** *19* (19), 3070-3076.

47. Karg, M.; Hellweg, T.; Mulvaney, P., Self-Assembly of Tunable Nanocrystal Superlattices Using Poly-(NIPAM) Spacers. *Adv. Funct. Mater.* **2011,** *21* (24), 4668-4676.

48. Mock, J. J.; Barbic, M.; Smith, D. R.; Schultz, D. A.; Schultz, S., Shape effects in plasmon resonance of individual colloidal silver nanoparticles. *J Chem. Phys.* **2002,** *116* (15), 6755-6759.

49. Schuck, P. J.; Fromm, D. P.; Sundaramurthy, A.; Kino, G. S.; Moerner, W. E., Improving the Mismatch between Light and Nanoscale Objects with Gold Bowtie Nanoantennas. *Phys. Rev. Lett.* **2005,** *94* (1), 017402.

50. Su, K. H.; Wei, Q. H.; Zhang, X.; Mock, J. J.; Smith, D. R.; Schultz, S., Interparticle Coupling Effects on Plasmon Resonances of Nanogold Particles. *Nano Lett.* **2003,** *3* (8), 1087-1090.

51. Israelachvili, J. N., *Intermolecular and surface forces*. Academic Press: 1992.

52. Nikoobakht, B.; Wang, Z. L.; El-Sayed, M. A., Self-Assembly of Gold Nanorods. *J Phys. Chem.B* **2000,** *104* (36), 8635-8640.

53. Chen, M.; Kim, J.; Liu, J. P.; Fan, H.; Sun, S., Synthesis of FePt Nanocubes and Their Oriented Self-Assembly. *J. Am. Chem. Soc* **2006,** *128* (22), 7132-7133.

54. Ren, J.; Tilley, R. D., Preparation, Self-Assembly, and Mechanistic Study of Highly Monodispersed Nanocubes. *J. Am. Chem. Soc* **2007,** *129* (11), 3287-3291.

55. Sau, T. K.; Rogach, A. L., Nonspherical Noble Metal Nanoparticles: Colloid-Chemical Synthesis and Morphology Control. *Adv. Mater.* **2010,** *22* (16), 1781-1804.

56. Zeng, J.; Tao, J.; Su, D.; Zhu, Y.; Qin, D.; Xia, Y., Selective Sulfuration at the Corner Sites of a Silver Nanocrystal and Its Use in Stabilization of the Shape. *Nano Lett.* **2011,** *11* (7), 3010-3015.

57. Kim, H.; Carney, R. P.; Reguera, J.; Ong, Q. K.; Liu, X.; Stellacci, F., Synthesis and Characterization of Janus Gold Nanoparticles. *Adv. Mater.* **2012,** *24* (28), 3857-3863.

58. He, J.; Perez, M. T.; Zhang, P.; Liu, Y. J.; Babu, T.; Gong, J. L.; Nie, Z. H., A General Approach to Synthesize Asymmetric Hybrid Nanoparticles by Interfacial Reactions. *J. Am. Chem. Soc* **2012,** *134* (8), 3639-3642.

59. Nie, Z.; Fava, D.; Kumacheva, E.; Zou, S.; Walker, G. C.; Rubinstein, M., Self-assembly of metal-polymer analogues of amphiphilic triblock copolymers. *Nat. Mater.* **2007,** *6* (8), 609-614.

60. Lee, A.; Andrade, G. F. S.; Ahmed, A.; Souza, M. L.; Coombs, N.; Tumarkin, E.; Liu, K.; Gordon, R.; Brolo, A. G.; Kumacheva, E., Probing Dynamic Generation of Hot-Spots in Self-Assembled Chains of Gold Nanorods by Surface-Enhanced Raman Scattering. *J. Am. Chem. Soc* **2011,** *133* (19), 7563-7570.

61. Chen, T.; Wang, H.; Chen, G.; Wang, Y.; Feng, Y.; Teo, W. S.; Wu, T.; Chen, H., Hotspot-Induced Transformation of Surface-Enhanced Raman Scattering Fingerprints. *ACS Nano* **2010,** *4* (6), 3087-3094.

62. Wang, B. B.; Li, B.; Zhao, B.; Li, C. Y., Amphiphilic Janus gold nanoparticles via combining "Solid-State Grafting-to" and "Grafting-from" methods. *J. Am. Chem. Soc* **2008,** *130* (35), 11594-11595.

63. Yoon, J. H.; Lim, J.; Yoon, S., Controlled Assembly and Plasmonic Properties of Asymmetric Core-Satellite Nanoassemblies. *ACS Nano* **2012,** *6* (8), 7199-7208.

64. Rycenga, M.; McLellan, J. M.; Xia, Y., Controlling the assembly of silver nanocubes through selective functionalization of their faces. *Adv. Mater.* **2008,** *20*, 2416-2420.

65. McLintock, A.; Hunt, N.; Wark, A. W., Controlled side-by-side assembly of gold nanorods and dye molecules into polymer-wrapped SERRS-active clusters. *Chem. Comm.* **2011,** *47* (13), 3757-3759.

66. Sreeprasad, T. S.; Samal, A. K.; Pradeep, T., One-, Two-, and Three-Dimensional Superstructures of Gold Nanorods Induced by Dimercaptosuccinic Acid. *Langmuir* **2008,** *24* (9), 4589-4599.

67. Grzelczak, M.; Mezzasalma, S. A.; Ni, W. H.; Herasimenka, Y.; Feruglio, L.; Montini, T.; Perez-Juste, J.; Fornasiero, P.; Prato, M.; Liz-Marzan, L. M., Antibonding Plasmon Modes in Colloidal Gold Nanorod Clusters. *Langmuir* **2012,** *28* (24), 8826-8833.

68. Jones, M. R.; Macfarlane, R. J.; Lee, B.; Zhang, J. A.; Young, K. L.; Senesi, A. J.; Mirkin, C. A., DNA-nanoparticle superlattices formed from anisotropic building blocks. *Nat. Mater.* **2010,** *9* (11), 913-917.

69. Gao, B.; Arya, G.; Tao, A. R., Self-orienting nanocubes for the assembly of plasmonic nanojunctions. *Nat. Nanotech.* **2012,** *7*, 433-437.

70. Gao, B.; Alvi, Y.; Rosen, D.; Lav, M.; Tao, A. R., Designer nanojunctions: orienting shaped nanoparticles within polymer thin-film nanocomposites. *Chem. Comm.* **2013,** *49*, Advance articles.

Chapter 3

Nanocube-on-Metal Metasurfaces for Tunable Light Absorbance in the Near-Infrared

3.1. Introduction

Metasurfaces are ultrathin, two-dimensional arrays of subwavelength resonators that have been demonstrated to control the flow of light in ways that are otherwise unattainable with natural materials. These arrays are typically composed of metallic Ag or Au nanostructures shaped like split-rings, nanowire pairs, or nanorods (commonly referred to as meta-atoms) that are arranged to produce a collective optical response spanning an impressive range of properties, from the perfect absorption of incident light to superresolution imaging. However, metasurfaces pose major challenges in their fabrication over large areas, which can be prohibitively expensive and time-consuming using conventional nanolithography techniques. Here we show that differently shaped colloidal nanocrystals can be organized into metasurface architectures using robust, scalable assembly methods. These metasurfaces exhibit extreme in-plane electromagnetic coupling that is strongly dependent on nanocrystal size, shape, and spacing. Colloidal metasurfaces that display near-ideal electromagnetic absorbance can be tuned from the visible into the mid-infrared wavelengths.

Colloidal nanocrystals have been successfully demonstrated as nanoscale building blocks for the assembly of large-area plasmonic metamaterials.[1-3] Metal nanocrystals serve as plasmonic meta-atoms by supporting the excitation of localized surface plasmon resonances (LSPRs), where light impinging on a metal nanostructure couples to the free electrons in the metal.[4, 5] To form a metasurface, nanocrystals must be organized into macroscale arrays that produce the optical response of an effective

medium.[6-8] Changing the size and shape of the individual nanostructures, as well as changing the arrangement and spacing within the array enables tuning of the permittivity and permeability of the metasurface without changing the dielectric environment.[9, 10] In demonstration of such an approach, Moreau and co-workers recently fabricated a near-perfect electromagnetic absorber composed of colloidal Ag nanocubes deposited onto an Au thin-film.[11] This sandwich structure produces regions of intense light confinement in the gaps between the nanocube and the Au surface. Absorbance in the visible range is tuned by controlling the dielectric spacing between these two components. To achieve metasurface operation extending into the IR wavelengths, meta-atoms that support LSPR excitation at longer wavelengths can be chosen.[12] However, this approach is limited by the ability to chemically synthesize nanocrystals within a specified size or shape range.

An alternative strategy to tailor the wavelength range and bandwidth of a colloidal metasurface is to exploit electromagnetic coupling between individual meta-atoms. Typically, when metallic nanoparticles are placed in proximity to each other, inductive or capacitive interaction between the nanoparticles will give rise to a coupled electromagnetic response.[13] Thus, in-plane coupling between meta-atoms is expected to provide an additional design variable for colloidal metasurfaces. Here, we exploit self-assembly as a powerful fabrication approach to overcome limitations in scalability, tunability, and design of colloidal metasurfaces. We examine the optical response of metasurfaces comprised of colloidal Ag nanocubes with interparticle spacings in the range of a 2-100 nm. In the case of Ag nanocubes on a metal film

(abbreviated here as NOM), in-plane coupling between neighboring nanocubes gives rise to give tunable reflectance and absorbance properties over a wide wavelength range, out to 3 μm.

3.2. Results and Discussion

3.2.1. Simulated Effects of In-Plane Coupling

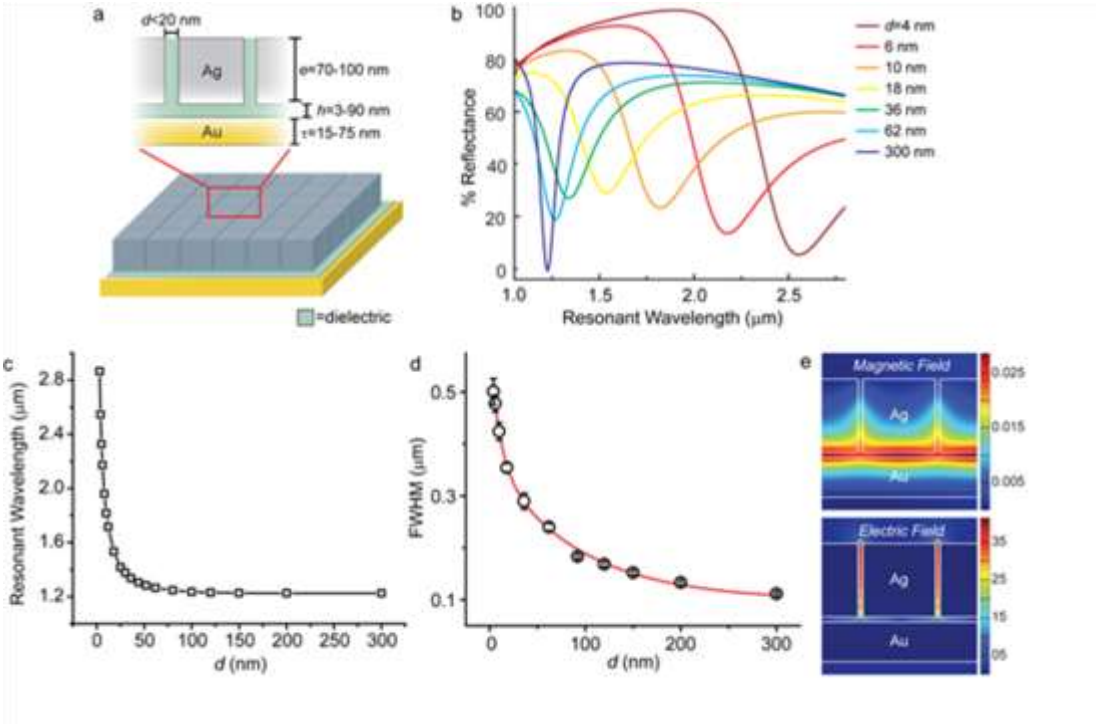

Figure 3.1. NOM metasurface geometry and simulated optical response for varying interparticle spacing. (a) Schematic of the model NOM structure with Ag nanocubes assembled atop an Au film with a dielectric spacer. Adjustable parameters include interparticle distance (*d*), length of nanocube edge (*e*), thickness of Au film (τ), and dielectric spacer height (*h*). (b) Reflectance spectra of simulated NOM arrays of 92 nm Ag nanocubes with *d*=4-300 nm. (c) Plot showing exponential trend of fundamental resonance wavelength as a function of interparticle spacing. (d) Plot of the FWHM of the fundamental resonance for decreasing *d*. (e) Magnetic and electric field intensities calculated at the fundamental resonance wavelength (λ=2.54 μm) for a close-packed NOM metasurface with *d*=4 nm. The high-field regions (red) for the H-field are supported below the nanocube, whereas they are apparent in the inter-nanocube gap for the E-field.

Previously, NOM metasurfaces with Ag nanocube surface coverages between 4-17% were examined[11]. These surface coverages are correlated to interparticle spacings of 190-350 nm where interactions between neighboring nanocubes are negligible.[14] We examined the optical response for NOM metasurfaces composed of Ag nanocubes (with edge length, e=92 nm) that possess different interparticle spacings, d, between 3-300 nm using 2D finite-difference time-domain (FDTD) simulations. (Figure 3.1.) The fundamental mode, defined as the lowest-order resonance of the metasurface, is exhibited by a sharp decrease in the reflectance spectra corresponding to near-perfect absorption (Fig. 3.1.b). The resonant wavelength of the fundamental mode shows an exponential decrease when plotted as a function of d (Fig. 3.1.c). This relationship has been well-observed for plasmonic nanoparticle pairs,[15] clusters,[16] and arrays.[17] For spacings of d=3 nm, nanocubes experience strong electromagnetic coupling and the fundamental mode is centered at λ=2.87 μm. As d is increased, this value approaches the resonance wavelength reported for a well-spaced nanowire array,[18] with λ=1.225 μm for d=300 nm. These large interparticle spacings result in an array of meta-atoms in the weak-coupling limit, where the optical resonance resembles that of an isolated particle.

Figure 3.1.d. plots the linewidth of the fundamental mode as a function of nanocube spacing. As d is increased, the linewidth sharpens significantly from 0.50 μm for d=4 nm to 0.11 μm for d=300 nm. The NOM structure exhibits significantly different behavior from electromagnetically coupled nanoparticle pairs, where the linewidth for particles spaced by <20 nm decreases to less than 50% of the linewidth

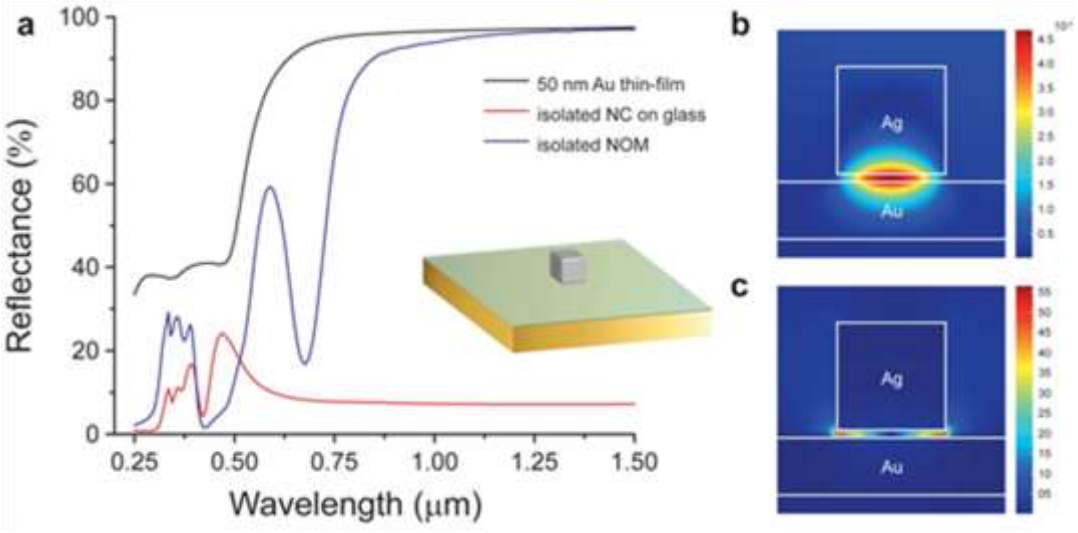

Figure 3.2. (a) Experimental reflectance spectra for an array of isolated Ag nanocubes (*e*=92 nm, *d*>300 nm) on glass (red curve), and on a 50 nm Au thin-film (blue curve), showing the significant redshift of the dipolar nanocube resonance. For reference, the reflectance for a 50 nm Au film is also plotted (black curve). For λ<425 nm, the spectral features associated with the higher-order nanocube LSPRs, there is virtually no frequency shift of these modes with the addition of the Au thin-film. For wavelengths beyond the gap-mode (λ>850 nm), the reflectance mirrors that of the underlying Au film. FDTD simulation of the (b) magnetic and (c) electric field density at the gap-mode resonance shows that the enhanced field is confined within the cavity generated by the nanocube.

observed for isolated particles.[19] This difference in linewidth behavior results from the occurrence of both out-of-plane and in-plane coupling in the NOM metasurface. Out-of-plane coupling refers to nanoparticle-surface interactions between the nanocube and the underlying metallic film. Nanoparticle-surface interactions typically result in a redshift of the dipolar LSPR without significant peak broadening[20] (see Figure 3.2.). In-plane coupling refers to interactions between neighboring nanocubes. Increasing the density of nanocubes, and thus decreasing *d* of the NOM structure, results in a quasi-continuous resonance from the coupled LSPRs of neighboring nanocubes. Out-of-plane coupling between this quasi-continuous LSPR resonance and the metal film has the effect of dramatically broadening (due to radiation damping) and red-shifting

the fundamental mode of the NOM structure. This is illustrated in Figure 3.1.e., which shows the simulated magnetic and electric field current densities for the fundamental mode (λ=2.54 μm) for the close-packed nanocube NOM structure. A quasi-continuous gap mode between the nanocubes and the metal film effectively extends across the entire metasurface. An electric field node is located in the region of greatest intensity for the corresponding magnetic field, and the region of greatest electric field intensity is located within the interstitial spaces between neighboring nanocubes. The local field volume is spread over multiple nanocubes, and for an idealized symmetric geometry, increasing the fundamental gap mode volume by approximately 2.8 times in comparison to isolated nanocubes with d>300 nm (See Section 3.2.2.).

3.2.2. Metasurface Mode Volume Calculation

We estimate mode volume using statistical image analysis to examine transmission electron microscope (TEM) images of Ag nanocube arrays. We selected only nanocubes oriented with a face precisely normal to the electron beam, as to mitigate error from the increased cross-sectional area of a plane not parallel to a nanocube facet. We measured the face-to-face edge lengths (e_1, e_2) and the radius of curvature of nanocube edges (r_e), and calculated the resulting cross-sectional area (A_{gap}) (See Equation 3.1.). Multiplying this area by the height of the gap between the nanocube and the metallic film gives an approximation of the local field volume for a

NOM metasurface with isolated nanocubes. The gap height (*h*) is the sum of the self-

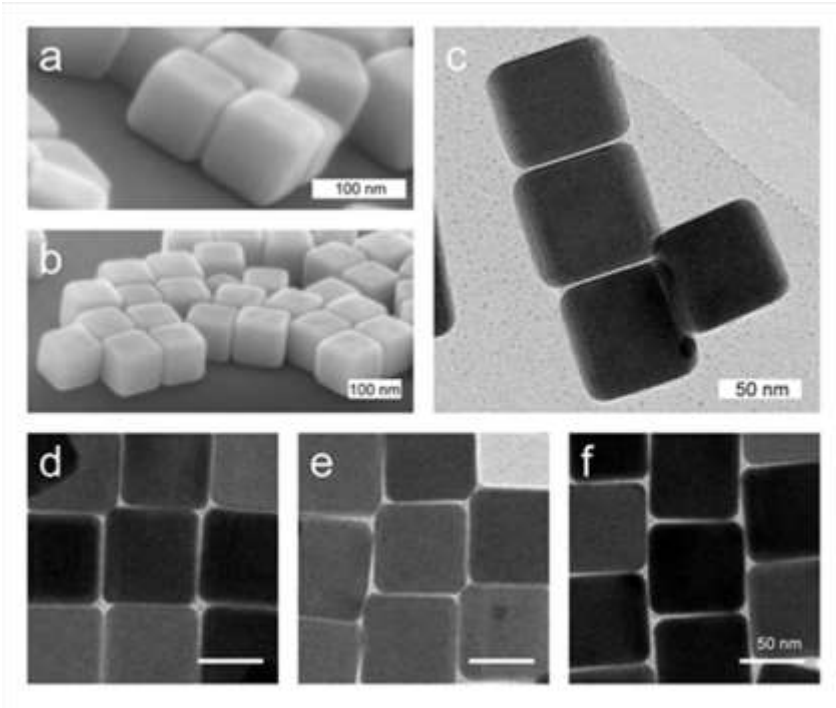

Figure 3.3. Interparticle spacing of close-packed Ag nanocubes. (a,b) SEM and (c-f) TEM images of close-packing Ag nanocubes capped with 55k M_w PVP. Nanocubes at the air-water interface have PVP chains that extend out radially for surface pressures at or near 0 mN/m. At surface pressures above ~2 mN/m, steric interactions between the polymer chains of interacting nanocubes is no longer elastic. The nanocubes interact with each other through van der Waals interactions, compressing the polymer chains between nanocube faces, creating a uniform dielectric shell around each cube. The average gap distance between nanocube faces was measured at 1.73±0.43 nm.

assembled alkanethiol monolayer height (as measured by ellipsometry) and the thickness of the compressed polymer layer encapsulating the nanocube (measured via TEM as one half the spacing between two close-packed nanocube faces).

$$A_{gap} = (e_1 \bullet e_2) - {r_e}^2[4 - \pi] \qquad (3.1.)$$

$$V_{gap} = A_{gap}\left[2.10\ nm + \tfrac{1}{2}(1.73\ nm)\right] \qquad (3.2.)$$

To determine the relative change in local field volume as we transition from the isolated to the close packed NOM metasurface, we simply adapt the above method

for TEM images of close packed Ag nanocubes. The volume between abutting nanocube faces in the close packed film was calculated by selecting a region of the film where all neighboring nanocubes lay in a single plane, which was oriented precisely normal to the incident electron beam (for a selection of images used in the analysis, see Figure 3.3., d-f). In this manner, all of the inter-nanocube spaces in the region of interest are approximately orthogonal to the image plane. We then measured the cross-sectional area of the void space surrounding a selected nanocube (A_{IP}) (See Equation 3.3.). Most of void space is formed between two approximately parallel nanocube faces, with average spacing of ~2 nm, governed by the chain length of the PVP coating. However where the nanocubes are offset, leading to a larger volume void extending away from the nanocube face, we considered the void region extending ~5 nm beyond the perimeter of the selected nanocube. This distance was chosen because it is on the order of the LSPR decay length for strongly interacting particles. We then approximate the inter-particle local field volume by multiplying the cross-sectional area of this void space by the height of the nanocube, calculated from the average of e_1 and e_2. The sum of the inter-particle volume and the nanocube-metal film gap yields the approximate volume of the local field for a close packed nanocube.

$$V_{close-packed} = \frac{A_{IP}}{2}(e_1 + e_2) + V_{gap} \qquad (3.3.)$$

This leads to an average local field volume for nanocubes (average edge length e=74.98±1.79 nm) in the close-packed NOM metasurface of approximately 2.77±0.23 times that for the metasurface with isolated nanocubes.

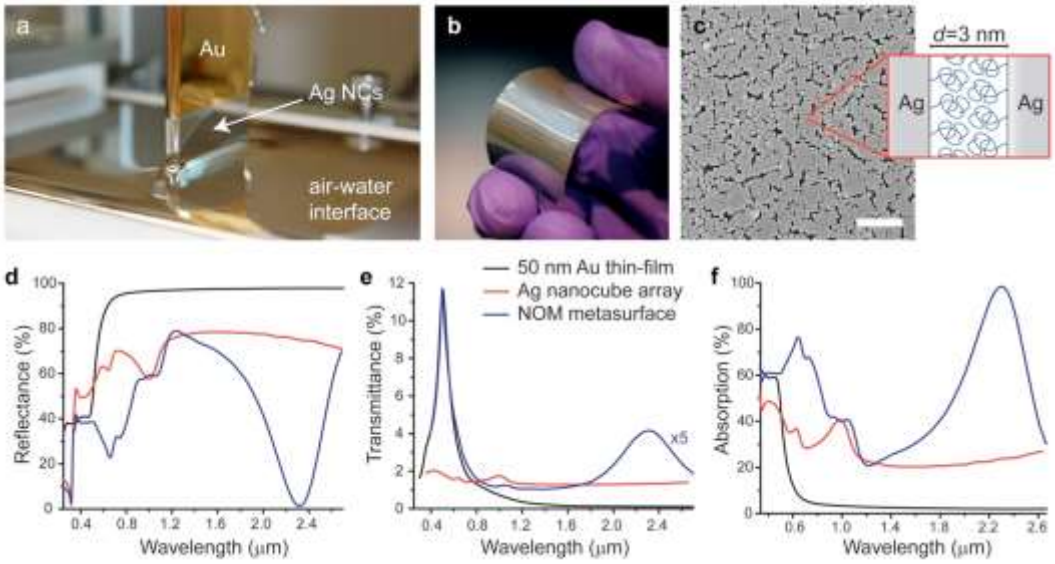

Figure 3.4. Fabrication and optical response of a NOM metasurface. (a) Image of the deposition process after Ag nanocube array assembly at an air-water interface. (b) Demonstration of metasurface fabrication onto a large-area, flexible elastomer substrate. (c) Scanning electron microscope image showing close-packed Ag nanocubes after deposition, with a measured spacing of 3 nm, which occur due to polymer grafts at the Ag surface. Scale bar = 1.0 μm. (d-f) Reflectance, transmittance, and absorbance spectra of a close-packed NOM metasurface using Ag nanocubes with *e*=92 nm, with 98% absorbance at the fundamental resonance (blue curve). For comparison, spectra for an array of close-packed Ag nanocubes (red), and a bare Au thin-film (black) are shown.

3.2.3. Experimental Demonstration of NOM Metasurface

Figure 3.4. shows the fabrication and resulting optical properties of a close-packed NOM metasurface. We employ a Langmuir-Blodgett trough to form close-packed Ag nanocube arrays[17] at an air-water interface (Fig. 3.4.a) that can then be transferred onto arbitrary substrates, including flexible and non-planar supports (Fig. 3.4.b). Ag nanocubes were synthesized using previously reported colloidal methods[21, 22] and then compressed into a dense monolayer as shown in the scanning electron microscope (SEM) image in Figure 3.4.c. Interparticle spacing within the regions of the monolayer that display domains with close packed 'face-to-face' nanocubes is

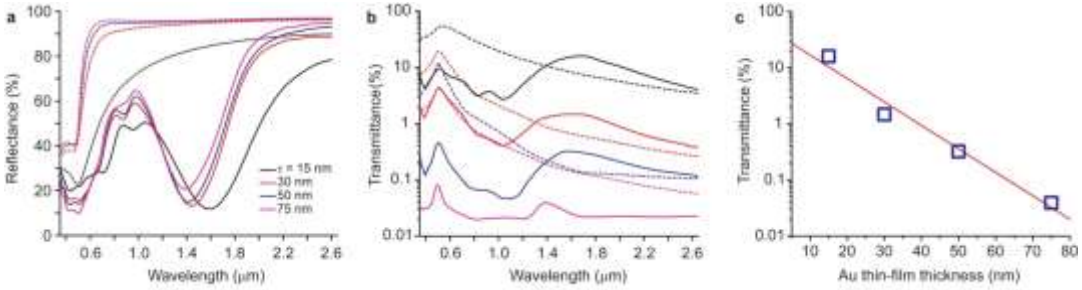

Figure 3.5. Effect of Au thin-film thickness on NOM fundamental resonance. (a,b) Near-normal reflectance and transmittance spectra for close-packed NOM structures with 70 nm Ag nanocubes and Au thin-film thickness of τ=15, 30, 50, and 75 nm. Solid lines show the optical response of the aforementioned NOM metasurfaces of varying τ, whereas dashed lines show the response for bare Au thin-films of corresponding thickness. (c) The maximum transmission at the fundamental mode of each metasurface is plotted in a semi-log fashion, where a linear increase in the Au thin-film thickness will result in a nearly exponential decrease in NOM transmittance at the resonant frequency.

controlled by the presence of long polymer grafts that passivate the nanocube surface, yielding separation distances of approximately 2-3 nm, as measured by transmission electron microscopy (Figure 3.3.). The nanocube monolayer is then transferred onto a solid support using a mechanized dip-coater. The solid support is composed of a 50 nm Au thin-film sputtered onto soda-lime glass. The Au thin-film is passivated with a molecular monolayer of alkanethiols, which serves as a dielectric spacer approximately 3 nm thick.

Figure 3.4., d-e shows the near-normal (θ=4°) reflectance and normal transmittance spectra of a close-packed NOM metasurface composed of Ag nanocubes (e=92 nm). The fundamental mode is clearly observed at λ=2.32 μm, where the reflectance spectrum exhibits a sharp decrease to a minimum percent intensity of 1.3%, correlating to an absorbance of 98% (Figure 3.4.f). In comparison, a pristine Au thin-film has a flat reflectance response of approximately 97% in the near-IR range

and a stand-alone Ag nanocube array has a reflectance intensity within a range of 71-78% at similar wavelengths. The drastic reduction in reflectance for the NOM metasurface can only be attributed to electromagnetic coupling of the nanocube array with the Au thin-film. The percent transmittance of the NOM metasurface (Figure 3.4.e) is a maximum of 0.83% at the fundamental mode wavelength. Transmittance can be further decreased by utilizing a thicker Au film as the solid support (see Figure 3.5.). It is of particular note that the entire thickness for this metasurface is approximately 150 nm—over 16 times less than the resonant wavelength of the NOM metasurface.

3.2.4. Tunable parameters of experimental NOM metasurfaces

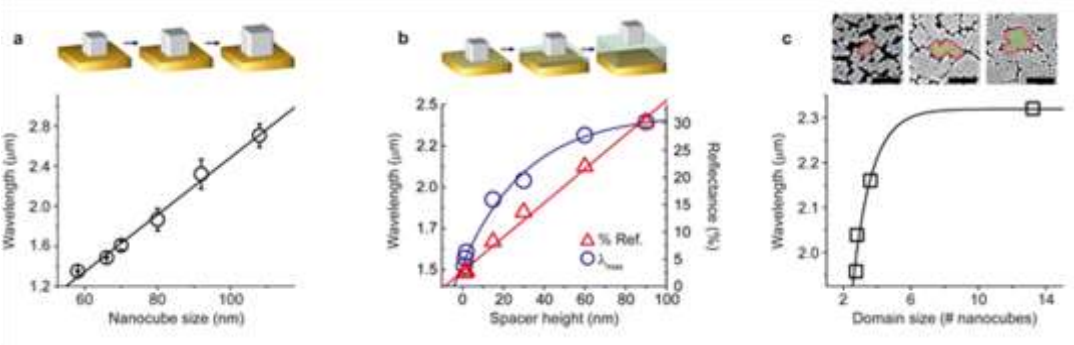

Figure 3.6. Tunable parameters of experimental NOM metasurfaces. (a) NOM metasurfaces with various sized nanocubes ranging from *e*=58-108 nm. The linear trend of the fundamental resonance wavelength as a function of nanocube size is shown (black line). Error bars display the standard deviation of the resonance wavelength position between multiple NOM metasurfaces fabricated from nanocubes with the same average size. (b) NOM metasurfaces with increasing dielectric spacer heights from a few nanometers to *h*=90 nm. As *h* is increased, the quality factor of the resonant gap is reduced, represented by the linear increase in minimum reflectance at the fundamental mode with increasing spacer height (red line). The corresponding resonant wavelength of the gap mode is shown for each metasurface at variable spacer height (blue line). (c) Representative SEM images and wavelength dependence of metasurfaces with varying nanocube domain sizes (black line). Scale bars = 500 nm.

The advantage of using this self-assembly technique is the ability to tune the resonant wavelength of the NOM metasurface using a wide range of experimental design parameters. Figure 3.6. shows metasurface architectures where the fundamental mode is tuned between 1.34-2.72 μm by changing Ag nanocube size, dielectric spacer height, or nanocube packing density and order. These results lead to some general rules regarding the performance of these self-assembled metasurfaces:

First, the wavelength of the fundamental mode increases linearly with nanocube size, owing to the linear increase in dipolar resonance wavelength for non-coupling colloidal nanocubes of increasing size (Figure 3.7.). Figure 3.6.a shows the effect of varying nanocube size on the position of the NOM fundamental resonance. The resonance position in the absorbance spectra is plotted for metasurfaces with Ag nanocubes of different sizes (*e*=59±4, 70±4, 80±8, 92±5, and 108±6 nm). The corresponding reflectance, transmittance, and absorbance spectra are accordingly

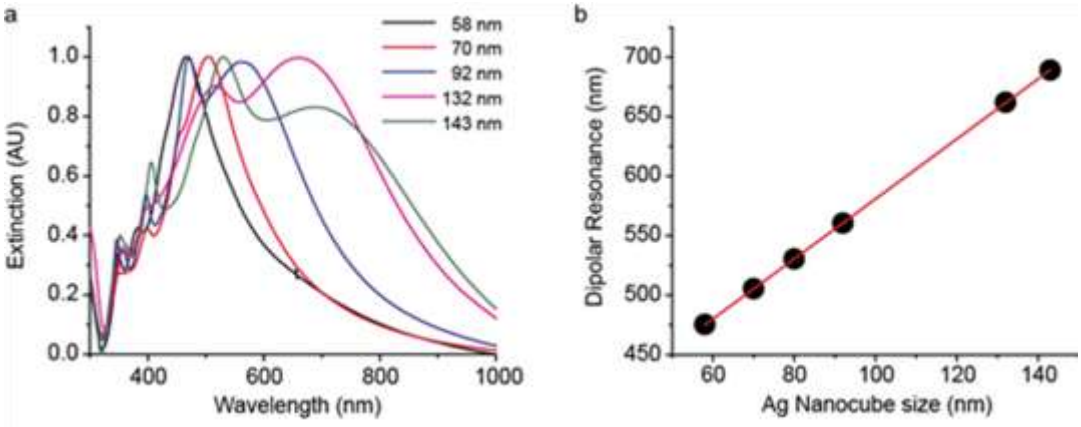

Figure 3.7. Linear trend of Ag nanocube dipolar resonance frequency with nanocube size (a) Normalized extinction spectra of colloidal Ag nanocubes with various edge lengths (*e*=58.5±3.6, 69.8±3.8, 92.3±5.1, 132.1±6.6, and 143.4±5.9 nm). (b) Trend showing the linear relationship between the dipolar LSPR wavelength of the nanocubes versus nanocube size, measured as the average nanocube edge length.

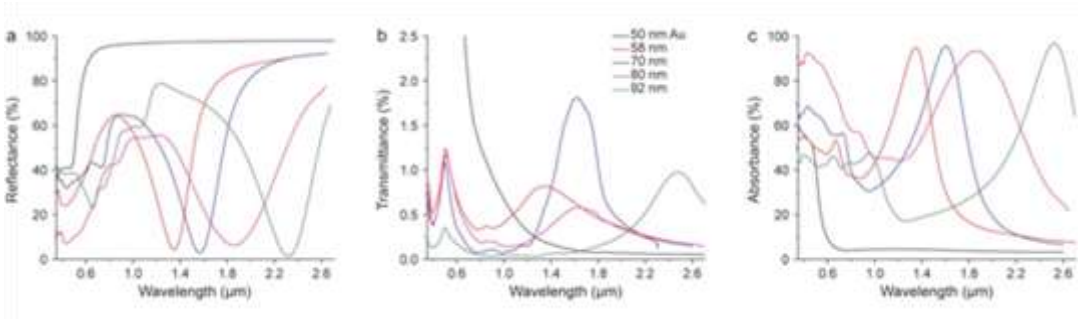

Figure 3.8. Optical response of NOM metasurfaces fabricated with nanocubes of varying size. (a) Near-normal reflectance, (b) transmittance, and (c) calculated absorbance spectra for metasurfaces with nanocubes of different edge lengths (*e*=58.5±3.6, 69.8±3.8, 80.2±7.9, and 92.3±5.1 nm).

heterogeneities in size and shape within each colloidal nanocube dispersion, as summarized in Table 3.1. Second, increasing Ag nanocube size decreases absorption efficiency of the fundamental mode. This is likely due to the increase in scattering cross-section observed for larger metal particles.[23] The NOM metasurfaces that yielded the highest reduction in reflectance were the films with *e*=70 nm and 92 nm nanocubes, with reflectance minima of 2.86% at 1.57 μm and 2.13% at 2.56 μm, respectively. Using two-dimensional FDTD simulations, we model the optical response for close-packed metasurfaces built with uniform Ag nanocubes ranging in size from 50 to 200 nm, while holding all other design parameters constant. (See

Table 3.1. Structural and optical parameters for metasurfaces with various nanocube size. Various structural and optical parameters for the metasurfaces shown in Figure 3.8. The average nanocube edge length (*e*) is varied for metasurfaces fabricated with approximately close-packed nanocube films, meaning the percent surface coverage (%SC) of nanocubes on the Au layer greater than 70%. The variation in spectral lineshape is primarily attributed to heterogeneities in size and shape within each colloidal nanocube batch.

e (nm)	%SC	*h* (nm)	λ_R (μm)	FWHM (μm)	%R (λ_R)	%T (λ_R)	%A (λ_R)
58.5 ± 3.6	72.0	~3	1.350	0.3434	4.25	0.82	92.89
69.8 ± 3.8	71.1	~3	1.566	0.4245	2.86	1.81	90.98
80.2 ± 7.9	78.4	~3	1.865	0.7810	6.16	0.58	91.71
92.3 ± 5.1	85.3	~3	2.557	0.4120	2.13	0.98	97.87

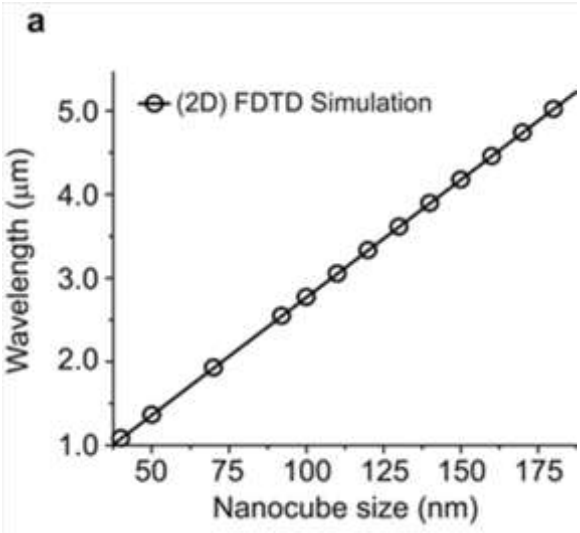

Figure 3.9. Metasurface Fundamental Mode beyond the Near-IR. (a) 2D FDTD Simulations of close-packed NOM metasurfaces with varying nanocube size from *e* = 40-200 nm. In order to extend the perfect-absorbing fundamental mode out to λ=3.0, 4.0, and 5.0 μm, NOM metasurfaces would require nanocubes with edge lengths e=108.1 nm, 143.7 nm, and 179.3 nm, respectively.

Figure 3.9.) In order to extend the perfect-absorbing fundamental mode out to λ=3.0, 4.0, and 5.0 μm, NOM metasurfaces would require nanocubes with edge lengths e=108.1 nm, 143.7 nm, and 179.3 nm, respectively.

For close-packed NOM metasurfaces, increasing gap height *h* weakens out-of-plane field confinement between the nanocubes and the Au film and increases in-plane field confinement between nanocubes. This results in a red-shift of the fundamental mode wavelength. Figure 3.6.b plots the effect of varying dielectric spacer height from 3-90 nm for NOM metasurfaces (*e*=70 nm). To achieve small *h* between 2.9-4.0 nm we varied the alkyl chain-length of the molecular monolayer covering the Au thin-film. For *h* between 15-90 nm, the height of the dielectric spacer was varied by spin-coating thin-films of poly(methyl methacrylate) (PMMA) onto the Au film prior to nanocube deposition. Intuitively, an increase in *h* should reduce the quality factor of

the resonant gap. We observe a 7-fold increase in percent transmission for NOM

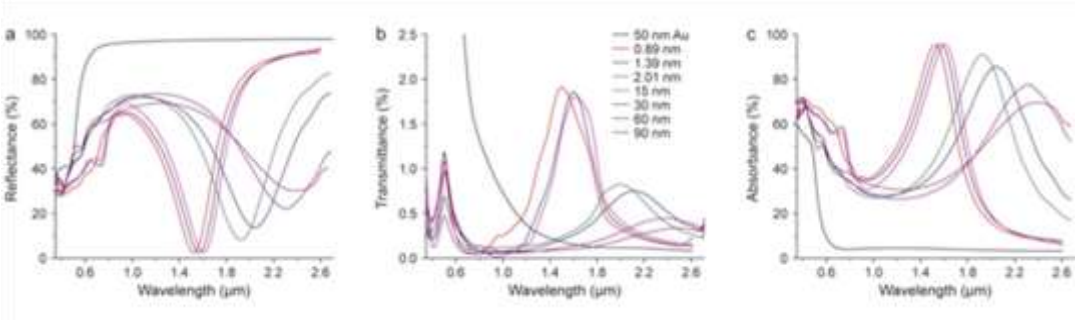

Figure 3.10. Optical response of NOM metasurfaces fabricated with dielectric spacer layer of variable height. (a) Near-normal reflectance, (b) transmittance, and (c) calculated absorbance spectra for close-packed NOM metasurfaces fabricated with 70 nm Ag nanocubes, with two regimes of variable dielectric spacer height. The first height regime used a self-assembled monolayer of one of three alkane-thiol monomers of variable chain length, with dielectric constant n=1.49. This enabled spacer heights within the extreme near-field coupling regime (h≈2.6, 3.1, and 3.7 nm). The second regime employed spin-cast PMMA layers (n=1.52) to achieve spacer heights within the strong-to-weak near-field coupling regime (h≈15, 30, 50, and 75 nm).

metasurface fabricated with these polymer dielectric spacers, but in each case the transmittance remains <2% (see Figure 3.10.). We also observe that the resonant wavelength of the fundamental gap mode redshifts with increasing h, from λ=1.52 μm at h=3 nm to λ=2.46 μm at h= 90 nm. This significant redshift is due to the increasing volume of the fundamental gap mode. This is in direct contrast to what is observed for metasurfaces composed of isolated metallic nanostructures, where, for small h (often h<50 nm), the fundamental mode wavelength blue-shifts with increasing h.[20, 24, 25] For large values of h (where $h \approx e$) we still observe a substantial suppression of reflectance at the fundamental resonance of the metasurface. This is advantageous because various dielectric materials (e.g. polymers, active materials) can be incorporated into the spacer layer without sacrificing the performance of the metasurface absorber.

We observe that the overall order of the self-assembled metasurface plays a key role in determining its optical function. Figure 3.6.c shows SEM images of three representative NOM metasurfaces, clearly showing the non-uniform spacing and

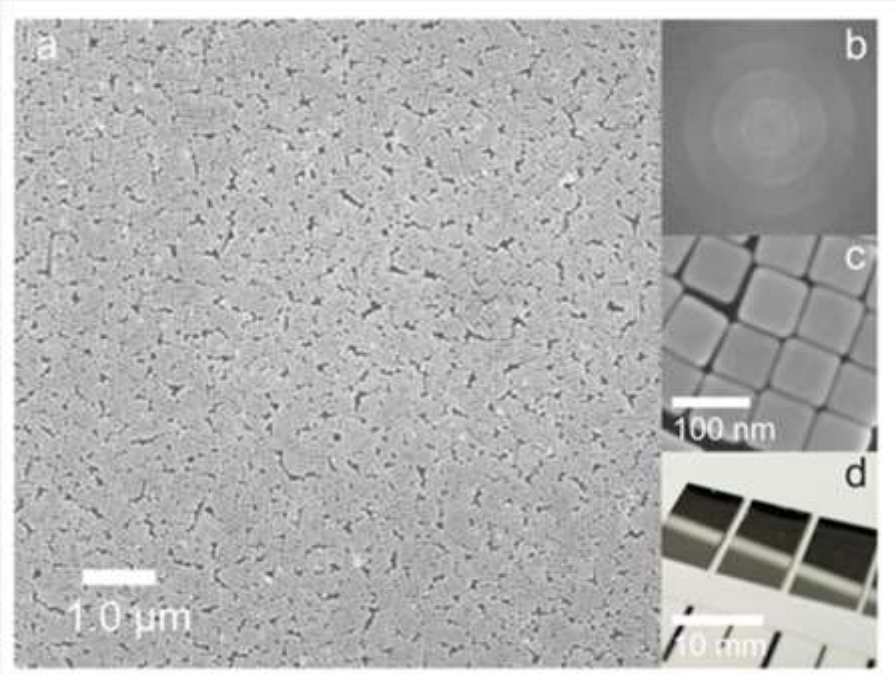

Figure 3.11. Metasurface long-range order. (a) SEM image of long-range order of Ag nanocube metasurface. (b) FFT power spectrum of 10x10 µm area, showing uniform average spacing. (c) Close-up of nanocube film order, showing close-packed face-to-face nanocubes. (d) Digital color image of as-made metasurfaces, fabricated on 10x7.5 mm substrates.

arrangement of nanocubes on the metasurface. We observe two distinct populations of inter-nanoparticle spacings: close-packed nanocubes within ordered domains ($d \approx$ 2-12 nm), and well-spaced nanocubes ($d >$ 100 nm) located at the edges of neighboring domains. The presence of these two spacing regimes over the long range order of the metasurface can be clearly seen in Figure 3.11. Because electromagnetic coupling increases exponentially with decreasing distance (Figure 3.1.c), the strong coupling between close-packed nanocubes is the primary determinant of the fundamental

resonant wavelength of the metasurface. Arrays with larger domain sizes possess better order, given that grain boundaries present defects in the array where the nanocubes are not close-packed. In the extreme limits of order and disorder, a NOM metasurface would possess an infinite domain size or a domain size of one nanocube, respectively. We have observed that the overall order of the nanocube array is likely determined by the size and shape distribution of the colloidal nanocubes; while surface chemistry also plays a role (since it dictates interparticle spacing and interactions at the air-water interface), we did not observe that the polymer ligands grafted to the nanocubes were critical in affecting domain size. Figure 3.6.c shows the resonant position of the fundamental mode for the NOM metasurfaces displayed in the SEM images, with the corresponding reflectance spectrum shown in Figure 3.12. As the film becomes more ordered, the wavelength of the fundamental mode asymptotically approaches the wavelength predicted for a perfect array (Fig. 3.1.b). This red-shift is attributed to a decrease in the average interparticle distance between nanocubes, consistent with our simulations. We also observe that an increase in domain size results in an increase in optical absorbance at the fundamental mode. Disorder within

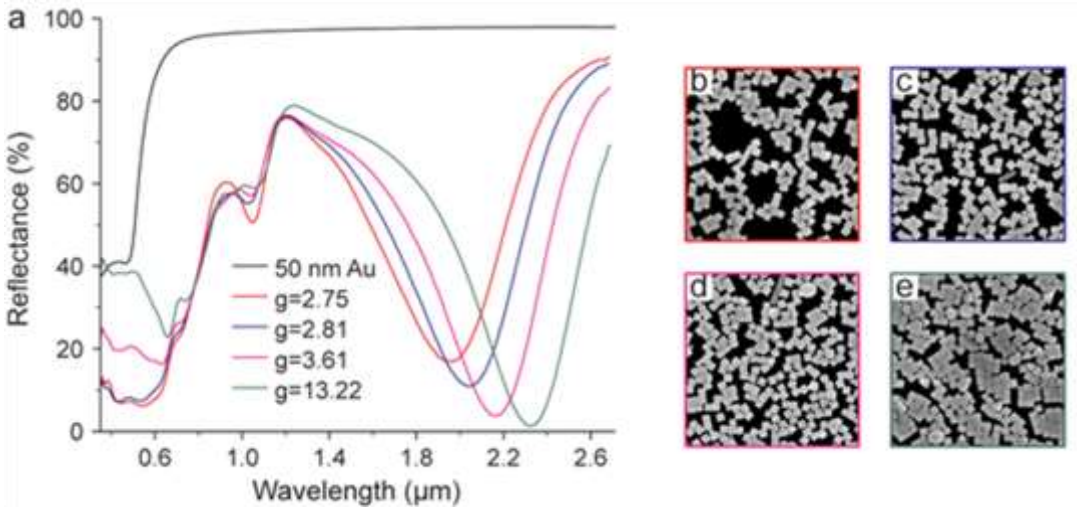

Figure 3.12. Effect of nanocube arrangement & cluster size on the NOM metasurfaces optical response. (a) Near-normal reflectance and the corresponding (b-e) SEM images for metasurfaces with varying domain sizes of g= 2.75±1.80, 2.81±1.87, 3.6±1.41, and 13.22±4.76 nanocubes. The NOM structure used 92 nm Ag nanocubes supported on a 50 nm Au thin-film by a 3 nm dielectric spacer height.

the NOM array increases the instances of isolated or poorly coupled nanocubes, contributing to radiation loss via scattering and the creation of a "leaky" fundamental gap mode.

3.2.5. Effect of Ag nanocrystal %SC and shape on gap-mode cavity

Finally, we demonstrate that these self-assembled metasurfaces can be achieved with a number of differently shaped meta-atoms. Figure 3.13. compares the optical resonances of metasurfaces composed of Ag nanocrystals with the following

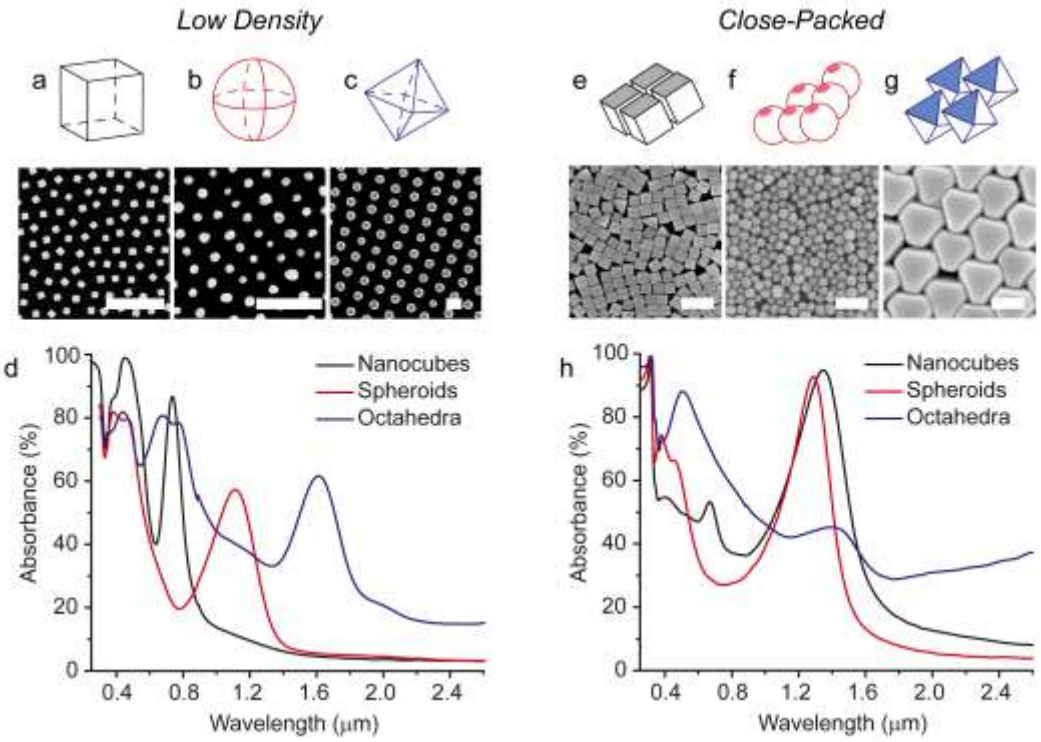

Figure 3.13. Effect of Ag nanocrystal packing density and shape on gap-mode cavity. (a-c) SEM images of well-spaced arrays of Ag cubes, spheroids, and octahedra; scale bars = 500 nm. Above each SEM image is a geometric representation of the individual nanocrystal used in each metasurface. (d) Experimental absorbance spectra for metasurface arrays with well-spaced nanocrystals of various shapes. (e-g) SEM images of close-packed metasurfaces; scale bars = 200 nm, with above diagram showing packing structure for each corresponding nanocrystal shape. (h) Experimental absorbance spectra corresponding to metasurface arrays with close-packed nanocrystals of various shapes.

shapes and sizes: cubes (59±4 nm), spheroids (65±11 nm), and octahedra (235±12 nm). We compare the optical absorbance spectra for these metasurfaces fabricated at low (Figure 3.13.,a-d) and close-packed (Figure 3.13.,e-h) nanocrystal densities. The low density metasurfaces were fabricated by depositing nanocrystal arrays with a surface coverage of ~20%, corresponding to arrays where the nanocrystals are spaced

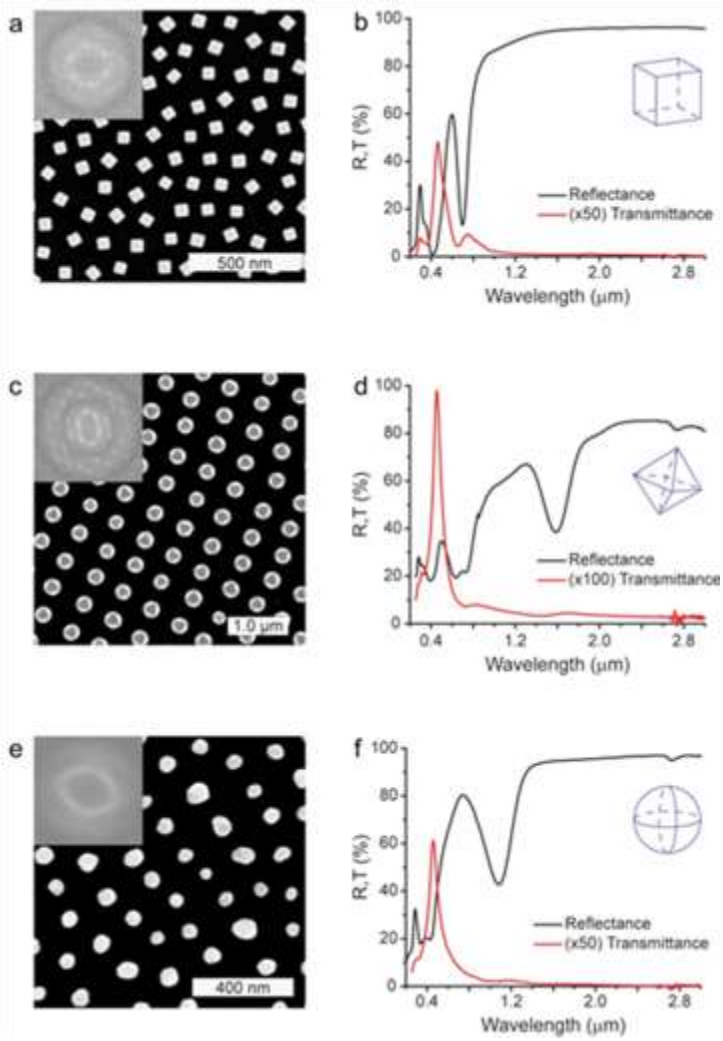

Figure 3.14. Nanocrystal shape dependence for low-density metasurfaces. SEM images corresponding to near-normal reflectance and transmittance spectra for low-density metasurfaces made with (a,b) Ag nanocubes, (c,d) Ag octahedra, and (e,f) Ag spheroids. Inset shows each nanocrystal array's FFT analysis, with greatest uniformity in nanocrystal shape and spacing for the nanocube film, and decreasing as the particles deviate from having cubic symmetry. Structural, optical, and quality parameters are listed in Supplementary Table 3.2.

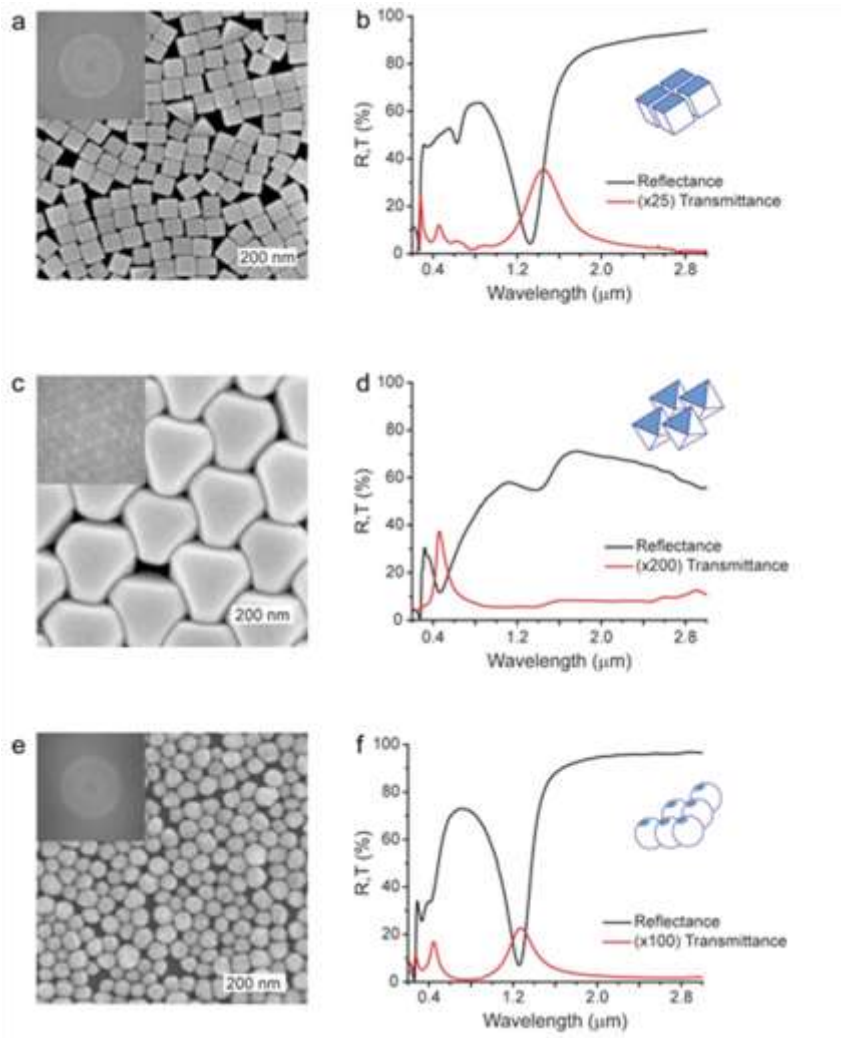

Figure 3.15. Nanocrystal shape dependence for close-packed metasurfaces. SEM images corresponding to near-normal reflectance and transmittance spectra for close-packed metasurfaces made with (a,b) Ag nanocubes, (c,d) Ag octahedra, and (e,f) Ag spheroids. Inset shows each nanocrystal array's FFT analysis. The octahedra, which close-pack to form an interlocking array, produce a well-ordered hexagonal lattice, as denoted by the spot pattern of that sample's FFT. The cubes and spheroids, which show larger size dispersity, form a random monolayer. The circular ring in each sample's FFT image denotes a monolayer where individual particles are uniformly spaced but randomly oriented, with the sharper (narrower line width) ring in the nanocube array's FFT coming from the higher degree of uniformity of the nanocube particles.

by at least two times their effective particle diameter. Close-packed metasurfaces were fabricated with nanocrystals separated by d<4 nm. Near-normal incidence reflectance and transmittance spectra were collected for each metasurface, shown in Figures 3.14.

and 3.15. Figure 3.13.,d,h shows the absorbance spectra obtained by subtracting the measured reflectance and transmittance values from 100%. For the low-density metasurfaces, the dominant peak observed in each of the absorbance spectra correspond to the fundamental optical resonance generated within the cavity between the nanocrystal and the metal thin-film. The wavelength of the fundamental mode scales with the size of the meta-atom, consistent with previous studies.[26] Percent absorbance is highest for meta-atoms that possess flat facets that lie parallel to the underlying metal film.

To compare the optical performance of each meta-atom, we use the following expression to calculate quality factor for the fundamental gap mode: $Q = \lambda_r / \delta\lambda$, where λ_r is the resonant wavelength and $\delta\lambda$ is the FWHM obtained from the absorbance spectrum. While there are numerous factors that contribute to the cavity quality of complex systems including local geometry parameters, refractive index, and absorbance coefficients,[27] this serves as a simple comparison of our three differently shaped meta-atoms. The quality factors of the three meta-atoms are described by the following relation:

$$(Q_{sphere}=3.8) < (Q_{octa}=6.1) < (Q_{cube}=7.2) \qquad (3.4)$$

This order is attributed to the shape of the nanocrystals. Both the octahedra and the nanocubes possess atomically smooth facets[16] that form a neat parallel-plate cavity with the underlying Au thin-film. Such cavities support high quality optical resonances resulting from low-loss confinement between the nanocrystal and the Au film. The shape of the octahedra is such that a significant portion of the nanocrystal

extends out beyond the footprint of the nanocrystal-film cavity, resulting in a lower *Q*

Table 3.2. Structural, optical, and quality parameters for metasurfaces with various shaped nanocrystals. Various measured parameters for low-density and close-packed metasurfaces made with Ag nanocubes, Ag octahedra, and Ag spheroids, corresponding to the metasurfaces in Supplementary Figures S11 and S12. Due to the relative large size of the Ag octahedra, close-packed metasurfaces made these particles produce a fundamental resonance beyond 3.3 μm, the maximum range of our spectrometer.

shape	packing	*e* (nm)	%SC	*d* (nm)	λ_r (μm)	FWHM (μm)	Q_f	%R (λ_r)	%T (λ_r)	%A (λ_r)
cubes	isolated	58.5 ± 3.6	21.0	133.9 ± 5.9	0.735	0.1016	7.2	13.10	0.18	86.77
	close-packed	58.5 ± 3.6	81.9	63.3 ± 1.3	1.350	0.3434	3.9	4.25	1.42	94.75
octahedra	isolated	235.3 ± 12.1	22.2	477.8 ± 97.8	1.610	0.2622	6.1	38.37	0.04	61.59
	close-packed	235.3 ± 12.1	88.0	247.9 ± 5.5	-	-	-	-	-	-
spheroids	isolated	65.3 ± 10.8	20.1	134.8 ± 19.8	1.112	0.2890	3.8	42.70	0.05	57.26
	close-packed	57.2 ± 5.6	77.1	60.3 ± 0.6	1.290	0.2725	4.7	7.10	0.23	92.67

than the nanocubes. Electromagnetic coupling between spheroids and the Au film produces gap modes where the field is poorly confined to the nanocrystal-film cavity due to the high curvature of the nanocrystal, resulting in the lowest *Q* of the three shapes. For the close-packed metasurfaces, we expect that strong coupling between the nanocrystal arrays at the Au thin-film will produce a large red-shift for the wavelength of the fundamental gap mode. This is the case for both nanocubes and octahedra. For the octahedra, this redshift is so large that the resonant wavelength of the fundamental mode is beyond the scope of our detector, past 3 μm. Electrodynamic simulations confirm that the close-packed octahedra metasurface possesses a fundamental mode near λ=3.60 μm. We attribute the absorbance peak located at λ=1.40 μm to the second-order mode of the metasurface. In contrast, close-packed Ag spheroids exhibit only a small redshift by comparison ($\Delta\lambda$=0.18 μm), with a resonant wavelength of λ=1.29 μm for the fundamental mode. While spherical nanoparticles are known to experience strong plasmonic coupling when close-packed,[28] this result shows that there is little interaction between the in-plane (i.e. interparticle) and the out-of-plane

(i.e. particle-film) gap modes. This is further confirmed by characterization of

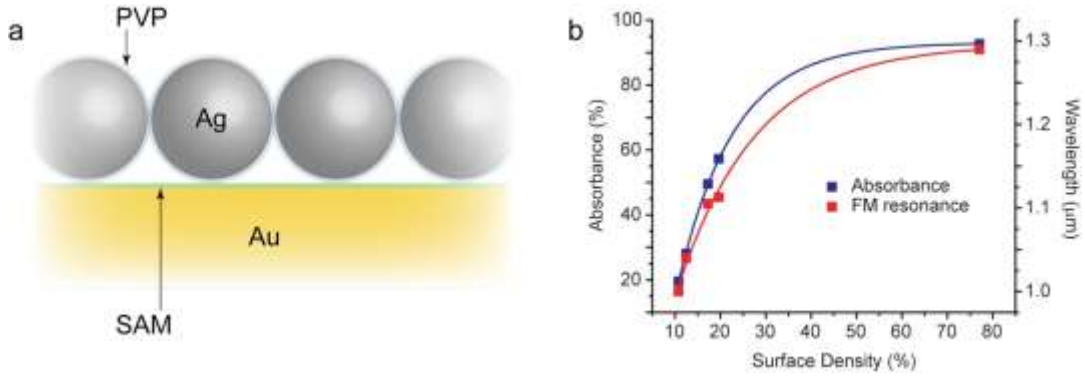

Figure 3.16. Close-packed metasurface fabricated with Ag nanospheres of varying surface densities. (a) Schematic of Ag nanosphere-on-metal metasurface, showing the reduced interaction-footprint of the particle on the underlying thin-film, as compared to a nanocube or octahedra. Metasurfaces with 65 nm Ag spheroids of varying surface density atop a 50 nm Au thin-film were fabricated. (b) Trend showing the position of the fundamental resonance, as well as the percent absorbance at that resonance vs. particle surface density. The cavity produced by two adjacent spheroids results in minimal inter-particle coupling, resulting in a direct correlation between position of the fundamental gap-mode, and percent absorbance at the gap-mode, for metasurfaces of varying surface density.

spheroid metasurfaces that possess varying nanocrystal surface coverage (see Figure 3.16.). An increase in surface coverage increases the total percent absorbance of the metasurface with little change to the *Q* of the fundamental mode, indicating that Ag spheroids behave like minimally-interacting optical resonators. This comparison between spheroids, cubes, and octahedra further highlights the importance of meta-atom shape on the ability to tune metasurface resonances into the infrared wavelengths.

3.3. Experimental and Computational Methods

3.3.1. Ag Nanocube Preparation

Ag Nanocubes were synthesized via a polyol method published elsewhere.[22] In brief, $AgNO_3$ is reduced in a solution of pentanediol, $CuCl_2$, and polyvinylpyrrolidone

(PVP) (M_w=55,000). PVP serves as a selective capping agent that controls nanocube nucleation and growth. The reaction was allowed to proceed until the resulting colloidal dispersion turned an opaque yellow-green color. To remove excess reactants, the nanocube dispersion product was centrifuged (2700 rpm for 10 min) using a Thermo Scientific CL2 Centrifuge, and the resulting precipitate was redispersed and diluted in an ethanol and water mixture, and then vacuum-filtered (Millipore Durapore membranes, with 0.65 μm, 0.45 μm, then 0.22 μm pore sizes) to remove any larger, unwanted particles. To prepare the Ag nanocubes for Langmuir-Blodgett film deposition, this dispersion is further concentrated by centrifugation (3400 rpm for 20 min) and the precipitate is redispersed in ethanol. This process was repeated three times before finally dispersing the precipitate in 1.0 mL chloroform. Ag nanocube monolayers were fabricated using a KSV Nima KN2001 Langmuir-Blodgett trough, as previously described.[17] The Ag nanocube solution was deposited drop-wise onto a deionized water (18 MΩ) subphase. The nanocube film formed at the air-water interface was allowed to sit for 30 min after deposition to allow the interfacial surface pressure to reach 0.0 mN m^{-1}. This insures complete solvent evaporation, enables excess PVP desorption into the water subphase, and allows nanocubes to disperse isotropically at the interface. The Ag nanocube film was isothermally compressed to surface pressures ranging from 0-50 mN m^{-1} prior to transfer onto a solid substrate. This transfer was carried out using a vertical dipper arm that is drawn through the air-water interface at a speed of 0.5 mm min^{-1}.

3.3.2. Substrate Preparation

Substrates for nanocube deposition were fabricated by first cleaning a soda-lime glass wafer (University Wafers) with a piranha solution (3:1 mixture of concentrated sulfuric acid and hydrogen peroxide 30% vol vol^{-1}) and plasma treatment (Harrick Plasma Cleaner PDC-002) for 300 s at 30 W. The substrates were then put into a high vacuum sputter chamber (Denton Discovery 18 Sputter System), and cleaned for 60 s with a 100W RF Ar plasma. The substrates were then sputtered with a 5 nm Ti adhesion layer, followed by a thin Au layer ranging from 15-75 nm. To generate a spacer layer between the Ag nanocubes and the Au thin-film, a dielectric layer atop the Au thin-film is necessary. To fabricate dielectric layers with variable thicknesses, we employed two general methods: (i) formation of a self-assembled monolayer (SAM) of alkanethiols on the Au thin-film to give a spacer layer on the order of a few nanometers, and (ii) a spin-coated polymer thin-film was used to provide a dielectric layer with a thickness between 15-100 nm. The SAMs were fabricated using carboxyl-terminated alkanethiols with varying length alkyl chains: 6-Mercaptohexanoic acid, 11-Mercaptoundecanoic acid, and 16-Mercaptohexadecanoic acid for dielectric layers that are approximately 0.89, 1.39, and 2.01 nm, respectively (Rudolph Auto EL Ellipsometer). The sputtered glass substrates were incubated in a 5.0 mM ethanolic solution of the desired alkanethiol for 60 min, followed by sonication in acetone for 15 min and oxygen-plasma treatment for 15 min to remove any excess physisorbed molecules. To fabricate the polymer layers, a 0.5-2.0 wt% solution of poly(methyl methacrylate) (PMMA) (M_w=25,000) in toluene was spin-coated (Laurell WS 400BZ-6NPP/lite) onto the sputtered glass substrates at different

speeds depending on the desired thickness. The thickness of the SAMs and PMMA films were verified by ellipsometry.

3.3.3. Optical Measurements

All transmittance and reflectance spectra were obtained using a Perkin-Elmer Lambda1050 UV-Vis-NIR Spectrometer. A piranha cleaned soda-lime glass wafer was used to obtain a background spectrum for the 100% transmittance reference beam. All specular reflectance measurements were taken at 4˚ near-normal incidence. Transmittance and reflectance spectra of the Ag nanocube/Au thin-films were compared with a reference spectrum of an appropriately thick Au thin-film on glass. For all reflectance and transmittance measurements, a spot-size of approximately 20 mm^2 was used, covering over 50% of the fabricated surface (excluding a ~1 mm perimeter around the edge of each substrate). This is to ensure effective measurement of the ensemble nanostructured metasurface and to provide an average over regions of variable uniformity. Absorption spectra were obtained by subtracting percent reflection and transmission from 100%.

3.3.4. FDTD Simulations

Finite difference-time domain simulations were carried out using the commercially available Lumerical FDTD Solutions utilizing the triton shared-computing cluster (TSCC) at the University of California, San Diego. Two-dimensional FDTD modeling is used to determine the nature of the electric and magnetic field confinement at the nanocube's surface and its interaction with the

adjacent metallic film. Due to the model's two-dimensional geometry the higher order modes of the silver cube are skewed, because they tend to involve multiple faces of the cube simultaneously. This model does not take into account quantum effects, which are typically observed when the geometry of the simulations start to approach dimensions of approximately 2 nm. A two-dimensional model was used to cut down the computational costs and due to the ease of implementing periodic boundary conditions.

3.4. Conclusions

Our work demonstrates that metasurfaces enabled by self-assembly can be fabricated in a scalable, robust, and tunable manner. This work paves the way for such advances in metamaterials development, and specifically in the demonstration of large-area assembly techniques based on dip-coating. We expand the active optical range of colloidal metasurfaces from the visible to the mid-IR wavelengths by utilizing in-plane light confinement between meta-atoms and by tuning meta-atom parameters such as size, shape, and arrangement. These colloidal metasurfaces exhibit extreme light confinement, with subwavelength optical cavities that possess dimensions less than 200 nm and operating wavelengths of a few microns. While these colloidal metasurfaces exhibit extreme light confinement, our highest performing metasurfaces are less-than-perfect and exhibit 98% absorbance at the fundamental resonance wavelength. In addition, assembly defects likely play a major role in limiting the uniformity and bandwidth of metasurface performance. Future work will examine the defect tolerance and the possibility of defect engineering for these

colloidal metasurfaces, and may provide new methods for designing the structure and function of metamaterials architectures.

Chapter 3 is a reformatted reprint in full, of the material from: **Rozin, M. J.**, Rosen, D., Dill, T. J. and Tao, A. R. Colloidal Metasurfaces Displaying Near-Ideal and Tunable Light Absorbance in the Infrared. *Nature Communications* 6, (2015). The dissertation author was the principal researcher and author of this paper.

3.5. References

1. Ciracì, C.; Hill, R. T.; Mock, J. J.; Urzhumov, Y.; Fernández-Domínguez, A. I.; Maier, S. A.; Pendry, J. B.; Chilkoti, A.; Smith, D. R., Probing the Ultimate Limits of Plasmonic Enhancement. *Science* **2012,** *337* (6098), 1072-1074.

2. Gao, B.; Rozin, M. J.; Tao, A. R., Plasmonic nanocomposites: polymer-guided strategies for assembling metal nanoparticles. *Nanoscale* **2013,** *5* (13), 5677-5691.

3. Rycenga, M.; Cobley, C. M.; Zeng, J.; Li, W.; Moran, C. H.; Zhang, Q.; Qin, D.; Xia, Y., Controlling the Synthesis and Assembly of Silver Nanostructures for Plasmonic Applications. *Chemical Reviews* **2011,** *111* (6), 3669-3712.

4. Landy, N. I.; Sajuyigbe, S.; Mock, J. J.; Smith, D. R.; Padilla, W. J., Perfect Metamaterial Absorber. *Physical Review Letters* **2008,** *100* (20), 207402.

5. Kildishev, A. V.; Boltasseva, A.; Shalaev, V. M., Planar Photonics with Metasurfaces. *Science* **2013,** *339* (6125).

6. Pors, A.; Albrektsen, O.; Radko, I. P.; Bozhevolnyi, S. I., Gap plasmon-based metasurfaces for total control of reflected light. *Sci. Rep.* **2013,** *3*.

7. Sun, S.; Yang, K.-Y.; Wang, C.-M.; Juan, T.-K.; Chen, W. T.; Liao, C. Y.; He, Q.; Xiao, S.; Kung, W.-T.; Guo, G.-Y.; Zhou, L.; Tsai, D. P., High-Efficiency

Broadband Anomalous Reflection by Gradient Meta-Surfaces. *Nano Letters* **2012,** *12* (12), 6223-6229.

8. Ni, X.; Emani, N. K.; Kildishev, A. V.; Boltasseva, A.; Shalaev, V. M., Broadband Light Bending with Plasmonic Nanoantennas. *Science* **2012,** *335* (6067), 427-427.

9. Kanté, B.; de Lustrac, A.; Lourtioz, J. M., In-plane coupling and field enhancement in infrared metamaterial surfaces. *Physical Review B* **2009,** *80* (3), 035108.

10. Dolling, G.; Enkrich, C.; Wegener, M.; Zhou, J. F.; Soukoulis, C. M.; Linden, S., Cut-wire pairs and plate pairs as magnetic atoms for optical metamaterials. *Opt. Lett.* **2005,** *30* (23), 3198-3200.

11. Moreau, A.; Ciraci, C.; Mock, J. J.; Hill, R. T.; Wang, Q.; Wiley, B. J.; Chilkoti, A.; Smith, D. R., Controlled-reflectance surfaces with film-coupled colloidal nanoantennas. *Nature* **2012,** *492* (7427), 86-89.

12. Zhang, S.; Fan, W.; Panoiu, N. C.; Malloy, K. J.; Osgood, R. M.; Brueck, S. R. J., Experimental Demonstration of Near-Infrared Negative-Index Metamaterials. *Physical Review Letters* **2005,** *95* (13), 137404.

13. Hentschel, M.; Saliba, M.; Vogelgesang, R.; Giessen, H.; Alivisatos, A. P.; Liu, N., Transition from Isolated to Collective Modes in Plasmonic Oligomers. *Nano Letters* **2010,** *10* (7), 2721-2726.

14. Liu, N.; Weiss, T.; Mesch, M.; Langguth, L.; Eigenthaler, U.; Hirscher, M.; Sönnichsen, C.; Giessen, H., Planar Metamaterial Analogue of Electromagnetically Induced Transparency for Plasmonic Sensing. *Nano Letters* **2009,** *10* (4), 1103-1107.

15. Atay, T.; Song, J.-H.; Nurmikko, A. V., Strongly Interacting Plasmon Nanoparticle Pairs: From Dipole−Dipole Interaction to Conductively Coupled Regime. *Nano Letters* **2004,** *4* (9), 1627-1631.

16. Fan, J. A.; Wu, C.; Bao, K.; Bao, J.; Bardhan, R.; Halas, N. J.; Manoharan, V. N.; Nordlander, P.; Shvets, G.; Capasso, F., Self-Assembled Plasmonic Nanoparticle Clusters. *Science* **2010,** *328* (5982), 1135-1138.

17. Tao, A.; Sinsermsuksakul, P.; Yang, P., Tunable plasmonic lattices of silver nanocrystals. *Nat Nano* **2007,** *2* (7), 435-440.

18. Alaee, R.; Menzel, C.; Huebner, U.; Pshenay-Severin, E.; Bin Hasan, S.; Pertsch, T.; Rockstuhl, C.; Lederer, F., Deep-Subwavelength Plasmonic Nanoresonators Exploiting Extreme Coupling. *Nano Letters* **2013,** *13* (8), 3482-3486.

19. Dahmen, C.; Schmidt, B.; von Plessen, G., Radiation Damping in Metal Nanoparticle Pairs. *Nano Letters* **2007,** *7* (2), 318-322.

20. Holland, W. R.; Hall, D. G., Frequency Shifts of an Electric-Dipole Resonance near a Conducting Surface. *Physical Review Letters* **1984,** *52* (12), 1041-1044.

21. Tao, A.; Sinsermsuksakul, P.; Yang, P., Polyhedral Silver Nanocrystals with Distinct Scattering Signatures. *Angewandte Chemie International Edition* **2006,** *45* (28), 4597-4601.

22. Sun, Y.; Xia, Y., Shape-Controlled Synthesis of Gold and Silver Nanoparticles. *Science* **2002,** *298* (5601), 2176-2179.

23. Near, R.; Hayden, S.; El-Sayed, M., Extinction vs Absorption: Which Is the Indicator of Plasmonic Field Strength for Silver Nanocubes? *The Journal of Physical Chemistry C* **2012,** *116* (43), 23019-23026.

24. Nielsen, M. G.; Gramotnev, D. K.; Pors, A.; Albrektsen, O.; Bozhevolnyi, S. I., Continuous layer gap plasmon resonators. *Optics Express* **2011,** *19* (20), 19310-19322.

25. Lassiter, J. B.; McGuire, F.; Mock, J. J.; Ciracì, C.; Hill, R. T.; Wiley, B. J.; Chilkoti, A.; Smith, D. R., Plasmonic Waveguide Modes of Film-Coupled Metallic Nanocubes. *Nano Letters* **2013**.

26. Wang, H.; O?Dea, K.; Wang, L., Selective absorption of visible light in film-coupled nanoparticles by exciting magnetic resonance. *Opt. Lett.* **2014,** *39* (6), 1457-1460.

27. Ferry, V. E.; Sweatlock, L. A.; Pacifici, D.; Atwater, H. A., Plasmonic Nanostructure Design for Efficient Light Coupling into Solar Cells. *Nano Letters* **2008,** *8* (12), 4391-4397.

28. Chen, C.-F.; Tzeng, S.-D.; Chen, H.-Y.; Lin, K.-J.; Gwo, S., Tunable Plasmonic Response from Alkanethiolate-Stabilized Gold Nanoparticle Superlattices: Evidence of Near-Field Coupling. *Journal of the American Chemical Society* **2007,** *130* (3), 824-826.

Chapter 4

Enhanced Second Harmonic Generation in Colloidal Metasurfaces

4.1. Introduction

The ability to efficiently generate and control nonlinear optical effects at the nanoscale promises novel functionalities for fundamental research and applications, as well as scaling down nonlinear optical components for integration with existing silicon nanofabrication. Optical metamaterials have garnered an extraordinary amount of interest in recent years, and initial metamaterial-based nonlinear optical media have been shown to demonstrate numerous nonlinear phenomena previously only observed with traditional bulk media[1, 2]. The technological significance of nanoscale nonlinear light sources is most evident for various nascent fields such as all-optical communication[3] and novel nonlinear biomedical imaging[4]. We present a highly scalable, bottom-up approach to fabricating two-dimensional arrays of resonant nanostructures for nonlinear light generation. Heretofore, nanostructured nonlinear optical media has predominantly relied on direct-write or lithography-based nanofabrication techniques. While suitable for building proof-of-concept structures, such fabrication processes are not amenable to production aspects such as scaling, throughput, and cost. In this paper we demonstrate an alternative; a colloidal synthetic and self-assembly based approach for nonlinear optical metasurfaces fabrication.

The first experimental verification of a nonlinear optical process was in 1961, with the observation of second harmonic generation (SHG) from a quartz crystal.[5] SHG is a nonlinear wave mixing process where two incident photons at the same fundamental wavelength (λ_{FW}) combine to produce a single, higher energy photon at double the fundamental frequency ($\lambda_{SH} = \lambda_{FW}/2$), or second harmonic. The discovery

utilized a first-of-its-kind high energy light source demonstrated just a year earlier—the ruby laser.[6] The "extraordinary intensity" of the optical fields produced by the focused laser beam, with incident energy approaching 10^5 $V \cdot cm^{-1}$, was seen as requisite for generation of a higher harmonic; due to the inherently weak intrinsic nonlinear response of most materials. Just as with a material's linear optical response—where the medium's (linear) polarization oscillating with the frequency of the incident light gives rise to conventional optical effects such as absorption and scattering—the origin of second order generation comes from the nonlinear polarization oscillating at the second harmonic frequency. (See Equation 4.1.) Because nonlinear polarization—and thus SHG—results from the interaction of the incident wave with the second-order nonlinearity of the medium, SHG intensity depends on the degree of nonlinearity of the medium, referred to as the nonlinear susceptibility[7]. Traditional nonlinear media is comprised of a bulk optical crystal with noncentrosymmetric atomic lattice, such as β-barium borate (BBO) and lithium niobate ($LiNbO_3$). Efficient light generation from such nonlinear crystals requires significant interaction length of the incident beam in the nonlinear media, high transparency at both fundamental and higher harmonic wavelengths, as well as fulfilling a phase matching condition between the incident beam and nonlinear crystal.

$$\boldsymbol{P} = \varepsilon_0\left[\chi^{(1)}\boldsymbol{E} + \chi^{(2)}\boldsymbol{E}^2 + \chi^{(3)}\boldsymbol{E}^3 + \cdots\right] \qquad (4.1.)$$

Equation 4.1 | Polarization ($\boldsymbol{P}$) is defined as the response of a material to an electromagnetic field ($\boldsymbol{E}$), where each term of increasing order gives rise to a

polarization oscillating at the corresponding frequency[1]. ε_0 is the vacuum permittivity and $\chi^{(n)}$ is the nth order susceptibility of the material.

However, it has recently been shown that nanoscale structures can also be used as nonlinear optical media, through the inherent symmetry breaking at the local interface at a nanostructure's surface. Although metasurfaces utilizing various materials and arrangements have been shown to demonstrate nonlinear responses, including dielectric[8], metallic[9-11], and composite designs[12-14], the greatly reduced interaction length available at the nanoscale poses a major hurdle to such metamaterial light sources for practical nonlinear applications. Metallic nanostructures pose a distinct advantage: their unique ability to couple propagating light from the far-field into deep subwavelength confined volumes greatly enhances the intensity of the incident optical field. Such confined optical fields, or localized surface plasmon resonances (LSPRs), stem from coherent oscillations of conduction band electrons in the metal resonating with the incident optical field. The enhanced optical near-fields generated from strongly confined LSPRs boosts the nonlinear polarization derived from the anisotropy at the interface of the metal and its environment. This makes plasmonic metasurfaces well-suited for nonlinear optical media, as the reduced interaction/path length associated with a flat surface is overcome by the heightened nonlinear response provided strong enhanced near-fields.

4.2. Results and Discussion

4.2.1. Nonlinear Optical Emission from Colloidal Metasurfaces

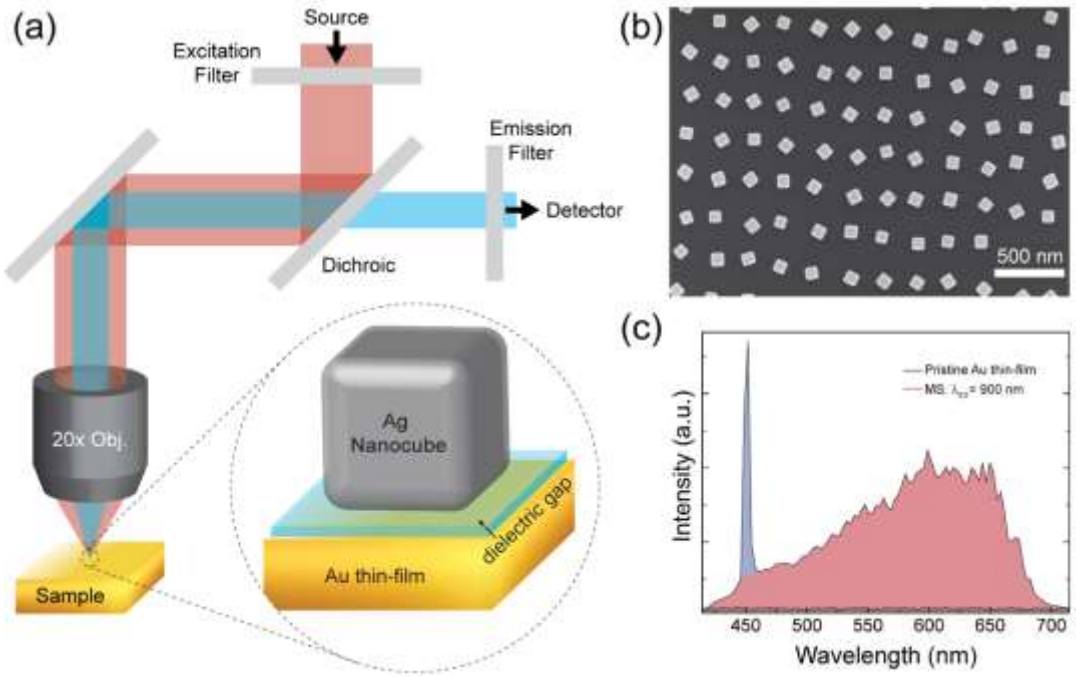

Figure 4.1 Wafer-Scale Colloidal Metasurface Displaying Strong Nonlinear Optical Emission. (a) Optical setup & metasurface schematic (inset). (b) SEM image of nanocube metasurface displaying well-spaced NC array. (c) Typical metasurface nonlinear emission.

We analyze enhanced nonlinear light generation from a nanocube-on-metal metasurface based on the film-coupled colloidal nanoantenna metasurface first reported by Moreau et al.[15] The nanocube metasurface is of particular interest to higher-harmonic generation for its ability to support multiple, spectrally separated but spatially overlapping resonances with strongly enhanced optical fields. A schematic of the metasurface geometry is shown in Figure 4.1.a (inset). The structure is composed of a well-spaced, nominally-periodic array of colloidal, cubic Ag nanocrystals assembled on top of a substrate-supported 50 nm Au film. Each nanocube is encapsulated in a thin (~2 nm) polymer shell, providing a spacer layer which insulates the nanocube from the continuous Au film underneath. This nanocube–spacer–film

junction behaves effectively like a metal-dielectric-metal interface, and serves as the artificially structured repeating unit, or meta-atom, within our metasurface. The simple, primarily self-assembly driven fabrication of such colloidal metasurfaces affords a direct path for producing highly tunable, scalable, and Si-compatible media for nonlinear optics.

The facile fabrication of this colloidal nanocrystal metasurfaces is described, with greater procedural detail outlined in the supporting information. Ag nanocubes were synthesized according to a modified polyol reaction, described in detail elsewhere[16]. The as-synthesized colloidal solution contains polymer-capped Ag nanocrystals—both nanocubes and a variety of unwanted non-cubic 'defect' nanocrystals—as well as excess reactants dispersed in 1,5-pentanediol. Defect nanocrystals larger in size than the average nanocube are removed via multiple vacuum filtrations, using successively smaller membrane filters. Excess reactants and small defect nanocrystals are removed via multiple cycles of centrifugation, redispersing the nanocube-enriched precipitate in pure EtOH each time, and finally concentrated into pure $CHCl_3$. The purified and concentrated nanocube solution was then added drop-wise to the air-water interface of a Langmuir-Blodgett trough, and allowed to equilibrate for ~20 min. The barriers of the trough were isothermally compressed until a positive surface pressure was detected, and a mechanical dipper was used to transfer the Ag nanocube array onto a 50 nm Au thin-film sputtered onto a silicon substrate. Figure 4.1.b shows a (top-down) SEM image of the nanocube metasurface, fabricated with nanocubes possessing an average edge length of 89±4

nm. The nanocube array has an average nanocube center-to-center spacing of 224±45 nm, and a nanocube purity of >98% (particle defect rate of <2%).

We measure the nonlinear optical response of the colloidal metasurface using a confocal scanning microscope in back-scattering collection mode. A tunable Ti-Sapphire laser was used as the excitation source with approximately 100 femtosecond pulse width, 80 MHz repetition rate, and tunable emission from 690–1040 nm. Figure 4.1.a shows a simplified schematic of the experimental setup for measuring SHG. The following briefly describes a typical SHG measurement; greater detail can be found in the supporting information. First, the metasurface is excited with a beam of short-pulsed, high-energy illumination at the chosen fundamental wavelength (e.g. λ_{FW}=900 nm). The beam of near-IR pulses is transmitted through a longpass dichroic filter/beam-splitter and focused through a 0.75 NA 20x dry objective, onto the surface of the sample. The visible nonlinear optical (NLO) emission generated by the metasurface is collected back through the 20x objective, and reflected by the dichroic mirror, which rejects any back-scattered NIR light. The collected light then passes through a shortpass filter, monochromator, and finally detected via GaAsP hybrid PMT (Leica). The spectral resolution of the NLO emission is limited by the minimum detection bandwidth of the monochromator— around 5 nm—resulting in the observed granularity of the emission curve. A typical metasurface NLO emission spectrum is shown in Figure 4.1.c, excited with a scanning, normal incidence pulse train with λ_{FW}=900 nm. The narrow SHG peak is prominent in the emission spectrum at precisely one-half λ_{FW}, λ_{SH}=450 nm (colored blue). The other prominent feature is the

expansive range of cathedral-like peaks (colored red) throughout the visible spectrum; most likely produced by multi-photon mediated photoluminescence. These broadband background NLO emission peaks span 420–700 nm; however, detection at either end of the visible spectrum is limited by cutoff filters and the detector's range. Their investigation is outside the primary scope of the present work and has been reported elsewhere.[17] For comparison, NLO emission from a pristine Au thin-film (*sans* nanocubes) is shown with an identical illumination configuration, which, for such relatively low power, reveals a featureless spectrum equivalent to near-zero emission (colored grey).

4.2.2. Nonlinear Optical Emission from Colloidal Metasurfaces

Figure 4.2.a shows the excitation-wavelength-dependent nonlinear spectra for a typical colloidal nanocube metasurface, for λ_{FW}=900, 910, and 920 nm. Each nonlinear emission spectrum is composed of narrow, coherent SH signal (blue) on top of a broadband incoherent multiphoton emission background (red). The measured experimental metasurface emission confirms the presence of SHG, with a spectrally narrow SH peak (FWHM < 6 nm) whose position follows a strict $\lambda_{FW}/2$ dependence. Unlike the SHG emission, the broad multiphoton emission does not experience a spectral shift with varying incident wavelength, confirming an incoherent mechanism caused by a convolution of multiple NLO emission pathways. The power dependence of the SHG signal is shown in Figure 4.2.b. The second harmonic intensity was found to increase superlinearly with excitation power, with a nonlinearity order of approximately 1.9 after accounting for the multiphoton emission background. Other

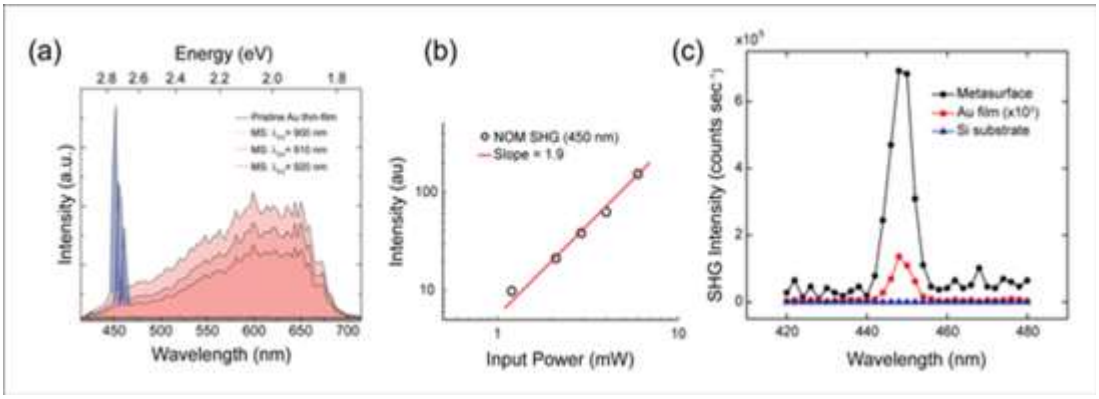

Figure 4.2. Wavelength and Power Dependence of Metasurface Second Harmonic Generation (a) Nonlinear emission spectra, showing λ_{FW}-dependent SHG. (b) SHG power dependence, showing SHG is a 2nd-order NLO process. (c) Metasurface second harmonic enhancement factor.

multi-photon resonant emission channels are evident in the NLO spectra.

We calculated SHG enhancement to compare our metasurface performance to others reporting plasmonic-based SHG[9]. SHG enhancement factor (EF) is defined as the ratio of metasurface SHG power (P_{MS}) over the SHG power of an un-patterned Au thin-film (P_{Au}). First, we measured the nonlinear emission for each constituent part of the metasurface: isolated Ag nanocubes on Si, the bare Au film, and a pristine Si substrate (Figure 4.2.c). The parameters of the metasurface used are as follows: Ag nanocubes with 87.5 ± 3.8 nm average size, nanocube surface density of 12.1%, and Au thin-film with 75 nm thickness. Using incident excitation power of 3.80 mW at 900 nm, we measured SHG power to be $P_{MS} = 2.20 \times 10^{-13}$ W. We then compared this to a pristine Au film—identical to the one used in constructing the metasurface. Because the unenhanced SH signal from the bare Au film is much weaker, higher pump power was required to detect unambiguous SHG. Using incident excitation power of 264.75 mW at 900 nm, we measured the SHG power of the Au film to be $P_{Au} = 7.00 \times 10^{-14}$ W (equivalent to 1.45×10^{-17} W at 3.80 mW incident power).

This gives a metasurface SHG enhancement factor of $EF_{MS} = 1.52 \times 10^4$. The metasurface and Au thin-film SHG spectra are shown in Figure 4.2.c, normalized to accommodate for pump power. Included is the SHG spectra obtained from exciting the bare silica substrate under the same conditions (blue triangles). We then calculated the SHG efficiency of the metasurface, defined as the ratio of the fundamental beam power ($P_{FW} = 3.80 \times 10^{-3}$ W) to the metasurface SHG power:

$$\boldsymbol{\eta_{SHG}} = \frac{P_{FW}}{P_{MS}} \qquad (4.2.)$$

For a metasurface with a 12% nanocube density, we measured SHG efficiency to be $\boldsymbol{\eta_{SHG}} = 5.39 \pm 0.37 \times 10^{-11}$. We then compared this efficiency with the efficiency of a metasurface fabricated with a higher (20%) nanocube density and all other parameters the same, shown in Figure 4.3. SEM images showing the two metasurfaces with 12% and 20% nanocube surface coverage are shown in Figure 4.3.,a-b. The specular reflectance of the metasurfaces are shown in Figure 4.3.c. The broad dip in reflectance in the near-IR corresponds to the large absorbance at the fundamental mode of the metasurface gap-resonance. The similarity of the spectral position of this mode indicates that there is minimal interaction between nanocubes in-plane. Both metasurfaces operate within the weak-coupling limit for plasmonic interactions between nanocubes. This is further confirmed by the overall similarity in the line shape of the fundamental mode for each metasurface, the only difference being the marked decrease in reflectance for the higher nanocube density sample (Figure 4.3.c). The presence of in-plane observed for isolated particles.[18] The presence of in-plane coupling between nanocubes would result in a clear redshift and

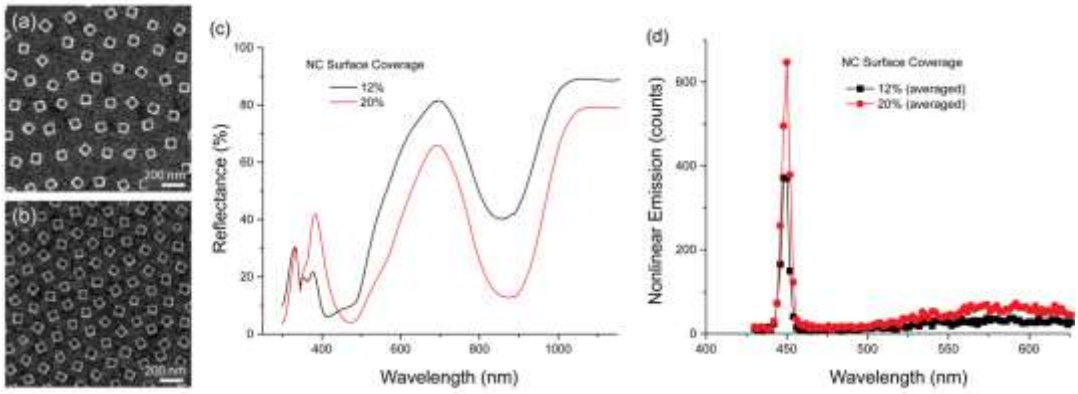

Figure 4.3. Effect of nanocube surface coverage on metasurface SHG Efficiency (a,b) SEM images of metasurface samples made with 20% and 12% Surface density of Ag nanocubes. (c) Reflectance spectra of Ag nanocube metasurfaces. (d) Nonlinear emission spectra showing SHG at λ_{SH}=450 nm.

broadening of this resonance in the spectra.[19] We measured SHG efficiency of the 20% nanocube density metasurface to be 9.05×10^{-11}, an increase of approximately 70% compared to the 12% nanocube density metasurface. Because the SHG efficiency is calculated without respect to the number of nanocube-film junctions, efficiency is directly related to absorptivity of the metasurface. This is reasonably expected because the increased per-cent surface density directly increases the total mode area of the collective gap-modes, as observed with the linear change in reflectance, a first order optical process. Unlike the expected outcome if a change in plasmonic interaction were to occur—affecting local field enhancement and thus intensity of the confined optical field, resulting in a nonlinear effect on SHG efficiency.

4.2.3. Metasurface Gap-Mode Enhancement

We use full–wave electrodynamic simulations to investigate how localized plasmon resonances excited by the metasurface influence second harmonic generation. We modeled the frequency-dependent light-matter interactions within the metasurface

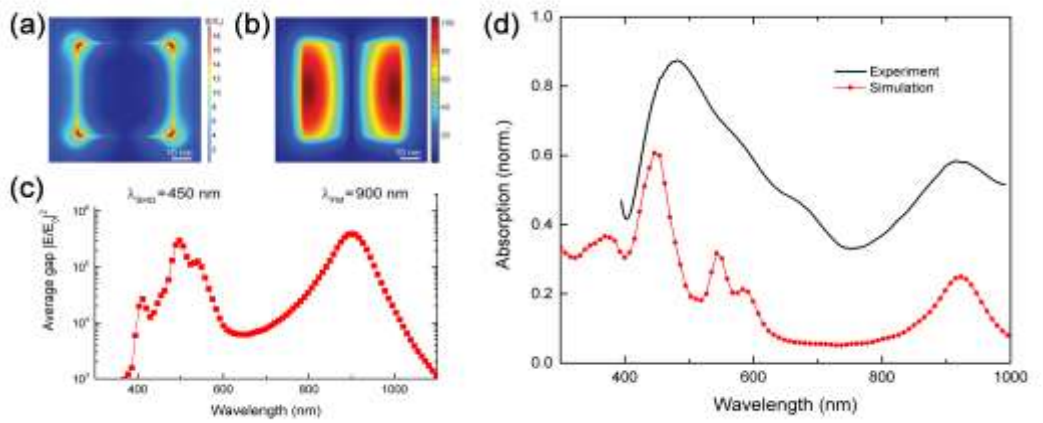

Figure 4.4. Metasurface Near-Field Enhancement, Gap-Mode Resonance Electric field distribution within the Ag-Au cavity at the second harmonic (a) and Fundamental (b) wavelengths. (c) Simulated average electric field intensity in the cavity as a function of incident wavelength. (d) Experimental and simulated metasurface absorption spectra.

structure using commercially available finite-difference time-domain (FDTD) software. Figure 4.4.,a-b shows the electric field distribution for a cross-section of the gap parallel to the surface, located halfway between the Au surface and the bottom face of the Ag nanocube. The electric field distribution at the fundamental frequency (λ_{FW}=900 nm) and the second harmonic frequency (λ_{SH}=450 nm) are shown. The experimental and simulated metasurface absorbance is plotted in Figure 4.4.d. Experimental metasurface reflectance and transmission were measured using a PE Lambda1050 UV-Vis-NIR Spectrophotometer with white-light illumination and Si photodetector; absorbance was then calculated using the relation A=(100-%R-%T)/100. The broad peak in the experimental spectrum (black curve, λ_0=900 nm) corresponds to the enhanced absorption from the fundamental gap-mode supported in the nanocube-film cavity. Experimentally, deviation in the size dispersity of the Ag nanocubes further broadens this leaky capacitive resonance. This is observed when

compared to the width of the fundamental mode of the simulated metasurface—with ideal nanocube and cavity geometry (red curve with circles); $FWHM_{SIM}(\lambda_0)$ = 200 nm, and $FWHM_{EXP}(\lambda_0)$ = 300 nm. Owing to the nature of the strong, capacitive-like coupling, and local field strength surpassing 10^2 times the incident field within the nanocube-film gap; cavity dimensions, as dictated by Ag nanocube size, is a primary contributor defining the line shape of the measured ensemble fundamental mode. This is particularly evident in the more pronounced, spectrally narrow higher order resonances in the simulated absorbance, as compared to experimental, owing to the idealized geometry of the metasurface simulations.

Although the simulated far-field absorption helps elucidate the location and nature of the various resonances present in the metasurface spectra, to gain further insight into how these modes affect the enhancement of the nonlinear optical response/processes, we must assume a more localized view. We used our metasurface simulations to calculate the wavelength-dependent average electric field enhancement, $|E/E_0|^2$ for the cross-section at the mid-point inside the nanocube-Au film cavity (Figure 4.4.c). The E-field enhancement spectrum shows the spectral dependence and magnitude of the enhanced localized E-field—one of the primary driving mechanisms for enhancing the efficiency of the nonlinear optical response at the metal/dielectric interface, and of the dielectric layer[12]. Whereas experimental metasurface design parameters (namely nanocube size, gap height) provide excellent control over spectral tunability of the fundamental gap-mode; independently tuning the wavelength of the higher order or nanocube modes is a much more constrained endeavor. While the

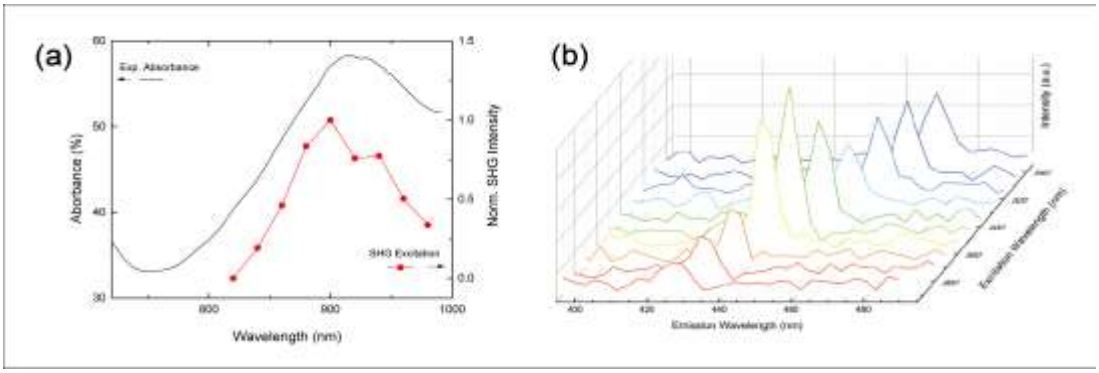

Figure 4.5. Wavelength-Dependent SHG Intensity. (a) Experimental metasurface absorbance (black) and plotted trend of the experimental extinction spectra (red circles). (b) Experimental metasurface SHG emission spectra for varying incident wavelength; the trend of which displays the extinction spectra.

metasurface is designed to exhibit maximum field enhancement—corresponding to the fundamental gap-resonance—at the excitation wavelength of $\lambda_{FW} = 900$ nm, this leaves the second harmonic wavelength shifted slightly off-resonance from any local EF maxima. However, the simulated E-field enhancement plot in Figure 4c enables a quantitative comparison between the enhancement of the cavity E-field at the second harmonic—EF_{SH} ~3.1×10^4—versus EF_{FW} ~3.9×10^5 at fundamental wavelength. Although shifted ~30 nm off peak-resonance, the modest enhancement at the second harmonic wavelength is expected to enhance nonlinear interaction with the generated second harmonic light.

4.3. Experimental and Computational Methods

Ag nanocube preparation: Ag Nanocubes were synthesized via a polyol method published elsewhere.[16] In brief, $AgNO_3$ is reduced in a solution of pentanediol, $CuCl_2$, and polyvinylpyrrolidone (PVP) (M_w=55,000). PVP serves as a selective capping agent that controls nanocube nucleation and growth. The reaction was

allowed to proceed until the resulting colloidal dispersion turned an opaque yellow-green color. To remove excess reactants, the nanocube dispersion product was centrifuged (2700 rpm for 10 min) using a Thermo Scientific CL2 Centrifuge, and the resulting precipitate was redispersed and diluted in an ethanol and water mixture, and then vacuum-filtered (Millipore Durapore membranes, with 0.65 μm, 0.45 μm, then 0.22 μm pore sizes) to remove any larger, unwanted particles.

Substrates were prepared by the following procedure: Si was sonicated in EtOH and cleaned for 60s under a 100W RF Ar plasma in a high vacuum sputter chamber (Denton Discovery 18 Sputter System). 5-10 nm of Ti followed by 50 nm of Au was then sputtered. Electromagnetic modeling was performed with Lumerical FDTD Solutions. AgNCs (Palik dielectric data) were modeled in 3 dimensions with an underlying 50 nm Au thin-film. A 3 nm dielectric layer with n = 1.4 was added to reflect the analyte layer positioned within the plasmon volume. Incident light was injected normal to the substrate, and polarized parallel to the (100) faces of the AgNC. A 1 nm global mesh was used; to improve accuracy, the mesh size was reduced in the gap region to 0.5 nm. The electric field profiles were calculated in the plane of the Au thin film, 1 nm offset from the surface. An average EF for the mSERS substrate is calculated by summing $|E/E_o|^4$ at each pixel (1x1 nm) and normalizing to the cross-sectional area of each nanocube. This calculation was carried out at discrete wavelengths over the visible range.

4.4. Conclusions

In this paper, we fabricate colloidal nanocube metasurfaces and experimentally demonstrate their ability as a highly tunable platform for enhanced non-linear light generation at visible frequencies. Our aim was to utilize the high quality field confinement and electromagnetic field enhancement achievable with colloidal nanocrystal metasurfaces to investigate the nonlinear emission of film-coupled Ag nanocube arrays.

Chapter 4, in full, is currently being prepared for submission for publication of the material. **Rozin, M. J.**; Zeng, Y.; Brown, E. R; Qian, H.; Liu, Z.; and Tao, A. R., Enhanced Second Harmonic Generation in Colloidal Metasurfaces. The dissertation author was the principal researcher and author of this material.

4.5. References

1. Kauranen, M.; Zayats, A. V., Nonlinear plasmonics. *Nat Photon* **2012,** *6* (11), 737-748.

2. Butet, J.; Brevet, P.-F.; Martin, O. J. F., Optical Second Harmonic Generation in Plasmonic Nanostructures: From Fundamental Principles to Advanced Applications. *ACS Nano* **2015,** *9* (11), 10545-10562.

3. Engheta, N., Circuits with Light at Nanoscales: Optical Nanocircuits Inspired by Metamaterials. *Science* **2007,** *317* (5845), 1698.

4. Wang, H.; Huff, T. B.; Zweifel, D. A.; He, W.; Low, P. S.; Wei, A.; Cheng, J.-X., In vitro and in vivo two-photon luminescence imaging of single gold nanorods. *Proceedings of the National Academy of Sciences of the United States of America* **2005,** *102* (44), 15752-15756.

5. Franken, P. A.; Hill, A. E.; Peters, C. W.; Weinreich, G., Generation of Optical Harmonics. *Physical Review Letters* **1961,** *7* (4), 118-119.

6. Maiman, T. H., Stimulated Optical Radiation in Ruby. *Nature* **1960,** *187* (4736), 493-494.

7. Contents A2 - Boyd, Robert W. In *Nonlinear Optics (Third Edition)*, Academic Press: Burlington, 2008; pp vii-xi.

8. Yang, Y.; Wang, W.; Boulesbaa, A.; Kravchenko, I. I.; Briggs, D. P.; Puretzky, A.; Geohegan, D.; Valentine, J., Nonlinear Fano-Resonant Dielectric Metasurfaces. *Nano Letters* **2015,** *15* (11), 7388-7393.

9. Park, S.; Hahn, J. W.; Lee, J. Y., Doubly resonant metallic nanostructure for high conversion efficiency of second harmonic generation. *Optics Express* **2012,** *20* (5), 4856-4870.

10. Celebrano, M.; Wu, X.; Baselli, M.; Großmann, S.; Biagioni, P.; Locatelli, A.; De Angelis, C.; Cerullo, G.; Osellame, R.; Hecht, B.; Duò, L.; Ciccacci, F.; Finazzi, M., Mode matching in multiresonant plasmonic nanoantennas for enhanced second harmonic generation. *Nat Nano* **2015,** *10* (5), 412-417.

11. Butet, J.; Yang, K.-Y.; Dutta-Gupta, S.; Martin, O. J. F., Maximizing Nonlinear Optical Conversion in Plasmonic Nanoparticles through Ideal Absorption of Light. *ACS Photonics* **2016,** *3* (8), 1453-1460.

12. Linnenbank, H.; Grynko, Y.; Forstner, J.; Linden, S., Second harmonic generation spectroscopy on hybrid plasmonic/dielectric nanoantennas. *Light Sci Appl* **2016,** *5*, e16013.

13. Lassiter, J. B.; Chen, X.; Liu, X.; Ciracì, C.; Hoang, T. B.; Larouche, S.; Oh, S.-H.; Mikkelsen, M. H.; Smith, D. R., Third-Harmonic Generation Enhancement by Film-Coupled Plasmonic Stripe Resonators. *ACS Photonics* **2014,** *1* (11), 1212-1217.

14. Kruk, S.; Weismann, M.; Bykov, A. Y.; Mamonov, E. A.; Kolmychek, I. A.; Murzina, T.; Panoiu, N. C.; Neshev, D. N.; Kivshar, Y. S., Enhanced Magnetic

Second-Harmonic Generation from Resonant Metasurfaces. *ACS Photonics* **2015,** *2* (8), 1007-1012.

15. Moreau, A.; Ciraci, C.; Mock, J. J.; Hill, R. T.; Wang, Q.; Wiley, B. J.; Chilkoti, A.; Smith, D. R., Controlled-reflectance surfaces with film-coupled colloidal nanoantennas. *Nature* **2012,** *492* (7427), 86-89.

16. Sun, Y.; Xia, Y., Shape-Controlled Synthesis of Gold and Silver Nanoparticles. *Science* **2002,** *298* (5601), 2176-2179.

17. Demichel, O.; Petit, M.; Viarbitskaya, S.; Méjard, R.; de Fornel, F.; Hertz, E.; Billard, F.; Bouhelier, A.; Cluzel, B., Dynamics, Efficiency, and Energy Distribution of Nonlinear Plasmon-Assisted Generation of Hot Carriers. *ACS Photonics* **2016,** *3* (5), 791-795.

18. Dahmen, C.; Schmidt, B.; von Plessen, G., Radiation Damping in Metal Nanoparticle Pairs. *Nano Letters* **2007,** *7* (2), 318-322.

19. Rozin, M. J.; Rosen, D. A.; Dill, T. J.; Tao, A. R., Colloidal metasurfaces displaying near-ideal and tunable light absorbance in the infrared. *Nat Commun* **2015,** *6*.

Chapter 5

Meta-Surfaced Enhanced Raman Scattering for Hyperspectral Chemical Mapping

5.1. Introduction

Raman spectroscopy is a highly advantageous technique for chemical and biological identification because it provides chemical-specific vibrational signatures of analytes, performs over a large wavelength range, can be implemented using portable spectroscopic instrumentation, and is well suited to detection in aqueous environments.[1-3] These features enable high analyte specificity along with real-time measurement capabilities. However, typical values for Raman scattering cross-sections are low compared to other optical processes, ranging between 10^{-31} – 10^{-29} cm^2 per molecule. Surface-enhanced Raman spectroscopy (SERS) overcomes these low scattering cross-sections by placing the analyte within the evanescent field generated at a metal surface, resulting in the near-field amplification of scattered light.[5] Colloidal metal nanoparticles composed of Ag, Au, and other highly conducting metals are highly studied substrates for SERS[6-10] because they support localized surface plasmon resonances (LSPRs) that produce intense electromagnetic fields localized at the nanoparticle surface and within nanoparticle junctions.[11-15] In addition, colloidal nanoparticles are readily synthesized using wet chemistry, and are thus amenable to solution post-processing and chemical surface modification to generate SERS substrates for chemical detection. As examples, colloidal metal nanoparticles have been used as SERS substrates for trace detection of molecules such as narcotics[16] and pesticides,[17] and to characterize the chemical reactions of surfaces[18] and catalysts.[13]

A critical challenge in SERS sensing is the ability to predict the optical behavior — and thus, the chemical sensitivity — of these nanoparticle-based substrates. There has been a considerable amount work trying to predict Raman EFs. Experimentally determined hotspot distributions on SERS substrates have been reported.[14] Experiment and simulation have been paired to explain the EF resulting from shaped nanoparticles, dimers, and clusters.[6, 19, 20] More recently, studies have used simulations and electron tomography to analyze near-atomic scale features, and their effects on optical properties.[21-23] While these studies are carefully conducted, they are limited to single particles or clusters and not representative of the polydispersity resulting from an ensemble colloidal solution. Most colloidal nanoparticles are synthesized in batch quantities and possess a large degree of heterogeneity in comparison to lithographically generated metal nanostructures. A typical size dispersion curve for colloidal nanoparticles is Gaussian,[24, 25] where larger nanoparticles exhibit red-shifted dipolar LSPR resonances and smaller nanoparticles exhibit blue-shifted LSPR resonances from the average peak position in the optical scattering spectrum. Complex shapes and assemblies can also introduce higher-order LSPR modes as well as dark plasmon modes, where near-field enhancement is high while far-field scattering is suppressed.[6, 26-28] As heterogeneity increases, the optical scattering response corresponding to LSPR excitation broadens, while the near-field enhancements of non-ideally sized nanoparticles are shifted off-resonance. Because SERS sensing typically relies on ensemble measurements where the optical readout is collected from many nanoparticles[29] experimental SERS sensitivities can vary

dramatically from predictions that are based on the optical behavior of singular nanoparticle size, shape, or assemblies where sample dispersity is not taken into account.[19, 30]

Here we construct an analytical model for the effects of nanoparticle size dispersity in the SERS response of colloidal Ag nanocubes arranged on flat Au films. We and others have recently demonstrated that these colloidal structures behave as large-scale plasmonic surfaces that exhibit high electromagnetic field enhancements.[31, 32] This is due to the highly confined optical gap generated between the colloidal nanocube and the metal film when they are separated by distances of < 20 nm. These colloidal surfaces have already been demonstrated as substrates for perfect optical absorption[33] and fast fluorescence emission.[34] In addition, Ag nanocubes present an ideal model system to understand the effects of colloidal dispersity on SERS response because they are single crystalline and nearly atomically planar, which means that they can be accurately modeled using electrodynamic simulations to account for different nanoparticle sizes and shapes (i.e. using simple parameters such as nanocube edge length and radius of curvature of cube corners). Here, we investigate the effects of colloidal dispersity by measuring the SERS enhancement factor (EF) for Ag nanocube substrates and comparing these results with our electrodynamic simulations. We measure the size and shape dispersity of typical Ag nanocube samples to simulate the optical response of an ensemble of nanoparticles, rather than a single nanoparticle. Our analysis shows that by taking into account a range of nanocube sizes and shapes,

we can predict the broad optical resonances and EFs observed in our experimental colloidal SERS substrates.

5.2. Results and Discussion

5.2.1. mSERS Fabrication and Characterization

In order to determine colloidal Ag nanocube size distributions, we analyzed multiple SEM images (Figure 5.1.) for SERS substrates fabricated with five different average nanocube sizes. We measured nanoparticle size and radius of curvature (ROC). Using standard image analysis software (ImageJ), we measured edge lengths of at least 100 nanocubes per substrate. Their distributions are displayed as histograms in Figure 2 for five different nanocube samples. The distributions were fit to a Gaussian curve to calculate average edge lengths and standard deviations. The same image analysis software was used to determine the ROC for the corners of the nanocubes. The ROC however is more difficult to accurately measure due to resolution limits of SEM imaging. The average sizes, standard deviations, and ROC for the SERS substrates are listed in Table 5.1.

We performed Raman spectroscopy on these nanocube substrates in order to determine the effect of average nanocube size on the Raman enhancement factor (EF). Figure 1A shows a schematic of a nanocube SERS substrate that is functionalized with the Raman reporter, PhSH, a well-studied and characterized molecule often used to

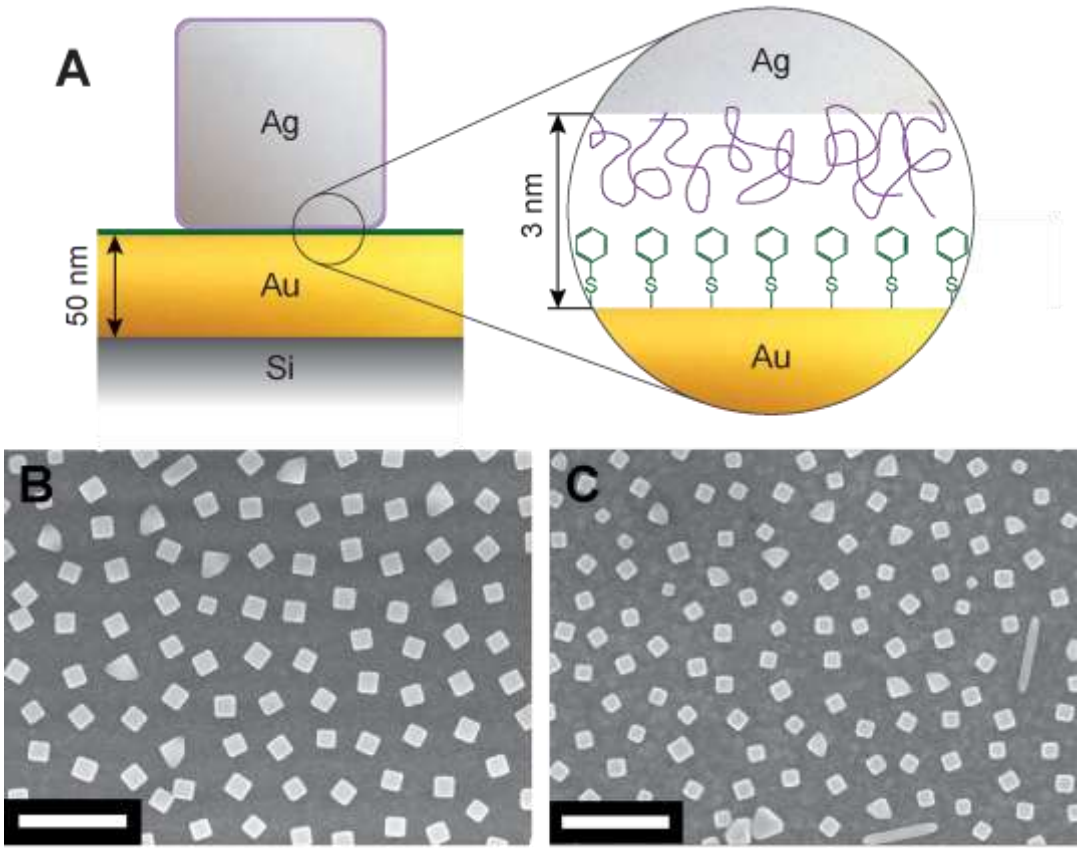

Figure 5.1. SERS Substrate schematic and representative SEM Images. A) A schematic of the nanocube on an Au-thin film as well as the PhSH and PVP layers producing a 3 nm dielectric spacer layer (inset). B,C) SEM Images of (B) 96 nm and (C) 74 nm nanocube dispersions deposited on an Au thin-film. Scale bars = 500 nm.

estimate Raman EFs.[35, 36] PhSH is also known to form well-packed molecular monolayers on Au surfaces, which enables us to obtain an accurate estimate of the number of reporter molecules located in the optical gap.[37] The remaining gap between the nanocube and film results from a thin layer of PVP on the nanocube leftover from the colloidal synthesis. The lateral spacing between individual nanocubes on the substrate is sufficient to ensure no inter-nanoparticle coupling occurs.[33]

Figure 5.3. shows the average PhSH SERS spectra collected for each of the five SERS substrates. Table 5.2. shows the SERS intensities at the 1024 cm^{-1}

vibrational mode for each substrate. All intensities fall in the range of 1.07 – 2.3 x 10^5

Table 5.1. Nanocube sample size distributions.

Mean Nanocube Size (nm)	Standard Deviation (nm)	Radius of Curvature (nm)
70	4	17
74	4	16
91	6	12
96	6	11
105	5	11

counts. Using these intensities, we calculated the Raman EF to approximate how much the Raman scattering intensity is increased per molecule for a given SERS substrate using the following equation:[27]

$$EF = \left(\frac{I_{SERS}}{I_{Raman}}\right)\left(\frac{N_{Raman}}{N_{SERS}}\right) \quad (5.1)$$

Where I_{SERS} and I_{Raman} are the Raman intensities for the SERS substrates and bulk PhSH samples respectively. N_{SERS} and N_{Raman} are the number of Raman molecules from which the intensities originate and are calculated using the PhSH bulk density and literature packing values for a molecular monolayer of PhSH on an Au surface.[38] Laser spot sizes were determined by scanning over a cleaved Si edge. N_{SERS} is then normalized to the density of nanocubes on each SERS substrate. All EFs were calculated at the 1024 cm^{-1} vibrational mode, which corresponds to the ring breathing mode and does not depend on molecular orientation.[5] Error in EF was determined from the standard deviation in the measured I_{SERS} values; error for I_{Raman} was considered negligible.

5.2.2. The effects of AgNC Surface Density on EF

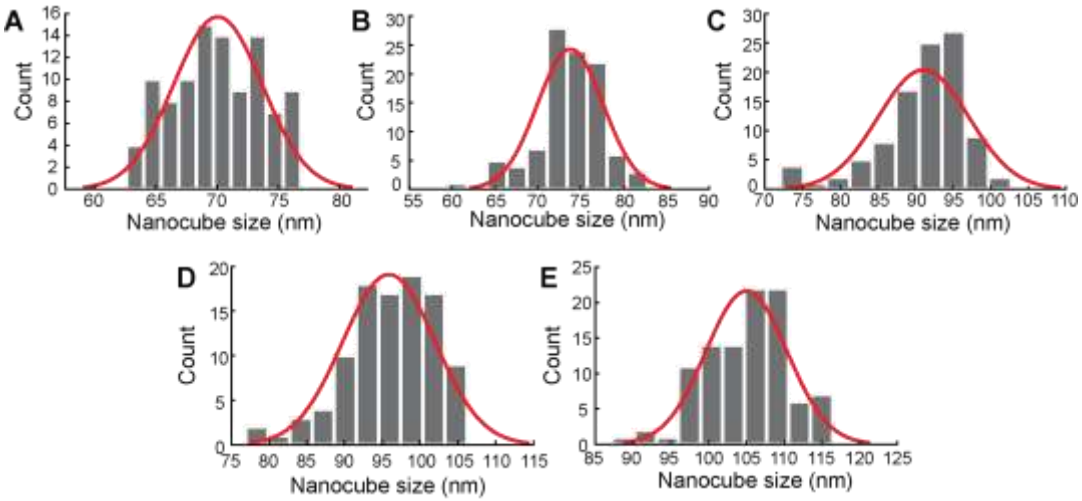

Figure 5.2. Histogram of size distributions for five different SERS substrates fabricated with varying nanocube sizes: A) 70 nm, B) 74 nm, C) 91 nm, D) 96 nm, E) 105 nm.

As previously reported, our simulation results show the appearance of a resonant optical cavity that is confined to the gap between the Ag nanocube and Au film.[32] Figure 4B-F show the electrical field distributions for Ag nanocubes with edge lengths of 70, 74, 91, 96, and 105 nm, respectively. The color maps are obtained by simulating the electrical field enhancement, $|E/E_o|$ at an excitation wavelength of 783 nm, the data point nearest the 785 nm Raman laser line. The field distributions in Figure 5.4. are characterized by a symmetric mode where reflections of the cavity resonance occur at the edges of the nanocube. The symmetry of these plasmon modes arises from the waveguide-like nature of the cavity modes supported in metal-insulator-metal cavities.[31] The electric field profiles shown in Figure 5.4.,b-f

correspond to the lowest order dipolar mode, or the fundamental waveguide mode. This resonance is intimately linked to both nanocube size and gap height.[33]

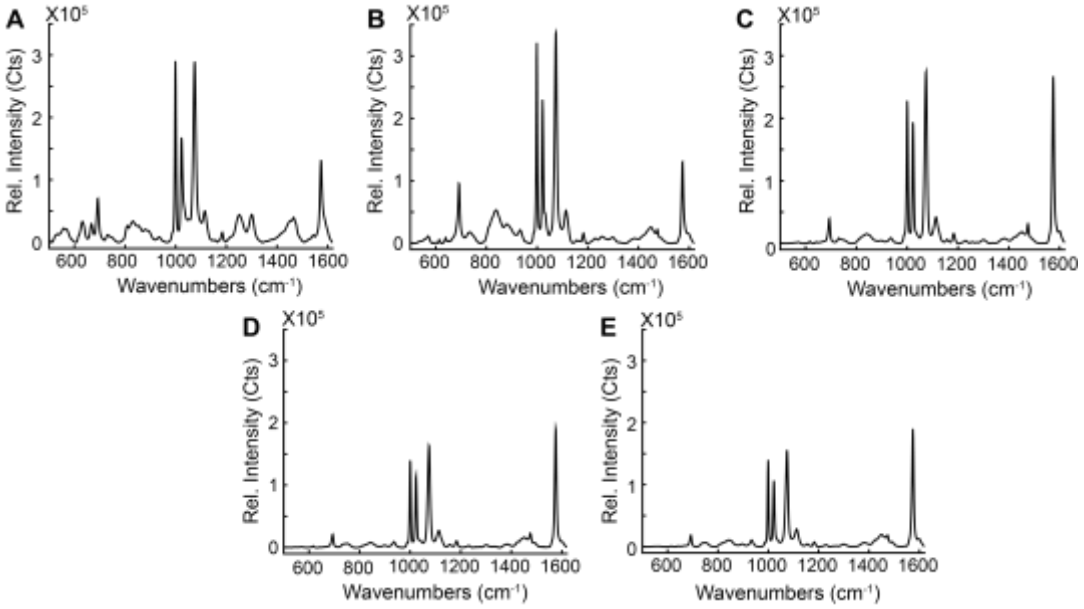

Figure 5.3. Average SERS spectra from five different SERS substrates fabricated from different sized nanoparticles (intensity displayed in counts): A) 70 nm, B) 74 nm, C) 91 nm, D) 96 nm, E) 105 nm. Each spectra is an average of 100 individual spectra collected from random points on the substrate.

Figure 5.4.g plots the Raman EF versus wavelength for each of the Ag nanocube substrates. An average Raman EF for each nanocube size is calculated by summing $|E/E_o|^4$ at each pixel (1x1 nm) and normalizing to the cross-sectional area of each nanocube. This calculation was carried out at discrete wavelengths over the range of 300-1300 nm. The maximum EFs correspond to excitation at the fundamental resonance. The position of the maximum EF shifts by approximately 10 nm per nanometer increase in edge length. At 785 nm, we observe a maximum $|E/E_o| = 97.1$ for a 74 nm Ag nanocube, whereas a cube only 4 nm smaller in edge length has a maximum field enhancement of $|E/E_o| = 36.9$, confirming a strong dependence on size.

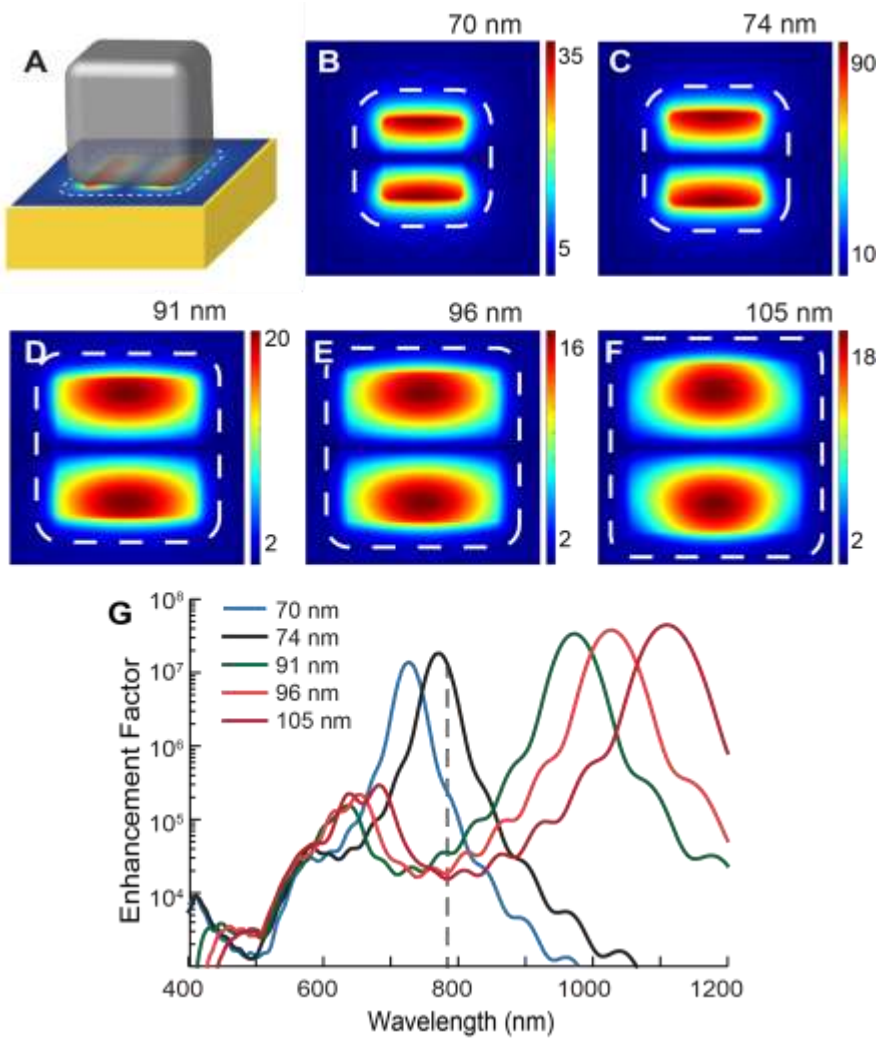

Figure 5.4. Computed field enhancement profiles and single nanocube Raman enhancement factors. A) A cartoon of a silver nanocube flat on an Au-thin film, and the field intensity profile solved at 783 nm for each of five different nanocube sizes B) 70 nm, C) 74 nm, D) 91 nm, E) 96 nm, and F) 105 nm. Dashed white lines represent the footprint of the cube. G) Raman enhancement factors for 70, 74, 91, 96, and 105 nm silver nanocube SERS substrates. The ringing artifacts in the EF profiles are likely caused by reflections in the PML. It is also possible they are caused by the finite time window used in an FDTD simulation which produces the ringing when Fourier transformed to the frequency domain.[4]

Table 5.2. shows the calculated Raman EFs resulting from single nanocube models. For excitation at 785 nm, a 74 nm nanocube possesses a Raman EF = 1.24 x 10^7 which is 54 times larger than that of a 70 nm nanocube that possesses EF = 2.29 x 10^5. Ag nanocubes with edge lengths of 91, 96, and 105 nm all possess Raman EFs near 10^4,

almost 3 orders of magnitude less than the smaller cubes. Other studies have shown similar results indicating strong size dependence for differently shaped colloidal metal nanoparticles.[31, 39, 40] In general, colloidal size-tuning where the nanoparticle LSPR is frequency-matched to the Raman excitation source is a widely accepted mechanism to engineer colloidal metal nanoparticles with maximum Raman EFs.

Ensemble Nanocube Models: To accurately predict the effect of size dispersity on Raman EF, we used our single-nanoparticle FDTD simulation results to model the optical response of an ensemble of Ag nanocubes that possess a range of edge lengths. Each ensemble EF was calculated by using a weighted average of the EFs for five differently sized nanocubes. The five sizes for each ensemble EF were determined from the experimentally determined size distributions shown in Figure 5.2. We chose to include the optical response for Ag nanocubes with edge lengths corresponding to the mean size, the mean size ± one standard deviation, and the mean size ± two standard deviations. The ensemble EF curve was generated by weighting each of these components to its population count on the Gaussian fits shown in Figure 5.2, roughly approximating the real size distribution of the colloidal sample.

The ensemble EFs calculated for 70, 74, 91, 96, and 105 nm nanocube samples are plotted in Figure 5.5. (gray shaded region) along with the simulation results for each single-nanoparticle component that contributes to the weighted average (colored lines). The Raman EF curves for the 70 and 74 nm nanocube ensembles differ significantly from the EF curves for the single nanocubes, specifically with respect to peak broadening of the LSPR band. The 91, 96, and 105 nm nanocube ensembles

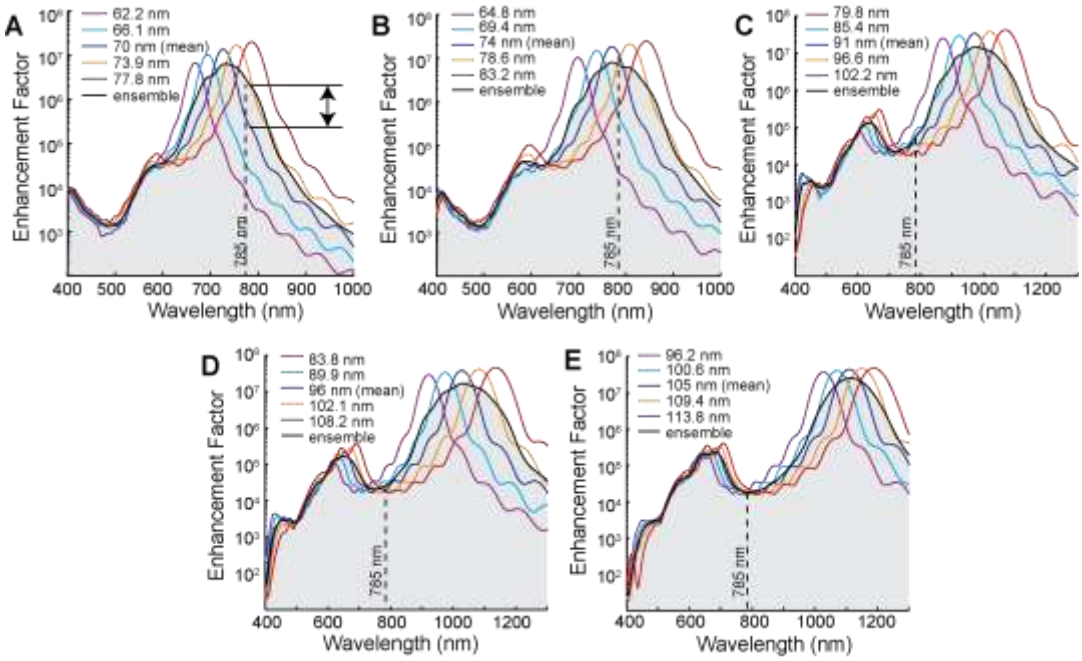

Figure 5.5. Calculation of ensemble EFs for different NP size distributions A) 70 nm, B) 74 nm, C) 91 nm, D) 96 nm, and E) 105 nm. Each ensemble EF is calculated by simulating five different nanocube sizes and generating a weighted average. Nanocube edge lengths were chosen to be representative of a Gaussian distribution of nanocube sizes, as determined by SEM image analysis. Nanocube models were constructed for edge lengths corresponding to the average nanocube size and ± one or two standard deviations.

exhibit resonances far enough from 785 nm that the EFs calculated for a size-disperse ensemble sample is not significantly different from the initial single nanocube models. Figure 5.6. shows a plot of our simulated and experimental Raman EFs as a function of average nanocube size. Our single nanocube models predict the highest Raman EF of 1.24×10^7 for a nanocube with an edge length of 74 nm, whereas the Raman EF drops by almost three orders of magnitude for nanocubes over 90 nm. Our experiments, however, show that this decrease is only by a factor of two. Our ensemble nanocube models predict a large peak broadening in the overall LSPR resonance of each SERS substrate, which may account for this discrepancy. Accounting for the peak broadening that accompanies a disperse colloidal sample

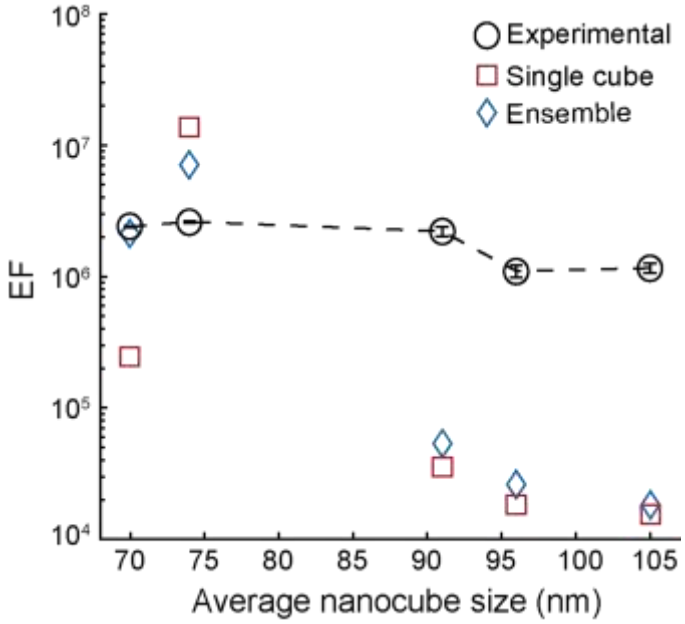

Figure 5.6. EF values versus nanoparticle size distribution. Black circles represent experimental EF determined at the 1024 cm^{-1} peak and their errors. Red squares indicate single nanoparticle EFs as determined by computer simulation. The blue diamonds indicate ensemble EFs determined by modeling nanoparticle size distribution.

allows us to more accurately predict the optical response for small nanocubes whose resonances lie near the excitation wavelength. However, our analytical model does not account for the large Raman EFs observed for substrates composed of large nanocubes (> 90 nm), which we observe to give large EFs even though their LSPRs are off-resonance.

This discrepancy for SERS substrates composed of larger Ag nanocubes is likely due to the contributions from shape heterogeneity, which can have large effects on the resonance and which are not accounted for in our analytical model. Figure 5.1.a shows that our colloidal substrates are composed of many “defect” nanoparticles that possess other polyhedral shapes (e.g. rods and tetrahedra), rounded corners, or form small nanoparticle clusters. Figure 5.7.a shows the field distribution profiles for a 100

nm nanocube and a 100 nm tetrahedron, a common shape defect observed in our colloidal SERS substrates. At an excitation wavelength of 785 nm, the maximum field

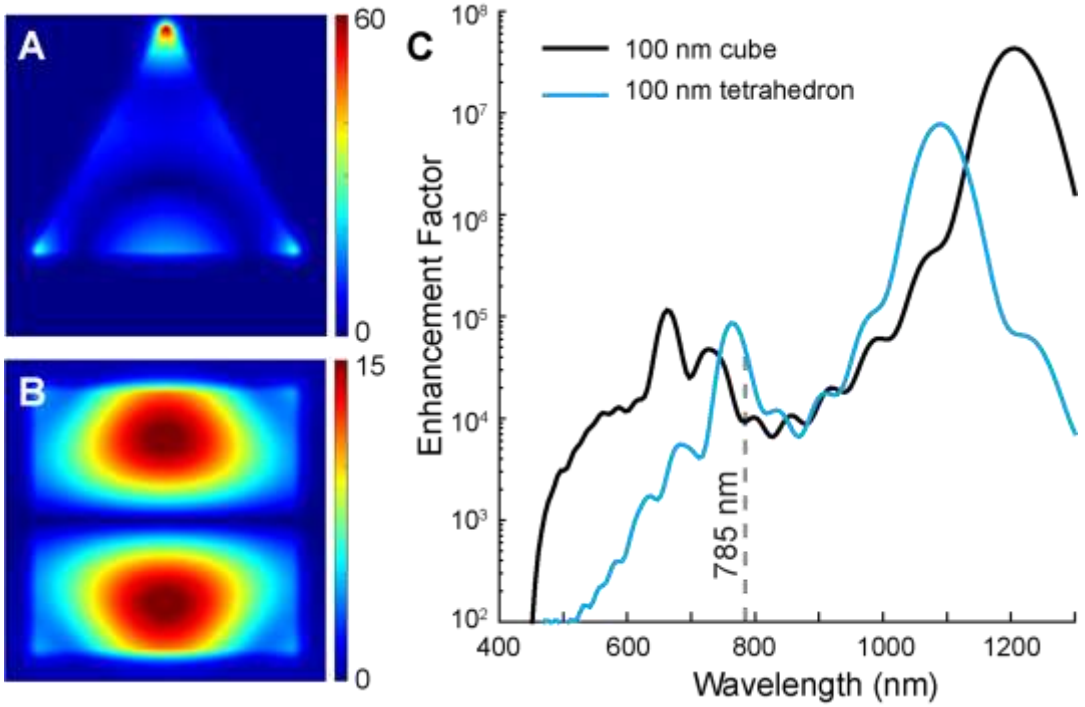

Figure 5.7. Effect of shape heterogeneity on enhancement factor. A) Calculated field enhancement profile of an Ag tetrahedron with edge length = 100 nm, and B) field enhancement profile of an Ag nanocube with edge length = 100 nm (783 nm excitation). C) Wavelength-dependent EF for the tetrahedral nanoparticle and nanocube modeled in parts A and B.

intensity is $|E/E_0|$ = 55.2 for the tetrahedron and $|E/E_0|$ = 15.4 for the nanocube. While the field intensity is higher for the tetrahedron, the optical mode of the cube extends over a larger surface area. As a result, the two polyhedral shapes possess near identical Raman EFs at this excitation wavelength (Figure 5.7.c).

We also considered the effect the orientation of silver nanocubes may have on the Raman EF. Nanoparticle orientation relative to incident light is known to significantly affect the plasmon resonance in many systems[28, 41]. We simulated a 70 nm nanocube with a 17 nm radius of curvature oriented with sides parallel to and at

18, 27, and 45° relative to the incident polarization. Figure 5.8.A-D) shows the field enhancement profiles. The mode shape changes to fill the volume of the cavity in the

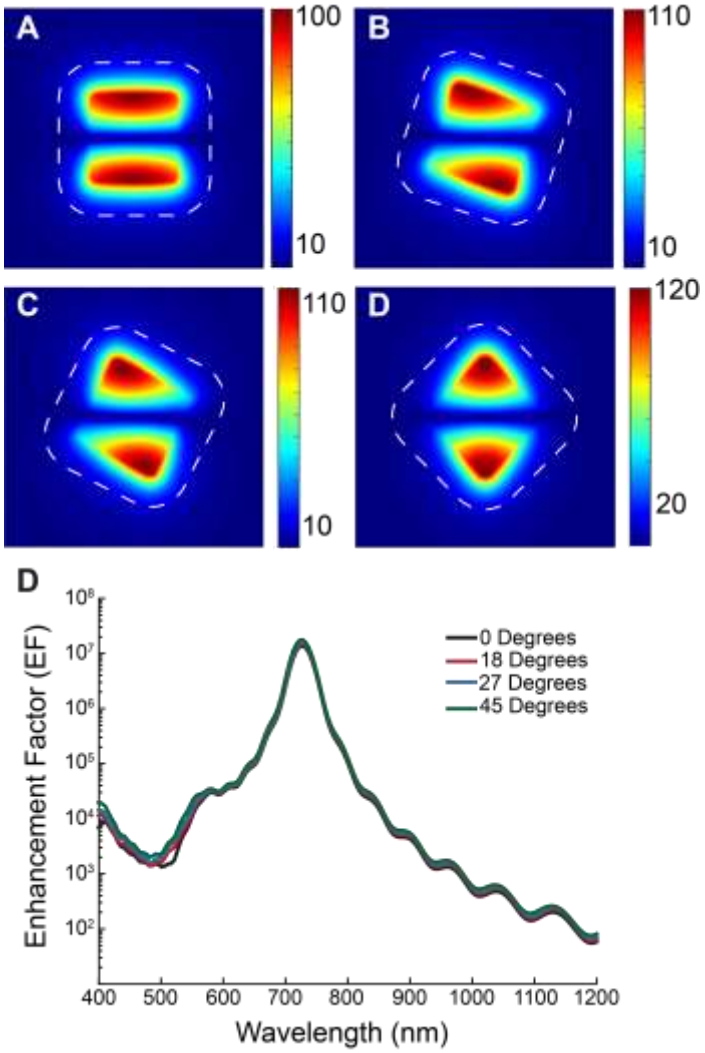

Figure 5.8. Orientational dependence of silver nanocubes. A-D) Field Intensity profiles solved at the resonance (728 nm) for a 70 nm nanocube with a 17 nm radius of curvature at different angular orientations relative to the incident polarization: A) 0 degrees B) 18 degrees C) 27 degrees and D) 45 degrees. E) Raman enhancement factors for different orientations of silver nanocube SERS substrates from 0 to 45 degrees.

direction of the polarization, evolving from rectangles to triangles as the nanocube approaches a 45° orientation. The mode volume doesn't change however, and we found that the resonance location didn't change either. The enhancement factor at 728

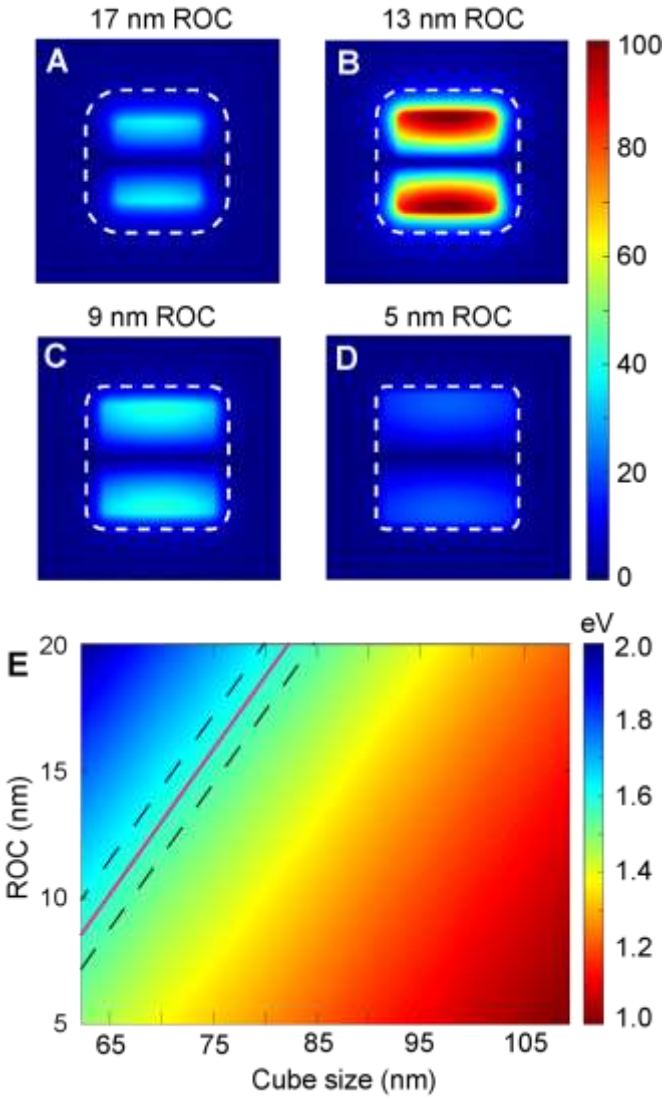

Figure 5.9. FDTD simulations and interpolated data for nanocube resonance when considering both nanocube size and ROC. A-D) Field enhancement profiles at 783 nm for a 70 nm nanocube modeled with A) 17 nm B) 13 nm C) 9 nm and D) 5 nm ROCs. E) Two dimensional heat map of resonance peak position, between the dashed lines is the range of nanocubes which are resonant with a 785 nm excitation source.

nm (at resonance) increases from 1.38 x 10^7 at 0° to 1.76 x 10^7 at 45°. This small change is not considered significant for the experimental discrepancy we observe. To be sure these orientational results were generalizable, we also modeled an 80 nm

nanocube with a 5 nm radius of curvature and found a similarly low enhancement factor dependence on polarization.

Table 5.2. Experimental and simulated Raman intensities and enhancement factors for each SERS substrate. All values are calculated at 785 nm.

	70 nm	**74 nm**	**91 nm**	**96 nm**	**105 nm**
I_{SERS} (1024 cm^{-1}) (X 10^5 Counts)	1.68 ± 0.41	2.30 ± 0.25	1.94 ± 0.16	1.14 ± 0.12	1.07 ± 0.09
Experimental EF (X 10^6)	2.47 ± 0.61	2.61 ± 0.28	2.21 ± 0.18	1.10 ± 0.11	1.16 ± 0.10
Single nanocube EF	2.29 x 10^5	1.24 x 10^7	3.51 x 10^4	1.86 x 10^4	1.56 x 10^4
Ensemble nanocube EF	1.97 x 10^6	6.89 x 10^6	5.69 x 10^4	2.63 x 10^4	1.82 x 10^4

Figure 5.9. shows the effects of curvature at colloidal nanocube corners on Raman EF. We simulated the field distributions for 70 nm Ag nanocubes modeled with ROCs of 5, 9, 13, and 17 nm. At an excitation wavelength of 785 nm, decreasing the ROC from 17 to 13 nm increases the maximum field intensity from $|E/E_0|$ = 36.9 to $|E/E_0|$ = 101.9 (Figure 5.8.,A-D). This results in a significant increase in Raman EF, from EF = 2.29 x 10^5 to EF = 1.80 x 10^7. Further decreasing the ROC leads to a decrease in field intensity and Raman EF as the fundamental LSPR mode becomes red-shifted beyond 785 nm. (Figure 5.9.C,D) To expand this analysis, we plotted the energetic location of the resonance peak as a function of both Ag nanocube size and ROC (Figure 5.9.,E). The resonance peak shifts by as much as 300 nm for a fixed nanocube size when the ROC is varied from 2-20 nm. As a visual aid, the regions bounded within the dashed lines denote the nanocube sizes and ROC combinations that are resonant at 785 nm (Figure 5.9.E, solid red line).

5.3. Experimental and Computational Methods

SERS Substrate Fabrication: Ag nanocubes were synthesized using a modified polyol reaction as previously described.[42] In brief, $AgNO_3$ is reduced in 1-5 pentanediol heated to ~200° C. $CuCl_2$ and polyvinylpyrrolidone (PVP, MW = 55,000) are added to control the nucleation and growth processes, and also to passivate the nanocube surfaces after growth. In order to decrease polydispersity and remove non-cubic particles, nanocubes were vacuum filtered. Millipore Durapore membranes were used in three different sizes to remove sequentially smaller nanoparticles: 650 nm, 450 nm, and 220 nm. The final nanocubes are then concentrated and washed via centrifugation several times to remove excess PVP, and resuspended in $CHCl_3$.

Nanocube films are made via a Langmuir Blodgett trough (KSV Nima KN2001).[43] The nanocube suspension is slowly drop-cast onto a deionized water subphase. After the nanocubes equilibrate, they are isothermally compressed at a rate of 3 cm^2/min to a desired surface pressure between 0 and 2 mN/m. The film was then transferred to a 50 nm Au thin-film sputtered on (100) Si. The Au is treated with 1 mM (ethanol) thiophenol (PhSH) overnight to form a self-assembled monolayer (SAM) on the Au surface. It is then copiously rinsed with EtOH and dried under N_2. The nanocube film is then transferred to the Au via dip coating and allowed to dry. Figure 1A shows a schematic of a single nanocube deposited on the functionalized Au. Figure 1B,C shows SEM images of two SERS substrates fabricated from different sized nanocubes, with averages of 74 and 96 nm.

Raman Data Collection: All data was collected on a Renishaw inVia Raman microscope. A 785 nm stripe diode laser was used with an illumination power of < 1 mW. A 50x, 0.9 NA objective was used for both illumination and collection of Raman data. For each SERS substrate, 100 data points were collected at random locations and averaged. For bulk PhSH Raman, 10 data points were collected and averaged under the same illumination conditions.

Electrodynamic Simulations: Electromagnetic modeling was performed with Lumerical FDTD Solutions. Ag nanocubes (Palik dielectric data) were modeled in 3 dimensions with a 50 nm Au thin film as a substrate. A 3 nm spacer with index of refraction (n) = 1.4 was added to reflect the organic spacing layers (PhSH and PVP). Incident light was injected normal to the substrate, and polarized parallel to the (100) faces. A 1 nm global mesh was used; to improve accuracy, the mesh size was reduced in the gap region to 0.5 nm. The model was solved at 200 points at 5 nm intervals from 300 nm to 1300 nm. All $|E/E_0|$ and EF values were calculated for 785 nm using a cubic spline interpolation from the surrounding data points. All electric field profiles shown are at 783 nm, the data point nearest our 785 nm Raman laser line. The electric field measurements were calculated in the plane of the Au thin film, 1 nm offset from the surface.

5.4. Conclusions

Our results show that size and shape dispersity in colloidal metal nanoparticle samples can have a significant effect on the resulting Raman EF for nanoparticle-based SERS substrates. Single nanoparticle models do not provide an accurate

prediction of Raman EFs, which can lead to inaccurate predictions of SERS detection levels. Using an analytical model that weight averages the optical response of multiple single nanoparticle models that possess different sizes can improve this accuracy. Extending these models to encompass shape dispersity requires image analysis to gauge ROC distributions and counts for other shape defect populations. Finally, accounting for other variables such as Ag surface roughness and deviations in optical gap thickness may also improve the accuracy of our ensemble model.

Chapter 5, in part, is a reformatted reprint of the material from: Dill†, T. J. & **Rozin†, M. J.**, Brown, E. R., Palani, S., Tao. A. R., Investigating the Effects of Polydispersity on Gap-Mode SERS Enhancement Factors. *The Analyst* **2016**, 141 (12), 3916-3924. (†Authors contributed equally) The dissertation author was the principal researcher and author of this paper.

5.5. References

1. Stockman, M. I., Nanoscience: Dark-hot resonances. *Nature* **2010,** *467* (7315), 541-542.

2. *Raman Spectroscopy for Nanomaterials Characterization*. 1 ed.; Springer-Verlag Berlin Heidelberg: 2012; p 646.

3. Ru, E. L.; Etchegoin, P., *Principles of Surface-Enhanced Raman Spectroscopy: and related plasmonic effects*. Elsevier Science: 2008.

4. Alaee, R.; Menzel, C.; Huebner, U.; Pshenay-Severin, E.; Bin Hasan, S.; Pertsch, T.; Rockstuhl, C.; Lederer, F., Deep-Subwavelength Plasmonic

Nanoresonators Exploiting Extreme Coupling. *Nano Letters* **2013,** *13* (8), 3482-3486.

5. Fang, Z.; Liu, Z.; Wang, Y.; Ajayan, P. M.; Nordlander, P.; Halas, N. J., Graphene-Antenna Sandwich Photodetector. *Nano Letters* **2012,** *12* (7), 3808-3813.

6. Landy, N. I.; Sajuyigbe, S.; Mock, J. J.; Smith, D. R.; Padilla, W. J., Perfect Metamaterial Absorber. *Physical Review Letters* **2008,** *100* (20), 207402.

7. Avitzour, Y.; Urzhumov, Y. A.; Shvets, G., Wide-angle infrared absorber based on a negative-index plasmonic metamaterial. *Physical Review B* **2009,** *79* (4), 045131.

8. Tao, A. R.; Yang, P., Polarized Surface-Enhanced Raman Spectroscopy on Coupled Metallic Nanowires. *The Journal of Physical Chemistry B* **2005,** *109* (33), 15687-15690.

9. Yoshida, A.; Imazu, K.; Li, X.; Okamoto, K.; Tamada, K., Spectroscopic Properties of Multilayered Gold Nanoparticle 2D Sheets. *Langmuir* **2012,** *28* (49), 17153-17158.

10. Lassiter, J. B.; McGuire, F.; Mock, J. J.; Ciracì, C.; Hill, R. T.; Wiley, B. J.; Chilkoti, A.; Smith, D. R., Plasmonic Waveguide Modes of Film-Coupled Metallic Nanocubes. *Nano Letters* **2013**.

11. Holland, W. R.; Hall, D. G., Frequency Shifts of an Electric-Dipole Resonance near a Conducting Surface. *Physical Review Letters* **1984,** *52* (12), 1041-1044.

12. Mistark, P. A.; Park, S.; Yalcin, S. E.; Lee, D. H.; Yavuzcetin, O.; Tuominen, M. T.; Russell, T. P.; Achermann, M., Block-Copolymer-Based Plasmonic Nanostructures. *Acs Nano* **2009,** *3* (12).

13. Gao, B.; Rozin, M. J.; Tao, A. R., Plasmonic nanocomposites: polymer-guided strategies for assembling metal nanoparticles. *Nanoscale* **2013,** *5* (13), 5677-5691.

14. Kildishev, A. V.; Boltasseva, A.; Shalaev, V. M., Planar Photonics with Metasurfaces. *Science* **2013,** *339* (6125).

15. Wiley, B.; Sun, Y.; Mayers, B.; Xia, Y., Shape-controlled synthesis of metal nanostructures: the case of silver. *Chemistry* **2005,** *11* (2), 454-63.

16. Fan, J. A.; Bao, K.; Wu, C.; Bao, J.; Bardhan, R.; Halas, N. J.; Manoharan, V. N.; Shvets, G.; Nordlander, P.; Capasso, F., Fano-like Interference in Self-Assembled Plasmonic Quadrumer Clusters. *Nano Letters* **2010,** *10* (11), 4680-4685.

17. Mukherjee, S.; Libisch, F.; Large, N.; Neumann, O.; Brown, L. V.; Cheng, J.; Lassiter, J. B.; Carter, E. A.; Nordlander, P.; Halas, N. J., Hot Electrons Do the Impossible: Plasmon-Induced Dissociation of H2 on Au. *Nano Letters* **2012,** *13* (1), 240-247.

18. Bozhevolnyi, S. I.; Søndergaard, T., General properties of slow-plasmon resonant nanostructures: nano-antennas and resonators. *Opt. Express* **2007,** *15* (17), 10869-10877.

19. Hao, J.; Wang, J.; Liu, X.; Padilla, W. J.; Zhou, L.; Qiu, M., High performance optical absorber based on a plasmonic metamaterial. *Applied Physics Letters* **2010,** *96* (25), 251104-251104-3.

20. Fraire, J. C.; Pérez, L. A.; Coronado, E. A., Cluster Size Effects in the Surface-Enhanced Raman Scattering Response of Ag and Au Nanoparticle Aggregates: Experimental and Theoretical Insight. *The Journal of Physical Chemistry C* **2013,** *117* (44), 23090-23107.

21. Ferry, V. E.; Sweatlock, L. A.; Pacifici, D.; Atwater, H. A., Plasmonic Nanostructure Design for Efficient Light Coupling into Solar Cells. *Nano Letters* **2008,** *8* (12), 4391-4397.

22. Tao, A.; Sinsermsuksakul, P.; Yang, P., Polyhedral Silver Nanocrystals with Distinct Scattering Signatures. *Angewandte Chemie International Edition* **2006,** *45* (28), 4597-4601.

23. Bresin, M.; Nehru, N.; Hastings, J. T. In *Focused electron-beam induced deposition of plasmonic nanostructures from aqueous solutions*, 2013; pp 861306-861306-6.

24. Dahmen, C.; Schmidt, B.; von Plessen, G., Radiation Damping in Metal Nanoparticle Pairs. *Nano Letters* **2007,** *7* (2), 318-322.

25. Zou, S.; Janel, N.; Schatz, G. C., Silver nanoparticle array structures that produce remarkably narrow plasmon lineshapes. *The Journal of Chemical Physics* **2004,** *120* (23), 10871-10875.

26. Nicoletti, O.; de la Pena, F.; Leary, R. K.; Holland, D. J.; Ducati, C.; Midgley, P. A., Three-dimensional imaging of localized surface plasmon resonances of metal nanoparticles. *Nature* **2013,** *502* (7469), 80-84.

27. Kanté, B.; de Lustrac, A.; Lourtioz, J. M., In-plane coupling and field enhancement in infrared metamaterial surfaces. *Physical Review B* **2009,** *80* (3), 035108.

28. Koh, A. L.; Fernández-Domínguez, A. I.; McComb, D. W.; Maier, S. A.; Yang, J. K. W., High-Resolution Mapping of Electron-Beam-Excited Plasmon Modes in Lithographically Defined Gold Nanostructures. *Nano Letters* **2011,** *11* (3), 1323-1330.

29. Kuester, E. F.; Mohamed, M. A.; Piket-May, M.; Holloway, C. L., Averaged transition conditions for electromagnetic fields at a metafilm. *Antennas and Propagation, IEEE Transactions on* **2003,** *51* (10), 2641-2651.

30. Le, F.; Lwin, N. Z.; Steele, J. M.; Käll, M.; Halas, N. J.; Nordlander, P., Plasmons in the Metallic Nanoparticle−Film System as a Tunable Impurity Problem. *Nano Letters* **2005,** *5* (10), 2009-2013.

31. Sun, Y.; Xia, Y., Shape-Controlled Synthesis of Gold and Silver Nanoparticles. *Science* **2002,** *298* (5601), 2176-2179.

32. Near, R.; Hayden, S.; El-Sayed, M., Extinction vs Absorption: Which Is the Indicator of Plasmonic Field Strength for Silver Nanocubes? *The Journal of Physical Chemistry C* **2012,** *116* (43), 23019-23026.

33. Rozin, M. J.; Rosen, D. A.; Dill, T. J.; Tao, A. R., Colloidal metasurfaces displaying near-ideal and tunable light absorbance in the infrared. *Nat Commun* **2015,** *6*.

34. Tao, A.; Sinsermsuksakul, P.; Yang, P., Tunable plasmonic lattices of silver nanocrystals. *Nat Nano* **2007,** *2* (7), 435-440.

35. Moreau, A.; Ciraci, C.; Mock, J. J.; Hill, R. T.; Wang, Q.; Wiley, B. J.; Chilkoti, A.; Smith, D. R., Controlled-reflectance surfaces with film-coupled colloidal nanoantennas. *Nature* **2012,** *492* (7427), 86-89.

36. Kulkarni, T. B. a. G. U., Femtoliter silver cups as surface enhanced Raman scattering active containers. *Nanotechnology* **2009,** *20* (4), 045504.

37. Balazs, A. C.; Emrick, T.; Russell, T. P., Nanoparticle Polymer Composites: Where Two Small Worlds Meet. *Science* **2006,** *314* (5802), 1107-1110.

38. McFarland, A. D.; Young, M. A.; Dieringer, J. A.; Van Duyne, R. P., Wavelength-scanned surface-enhanced Raman excitation spectroscopy. *Journal of Physical Chemistry B* **2005,** *109* (22), 11279-11285.

39. Holloway, C. L.; Love, D. C.; Kuester, E. F.; Salandrino, A.; Engheta, N., Sub-wavelength resonators: on the use of metafilms to overcome the λ size limit. *Microwaves, Antennas & Propagation, IET* **2008,** *2* (2), 120-129.

40. Shalaev, V. M., Optical negative-index metamaterials. *Nat Photon* **2007,** *1* (1), 41-48.

41. Søndergaard, T.; Bozhevolnyi, S., Slow-plasmon resonant nanostructures: Scattering and field enhancements. *Physical Review B* **2007,** *75* (7), 073402.

42. Ryu, J.-H.; Park, S.; Kim, B.; Klaikherd, A.; Russell, T. P.; Thayumanavan, S., Highly Ordered Gold Nanotubes Using Thiols at a Cleavable Block Copolymer Interface. *Journal of the American Chemical Society* **2009,** *131* (29).

43. Frankamp, B. L.; Uzun, O.; Ilhan, F.; Boal, A. K.; Rotello, V. M., Recognition-mediated assembly of nanoparticles into micellar structures with diblock copolymers. *Journal of the American Chemical Society* **2002,** *124* (6).